THE UNIVERSITY *of* EDINBURGH

SERS Nanosensors for Intracellular Redox Potential Measurements

Craig A. R. Auchinvole

Thesis presented for the degree of

Doctor of Philosophy,

The University of Edinburgh

September 2011

Supervisor: Dr Colin J. Campbell

Declaration of Authorship

I declare that this thesis is my own composition; that the work which is described has been carried out by me, unless otherwise stated; and that it has not been submitted in any previous application for a higher degree.

This thesis describes the results of research carried out in the School of Chemistry, University of Edinburgh, under the supervision of Dr Colin J. Campbell.

Craig A.R. Auchinvole
University of Edinburgh
September 2011

Signed:_____

Date:_____

Acknowledgements

Firstly I want to thank my supervisor, Dr. Colin Campbell, who gave me the opportunity to work with him on such an exciting research project. I am extremely grateful to Colin for all of his invaluable advice and support throughout my PhD. From the Campbell group, I extend my thanks to Mike and Ale, who I always enjoyed working with.

I would like to specially thank the late Professor Hamish McNab whose fantastic input in the synthetic work helped make the project successful. Hamish was a great man and a wonderful mentor to me and all of his students. I thank all my friends in the McNab group (Ran, Mary, Emma, Patrick and Will) for making me feel so welcome and for helping me to find my feet in the early days.

I acknowledge Professor Ken Donaldson and his group (particularly Irene and Jen) for sharing their expertise and advice on cellular toxicity studies. Professor Eleanor Campbell and her group (especially Oleg, Andre and Johan) must also be acknowledged for allowing me to use their equipment and assisting me with technical troubles.

Further appreciation goes to our collaborators in Biology and DPM, particularly Dr Amy Buck and Diwa, and to Professor Mark Bradley and his group for use of their facilities. I am also grateful to Patricia for her help with DFT calculations. In addition, I thank all the brilliant support staff in the School of Chemistry who helped make my life easier over the last three years.

Finally I would like to thank all of my family and friends for their understanding and support and, in particular, my father-in-law, Ian, for his helpful advice. I reserve extra-special thanks for my beautiful and amazing wife, Kate, who has been incredible over the last three years! She is the best person I have ever met and who I am very lucky to have. I dedicate this work to her.

Abstract

Redox regulation and homeostasis are critically important in the regulation of cell function; however, there are significant challenges in quantitatively measuring and monitoring intracellular redox potentials.

The work in this thesis details a novel approach to intracellular redox monitoring. The approach is based on the use of nanosensors, which comprise molecules capable of sensing the local redox potential, assembled on gold nanoshells. Since the Raman spectra of the sensor molecules change depending on their oxidation state, and since the nanoshells allow a large enhancement of the Raman scattering, intracellular potential can be calculated by simple optical measurements. A full description of the design, fabrication and characterisation (spectroscopic and electrochemical) of the nanosensors is provided within.

The ability to deliver nanosensors into cells in a controllable fashion was confirmed using electron microscopy. Results from a range of assays are also presented which reveal that introduction of nanosensors does not result in any cytotoxicity.

Sensor utility in monitoring redox potentials as cells responded to physiological and superphysiological oxidative and reductive stimuli was investigated. Importantly, the capability of the nanosensors in monitoring intracellular potentials in a reversible, non-invasive manner, and over a previously unattainable potential range, is demonstrated.

Contents

List of Figures

List of Equations

List of Schemes

List of Tables

Abbreviations

3'UTR	Three prime untranslated region
AA	Amino acid
AAPH	2,2′ azobis-2-amidinopropane
AFM	Atomic force microscopy
AGO	Argonaute
AIF	Apoptosis-inducing factor
APAF-1	Apoptotic protease activating factor-1
AQ	Bis-(2-Anthraquinone carboxamide)
ATP	Adenosine triphosphate
b	Broad
BCA	Bicinchoninic acid assay
BMES	Bis(2-mercaptoethyl)sulfone
BSA	Bovine serum albumin
CA-NLS 1	Fluorescein-aminohexanoic acid-PKKKRKVC
CA-NLS 2	CGGPKKKRKVGG
CARS	Coherent anti-Stokes Raman spectroscopy
CAT	Catalase
CS	Calf serum
CT	Charge transfer
CTAB	Cetyltrimethylammonium bromide
CV	Cyclic voltammogram
Cys	Cysteine
CyS/CySSyC	Cysteine/cysteine disulfide
DFC	2’,7’-dichlorfluorescein
DCFH	Non-fluorescent 2’,7’-dichlorfluorescein
DCM	Dichloromethane
DFM	Dimethylformamide
DFT	Density functional theory
DHAR	Dehydroascorbate reductase

DIC	Diisopropylcarbodiimide
DIPEA	*N*,*N*-Diisopropylethylamine
DMEM	Dulbecco's Modified Eagle's Medium
DMSO	Dimethyl sulfoxide
DNA	Deoxyribonucleic acid
DTNB	5,5'-dithiobis-(2-nitrobenzoic acid)
DTT	Dithiothreitol
E	Potential
ECP	Effective core potential
EDC	1-Ethyl-3-(3-dimethylaminopropyl)carbodiimide
EDTA	Ethylenediaminetetraacetic acid
ELSD	Evaporative light-scattering detector
eq.	Equivalents
ER	Endoplasmic reticulum
ETC	Electron transport chain
EtOH	Ethanol
EXP-5	Exportin-5
FCBX	N-(2-mercaptoethyl) ferrocene carboxamide
fmoc	9-fluorenylmethyloxycarbonyl
G-6-P	Glucose 6-phosphate
G6PD	Glucose 6-phosphate dehydrogenase
GCL	Glutamate cysteine ligases
GFP	Green fluorescent protein
Glu	Glutamic acid
GPx	Glutathione peroxidase
GR	Glutathione reductase
GS	Guanosine synthetase
GSH	Glutathione
GSNO	S-nitrosoglutathione
GSSG	Glutathione disulfide
GST	Glutathione S-transferase
GSTNB	Glutathione-S-5-thio-2-nitrobenzoic acid

HBTU	2-(1H-Benzotriazole-1-yl)-1,1,3,3-tetramethyluronium hexafluorophosphate
HOBt	Hydroxybenzotriazole
HPLC	High performance liquid chromatography
HQ	2-Mercaptohydroquinone
IMP	Importin
IPA	Isopropyl alcohol
IR	Infrared
IRP	Intracellular redox potential
KPE	0.1M phosphate buffer with 5 mM EDTA
m	Multiplet
M2VP	1-methyl-2-vinyl-pyridinium trifluoromethane sulfonate
M4VP	1-methyl-4-vinyl-pyridinium trifluoromethane sulfonate
MALDI-TOF	Matrix-assisted laser desorption/ionization–time-of-flight
MeCN	Acetonitrile
MeOH	Methanol
mRNA	Messenger RNA
miRNA	MicroRNA
mp	Melting point
MTT	3-(4,5-dimethylthiazol-2-yl)-2,5-diphenyltetrazolium bromide
NA	Numerical Aperture
$NADP^+$	Nicotinamide adenine dinucleotide phosphate
NADPH	Reduced nicotinamide adenine dinucleotide phosphate
NEM	*N*-ethylmaleimide
NHE	Normal hydrogen electrode
NLS	Nuclear localisation sequence
NMP	*N*-methylpyrrolidone
NMR	Nuclear magnetic resonance
NPC	Nuclear pore complex
NOS	NO synthase
NQ	1,8-diaza-4,5-dithia-1,8-di(2-chloro-[1,4]-naphthoquinone-3-yl)octane
Nqo1	NADPH quinone oxidoreductase 1

NR	Gold nanorods
NS	Gold nanoshells
P450	Cytochrome P450
PBS	Phosphate buffered saline
PCA	Principal component analysis
pMBA	Para-mercaptobenzoic acid
pre-miRNA	Precursor miRNA
pri-miRNA	Primary miRNA
q	Quartet
RAM	Redox-active molecules
RFU	Relative fluorescence units
RISC	RNA-induced silencing complex
RNA	Ribonucleic acid
roGFP	Redox-active GFP
ROS	Reactive oxygen species
RP	Redox potential
RP-HPLC	Reverse-phase HPLC
rt	Room temperature
s	Singlet
SAM	Self assembled monolayer
SERS	Surface enhanced Raman spectroscopy
SOD	Superoxide dismutase
SPPS	Solid-phase peptide synthesis
SPR	Surface plasmon resonance
t	Triplet
TCEP	Tris(2-carboxyethyl)phosphine
TEM	Transmission electron microscopy
TFA	Trifluoroacetic Acid
TIS	Triisopropylsilane
TLC	Thin Layer Chromatography
TNB	5-thio-2-nitrobenzoic acid
TNF	Tumour necrosis factor

$Trx\text{-}S_2$	Oxidised thioredoxin
UPR	Unfolded protein response
UV	Ultraviolet
Vit C	Vitamin C
δ_H	Chemical shift of hydrogen
δ_C	Chemical shift of carbon

Chapter 1

Introduction

1.1 Overview

In cells, redox potential (RP) is a highly regulated and compartmentalised property. Its homeostasis and regulation are critical in numerous cellular processes and events including: cell cycle, differentiation, apoptosis, inflammation, toxicity, protein interactions and signalling.[1,2,3,4,5] Despite its importance, the study of intracellular redox potential (IRP) has thus far been limited by the lack of suitable techniques with which to monitor it.

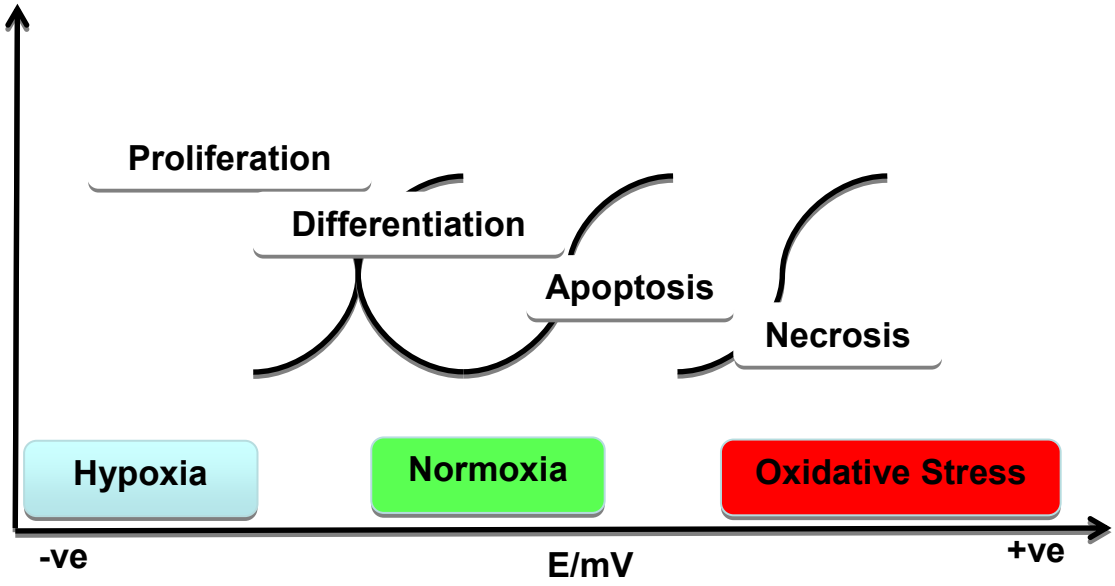

Figure 1.1: Variation of IRP through different biological stages of the cell cycle. In healthy cells, potential (E) is most negative during proliferation.[6] As E increases, cells may undergo differentiation, or apoptosis (programmed cell death).[6] Extremely high values of E from oxidative stress will eventually result in necrosis.[6]

An ideal system for IRP measurements should be able to:

(1) Quantitatively and reversibly monitor potential in live cells, with good spatiotemporal resolution.

Many traditional methods of calculating IRP involve cell lysis and cumbersome analytical separations.[7] Sensors would preferably be able to monitor, in real-time, potential from discrete cellular locations.

(2) Monitor RP with sub-cellular resolution.

It has been shown that the RPs of organelles are not in equilibrium with each other. For instance, the endoplasmic reticulum (ER) is held at a more oxidative poise than the cytoplasm in order to facilitate protein folding.[8] On the other hand, the nucleus may be held at a more reductive poise[6] in order to protect important biomolecules such as deoxyribonucleic acid (DNA) from oxidative damage.[9] The ability to target, efficiently and effectively, a sensor to monitor the potential in specific organelles would offer better understanding of cellular redox processes and how IRP is modulated throughout the life cycle of a cell.

(3) Monitor RP over a wide range covering hypoxic conditions, through the processes involved in oxidative stress.

The hypothetical electrochemical window of a cell spans more than a volt (as determined by reduced nicotinamide adenine dinucleotide phosphate (NADPH) (most reducing redox couple) and oxygen (most oxidative redox couple).[6] The current state of the art redox sensors possess relatively low mid-point potentials and, therefore, cannot accurately report on potentials in more oxidising environments, or during oxidative processes.[10,11,12] Widening the current range of intracellular potential measurements would thus prove highly advantageous when monitoring the potential inside oxidative compartments such as the ER or lysosomes,[8,13] or when following potential changes through processes such as apoptosis or necrosis.

(4) Be non-perturbing to the native redox poise of the cell.

The delivery of any system designed to probe the redox environment of a cell should not result in any reductive or oxidative toxic side effects.

1.2 Regulation of Intracellular Redox Potential

RP can be defined as:

> 'The reducing or oxidising power of a system, measured against the potential at a hydrogen electrode.'
>
> *-Biology Online*

Developed in 1889 by Walter Nernst, his famous equation allows comparison of potentials measured under standard conditions (E^{o}) with potentials measured under non-standard conditions:[14]

$$E = E^{\theta} + \frac{RT}{nF} \ln \frac{[O]}{[R]}$$

Equation 1.1: The Nernst equation (assuming equilibrium). Where E = potential (V), E^{o} = standard potential (V); R = universal gas constant; T = temperature (K); F = Faraday's constant; n = number of electrons involved in transfer reaction; [*O*] = concentration of oxidised species; and [*R*] = concentration of reduced species.

The Nernst equation has particular importance in biology, where electron transfer reactions are common-place.[6] Indeed, many of the current methods used to measure or monitor IRP rely on the Nernst equation.

IRP can be thought of as a delicately balanced cellular property. It relies on a variety of factors including, on the one hand, reactive oxygen species (ROS), and on the other hand, the cell's antioxidant system (including glutathione (GSH), thioredoxin, NADPH and enzymes) which detoxifies them.

1.2.1 ROS and Oxidative Stress

ROS are highly reactive oxygen-containing molecules. Examples of prominent cellular ROS include: hydrogen peroxide (H_2O_2), superoxide ($O_2^{\cdot -}$), hydroxyl radicals ($^{\cdot}OH$), nitric oxide (NO) and peroxynitrite ($OONO^-$).[2,15]

With a concentration of 10^{-7} M and a half-life ($t_{1/2}$) of 10^{-5} s, H_2O_2 is by far the most abundant and most stable intracellular ROS.[2] H_2O_2 is generated mainly as a result of electron leakage from the mitochondrial electron transport chain (ETC).[2,16] In the ETC, electrons are transported across four protein complexes to molecular oxygen, generating water and establishing a proton gradient across the inner mitochondrial membrane.[16,17] Energy from this gradient is then used to drive production of adenosine triphosphate (ATP), which is a cell's primary source of energy.[17] However, this process is not 100% efficient and electrons can leak from the ETC. These electrons can then react with molecular oxygen to generate $O_2^{\cdot -}$.[2,16] This is the main source of intracellular oxidant. Aided by superoxide dismutase (SOD) enzymes, $O_2^{\cdot -}$ can be dismutated to H_2O_2 and O_2.[2,16] H_2O_2 can be decomposed by catalase (CAT) to form water and molecular oxygen,[18] or through the Fenton reaction to form $^{\cdot}OH$.[19] Due to their high reactivity with biomolecules, $^{\cdot}OH$ are considered to be among the most hazardous ROS.[20] Despite the cytotoxic effects it can cause, it is worth noting that H_2O_2 has also been shown to be an important cell-signalling molecule in a variety of processes.[1,2]

Figure 1.2 below shows how common ROS are generated inside cells.

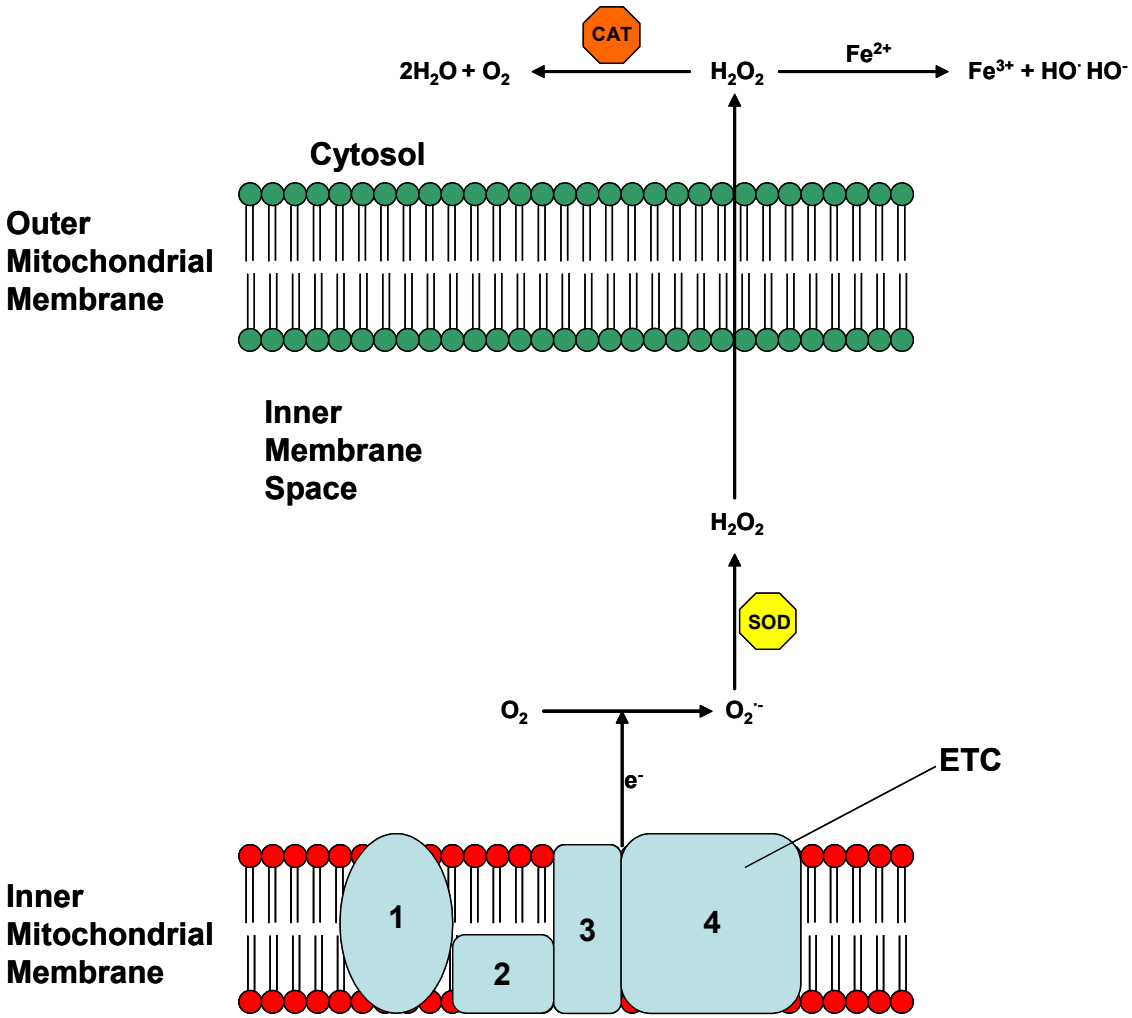

Figure 1.2: Mitochondrial ROS generation. Electron leakage from the ETC can lead to $O_2^{\cdot -}$ formation. SOD enzymes convert the $O_2^{\cdot -}$ into H_2O_2 which can translocate from the mitochondria to the cytoplasm and be converted into water and oxygen by catalase or participate in intracellular Fenton reactions.

Synthesised enzymatically by NO synthase (NOS) from L-arginine,[21] NO is also an important cellular ROS. Inside cells, NO can react with $O_2^{\cdot -}$ forming highly cytotoxic peroxynitrite.[15] NO can also react with GSH to form S-nitrosoglutathione (GSNO), which can act as a NO reservoir/donor.[22] Like H_2O_2, NO is also an important cell-signalling molecule, particularly affecting the vascular system.[23] Figure 1.3 below shows how NO is synthesised in cells and the fates which may befall it.

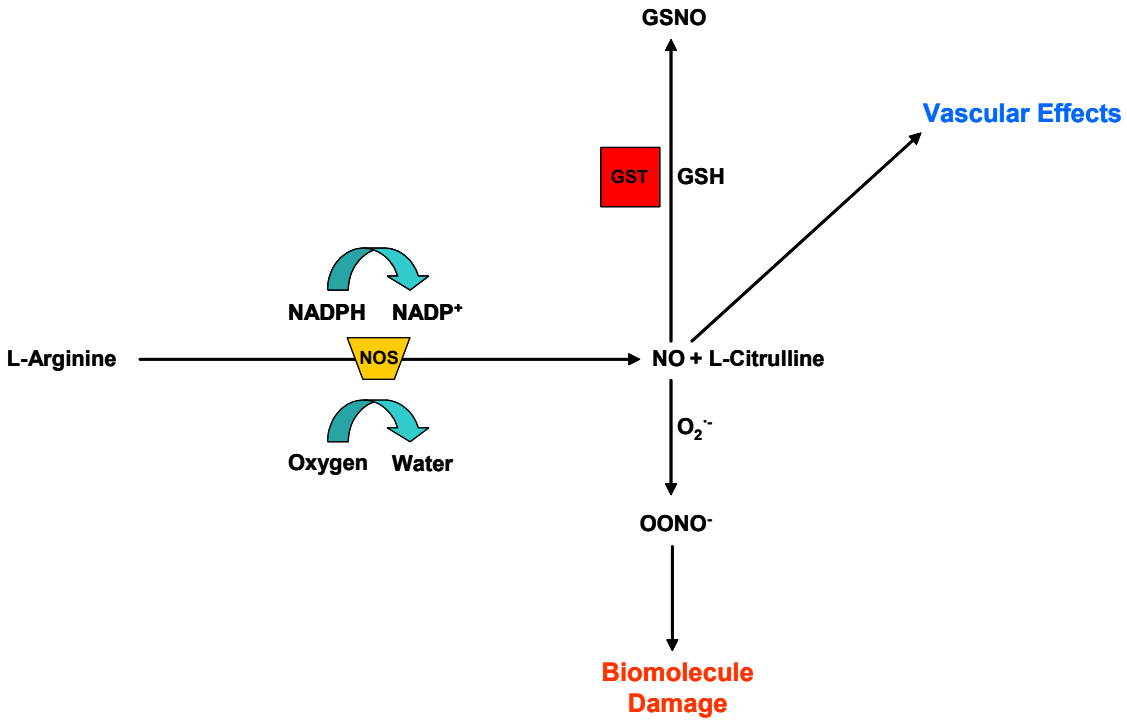

Figure 1.3: NO synthesis form L-arginine by NOS and possible intracellular fates of NO including: reaction with GSH, formation of peroxynitrite (leading to biomolecule damage) and effects on the vascular system (particularly in vasodilatation).

Although ROS are produced endogenously by cells and are important biological messengers and cell-signalling molecules, their unrestricted generation can lead to oxidative stress. In turn, oxidative stress can lead to severe and irreparable damage to cells.[6,24,25]

Oxidative stress can be defined as an increase in oxidant generation that cannot be sufficiently dealt with by a cell's antioxidant defence mechanisms.

Figure 1.4 below shows the main processes involved in oxidative stress.

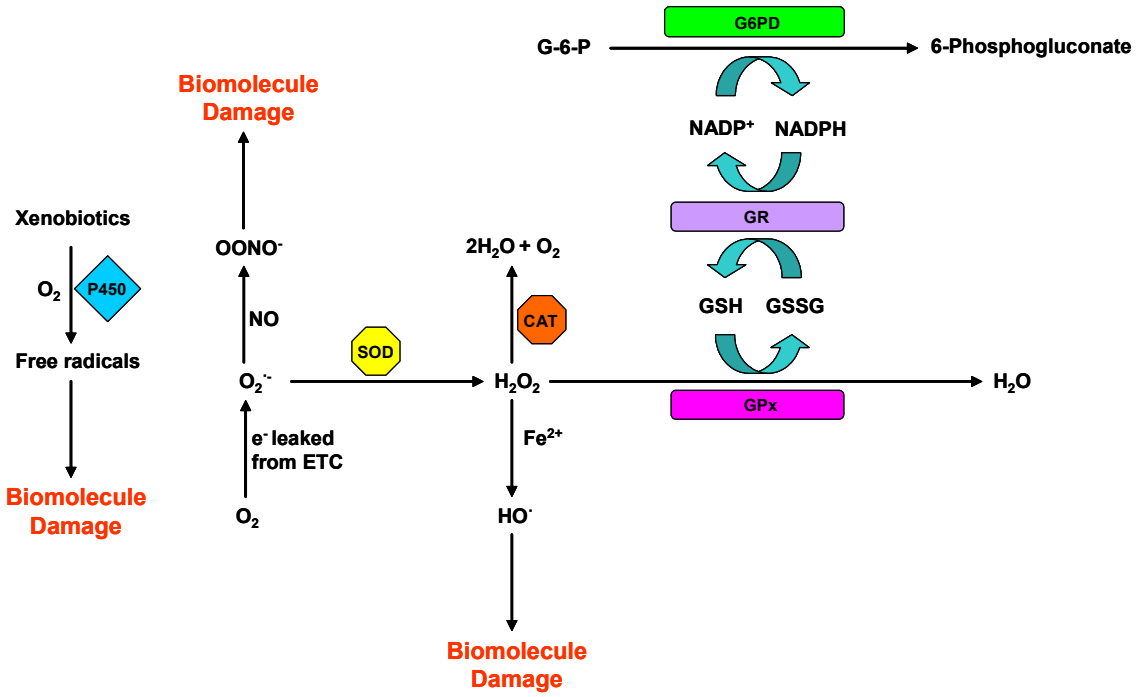

Figure 1.4: Mechanism showing how oxidative stress can be imposed on cells. Cell damage is induced by ROS. The main source of ROS *in vivo* is aerobic respiration, although ROS are also produced by other means including cytochrome P450 metabolism of xenobiotic compounds. Under normal conditions, ROS are cleared from the cell by the action of SOD, catalase, or glutathione peroxidase. The main damage to cells results from the ROS-induced alteration of macromolecules such as polyunsaturated fatty acids in membrane lipids, essential proteins, and DNA.

As mentioned on page 4, $O_2^{\cdot-}$ radicals in cells are generated mainly from the reaction of oxygen with electrons leaked from the mitochondrial ETC.[2,16] $O_2^{\cdot-}$ can react with NO to form the highly cytotoxic $OONO^-$ species[15] or are dismutated by SOD to form H_2O_2.[2,16] H_2O_2 can then participate in intracellular Fenton reactions with Fe^{2+}, generating $^{\cdot}OH$ radicals.[19,25] It may also be degraded by CAT (to water and oxygen) or through the glutathione peroxidase (GPx) system (to water).[22] There are other intracellular sources of ROS, including those that come from the breakdown of xenobiotics by cytochrome P450 (P450) enzymes.[26]

Under normal physiological conditions, these ROS are eliminated from the cell by its antioxidant defence systems. Oxidative stress ensues if ROS generation exceeds the capabilities of the cell's antioxidant defence system,[6,24] or if there is malfunction within the antioxidant defence system. The ROS generated during oxidative stress can go on to cause major damage to critical biomolecules, such as nucleic acids, lipids or proteins.[6,24,25] At a molecular level, common damages caused to these biomolecules by ROS include: hydroxylation of DNA bases, peroxidation of lipids, tyrosine nitration and cysteine oxidation (figure 1.5).[27,28,29] Indeed, the onset of oxidative stress has been implicated in several disease states including: cancers, cardiovascular diseases and neurodegenerative diseases.[30,31,32]

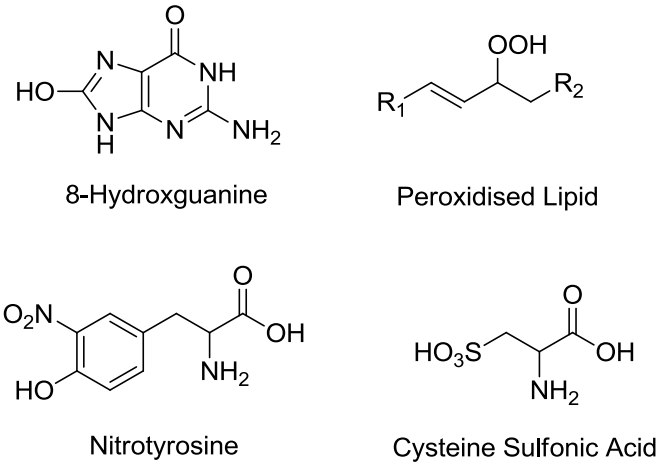

Figure 1.5: Common biomolecule damage caused by ROS. Top left – 8-hydroxyguanine. Top right – an unsaturated, peroxidised lipid. Bottom left – nitrated tyrosine. Bottom right – oxidised cysteine.

1.2.2 Antioxidant Defences

In order to defend themselves and detoxify ROS, cells harbour several important antioxidant defence mechanisms. These systems are crucial in the protection of biomolecules, without which proper cell function would cease.

1.2.2.1 Glutathione

Glutathione (GSH) is a tripeptide, synthesised naturally in the body from the amino acids (AAs) L-cysteine, L-glutamic acid, and glycine.[22] With concentrations ranging from 1-10 mM in the cytoplasm, GSH is considered to be the major thiol-disulfide redox buffer/antioxidant defence of the cell.[6] In cells, GSH can become oxidised to form glutathione disulfide (GSSG). The structures of GSH and GSSG are shown below in figure 1.6. In cells, under normoxic conditions, more than 90% of total glutathione exists as GSH.[6] Any increase in the [GSSG]:[GSH] ratio is generally interpreted as cytotoxic.

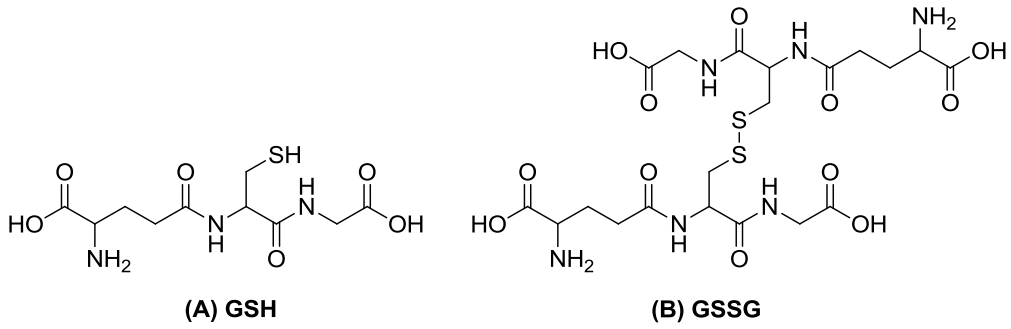

Figure 1.6: Molecular structures of **(A)** GSH and **(B)** GSSG.

Figure 1.7 below shows the processes involving GSH in cellular redox defence.

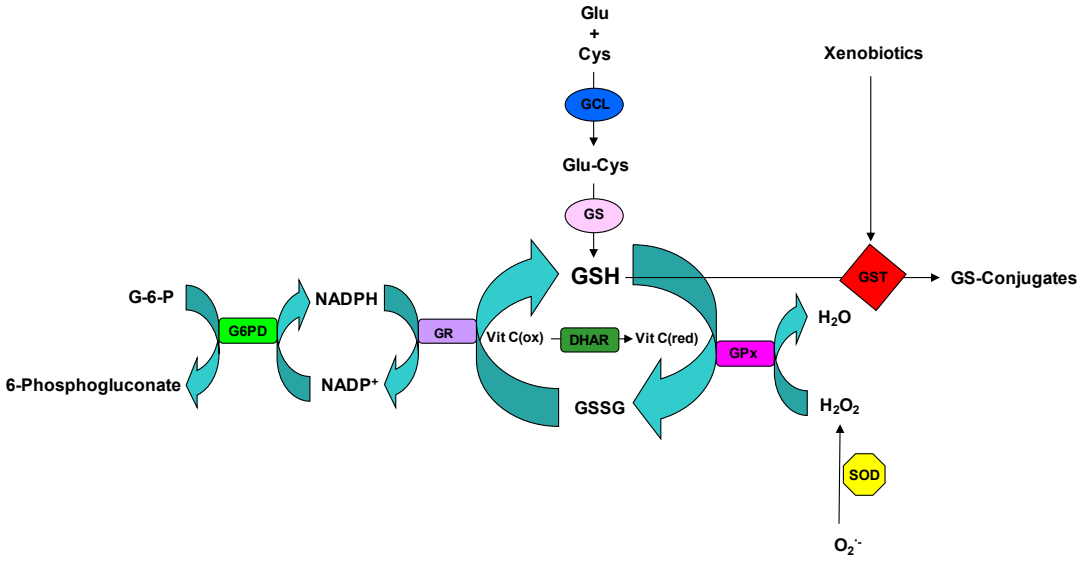

Figure 1.7: Defence actions of GSH. Synthesised from glutamic acid, cysteine and glycine GSH can detoxify ROS (such as H_2O_2) through the GPx system. It can also detoxify harmful xenobiotic substances through the GST system and helps to maintain a steady concentration of ascorbic acid through the GR system.

As an antitoxic agent, GSH is able to act as both a nucleophile and as a reductant. It can react with harmful electrophilic or oxidising xenobiotic species and prevent them from reacting with and causing damage to important biomolecules.[22,25] Detoxifications involving GSH are catalysed by glutathione S-transferases (GSTs),[22] an important and abundant class of cellular enzymes.[33]

Arguably, GSH's most important defence function is that of an antioxidant. Just as GSH is able to detoxify harmful xenobiotics, it can also neutralise ROS like H_2O_2 through the GPx system.[22] Again, this helps to prevent crucial biomolecules suffering oxidative damage. GSH also participates in the glutathione-ascorbate metabolic pathway, whereby GSH-dependent dehydroascorbate reductases (DHARs) help sustain a steady concentration of ascorbic acid (vitamin C) in the face of oxidative stress.[22] GSH is regenerated from these processes through glutathione reductase (GR) which catalyses the reaction of GSSG with NADPH to yield GSH along with nicotinamide adenine dinucleotide phosphate ($NADP^+$).[22,25]

1.2.2.2 Thioredoxin

The thioredoxin system is another crucial thiol-disulfide antioxidant system present in micromolar concentration in cells. Thioredoxins are large oxidoreductase proteins which contain a dithiol-disulfide active site (figure 1.8).[6,24]

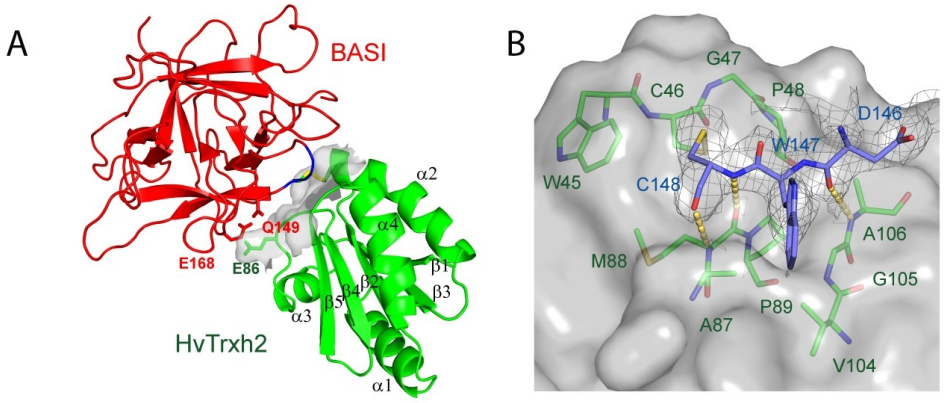

Figure 1.8: Crystal structure of thioredoxin showing **(A)** an overview of the secondary structure of barley thioredoxin h (HvTrxh2) in a disulfide linked complex with barley a-amylase subtilisin and **(B)** the active-site.[34]

Thioredoxins exert their antioxidant effect by facilitating protein reduction through cysteine thiol-disulfide exchange.[24] Unlike GSH which forms inter-molecular disulfides, thioredoxins usually form intra-molecular disulfides which can be reduced back to thiols by the enzyme thioredoxin reductase, in a process dependent on NADPH (figure 1.9).[24]

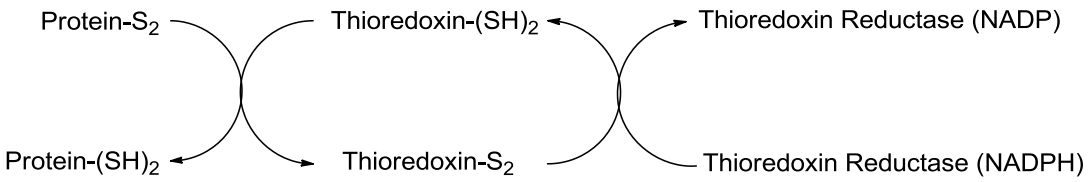

Figure 1.9: Antioxidant mechanism of thioredoxin. Thioredoxin reduces disulfide bonds in target proteins. Oxidized thioredoxin is reduced by thioredoxin reductase, which receives reducing equivalents from NADPH.

In terms of biological function, by acting as a cytokine modulator, thioredoxins are an important part of the inflammatory response.[35,36] They also facilitate refolding of proteins and regulate DNA binding activity of some transcription factors.[37]

1.2.2.3 Nicotinamide Adenine Dinucleotide Phosphate

NADPH is mainly generated during the oxidative phase of the pentose phosphate pathway.[17] NADPH can provide reducing equivalents for the redox processes involved in the detoxification of ROS.[22,24,25] It is responsible for reconversion of GSSG and oxidised thioredoxin (Trx-S_2) to their reduced states. The NADPH system also generates free radicals for immune cells to destroy pathogens in the respiratory burst.[38] Figure 1.10 below shows the structure of $NADP^+$, along with its reduction to NADPH at its nicotinamide moiety.

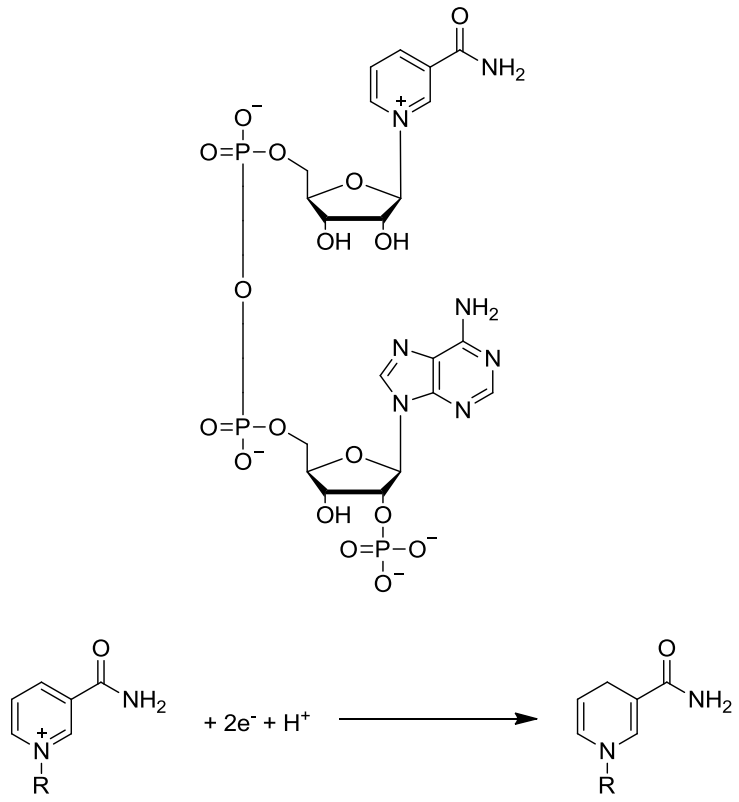

Figure 1.10: Structure of $NADP^+$ along with its reduction reaction during which it gains two protons and an electron.

1.2.2.4 Antioxidant Enzymes

Enzymes are globular proteins that catalyse biological processes.[17] In cells, enzymes are an important part of the antioxidant defence system and work in conjunction with small molecules like GSH and NADPH, as well as thioredoxin, to protect cells against the harmful effects of ROS. [2,16,24,39]

SODs were among the first antioxidant enzymes to be discovered.[40] Highly efficient in their function, SODs operate by converting $O_2^{\cdot -}$ into H_2O_2 and molecular oxygen (figure 1.10).[2]

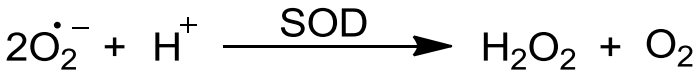

Figure 1.11: Dismutation of $O_2^{\cdot -}$ by SOD to form H_2O_2 and oxygen.

Through intracellular Fenton reactions, $^{\cdot}OH$ can be formed from H_2O_2.[19,41] CAT lowers the risk of this occurring, by catalysing the dismutation of H_2O_2 into water and oxygen (figure 1.12).[18]

Figure 1.12: Dismutation of H_2O_2 by CAT to form water and oxygen.

Both the GSH and thioredoxin systems have several important associated enzymes that ensure their optimum function. GPxs catalyse reactions which detoxify ROS (figures 1.4 and 1.6).[22,25] GSH and thioredoxin reductases ensure that GSSG and Trx-S_2 are reduced back to their antioxidant forms, GSH (figure 1.4 and 1.7) and thioredoxin (figure 1.9).[22,24,25,39]

1.2.2.5 ROS Regulation of Gene Expression and Cellular Control of Free Transition Metals

While the harmful effects of excessive ROS generation/accumulation in cells have been discussed it is also important to take into account that they play important roles as cellular messengers.[2] One of the most important functions of ROS is the regulation of gene expression.[2,42,43] Many cellular proteins possess cysteine residues, which can be subjected to oxidation/reduction reactions at their thiol moieties.[2,42] Indeed, H_2O_2 has been shown to regulate the activity of a host of kinases and phosphatases through oxidation.[2,42] Some of these proteins are in fact transcription factors (proteins that control the flow of genetic information from DNA to RNA). The transcription factor AP-1 is one of the most studied cases of transcriptional redox regulation. Through induction by H_2O_2 AP-1 can control the regulation of a number of genes involved in the cellular processes of differentiation, proliferation and apoptosis.[42] Other important transcription factors regulated by ROS include MTF-1 (which is involved in metal homeostasis) and NF-KB (which is involved in cellular defence and immunological response).[42]

Traces of transition metals such as iron, copper, manganese and zinc are commonly found within our cells and are essential in their healthy function.[17] As outlined in section 1.2.1, free transition metals in cells can participate in harmful intracellular Fenton reactions which can lead to ROS generation and subsequent biomolecule damage. It would, however, be inaccurate to suggest that the presence of free transition metals in cells is widespread and unchecked. While increased cellular levels of transition metals have been associated with neurological diseases,[31] in healthy cells transition metals are tightly regulated.[44,45,46] For example, iron, an important component of haemoglobin and a variety of redox enzymes, has its uptake regulated by a number of proteins including transferrin and iron regulatory proteins.[44] Similarly, zinc, important as a co-factor and intracellular mediator, is regulated by proteins which control its uptake and intracellular trafficking. These proteins include membrane transporters belonging to the ZIP, ZnT and metallothioein families.[45]

1.3 Current Techniques for Measuring and Monitoring Intracellular Redox Potential

There are several techniques available for the study of IRP. While each has its merits, none of them currently meet the requirements for an ideal cellular redox monitoring system, as outlined on page 2.

One of the common drawbacks of current techniques used in IRP measurement is tailoring them to measure cellular GSH. While it has been widely acknowledged as the main thiol-disulfide redox buffer of the cell,[6] the other systems described on pages 11-14 also play important roles. In the dynamic environment of a cell, where redox couples are not necessarily in equilibrium with one another, there is no one fixed IRP value. IRP will vary depending on the particular redox couple being measured, the relative concentrations of redox couples and where exactly in the cell a measurement is being taken from.[6] For example, the NADPH/$NADP^+$ redox couple has an E°' of -315 mV whereas the E°' of GSH/GSSG is more oxidising at -240 mV (both vs. NHE at pH 7).[6] Moreover, while, for instance, the cytoplasm has been shown to possess relatively reducing redox potentials (approximately -270 mV) the ER has been shown to possess a considerably more oxidising redox potential (approximately -209 mV).[6,8] Therefore, one cannot simply give a definitive value of IRP based solely on the measurement of a single redox couple or from a single organelle.

1.3.1 GSH-Recycling Assay

In 1969, Tietze[47] developed an enzymatic assay for the quantification of cellular glutathione. The assay uses enzymatic recycling, with GR employed, in order to ensure reduction of all cellular glutathione to GSH. The thiol groups of GSH are then allowed to react with DTNB. This produces 5-thio-2-nitrobenzoic acid (TNB) (yellow in colour) and a complex glutathione-S-5-thio-2-nitrobenzoic acid (GSTNB). The GSTNB complex is reduced by GR to regenerate GSH and more TNB. The rate

of TNB formation is directly proportional to the GSH concentration in the sample, which can be estimated spectrophotometrically through absorbance measurements at 412 nm.

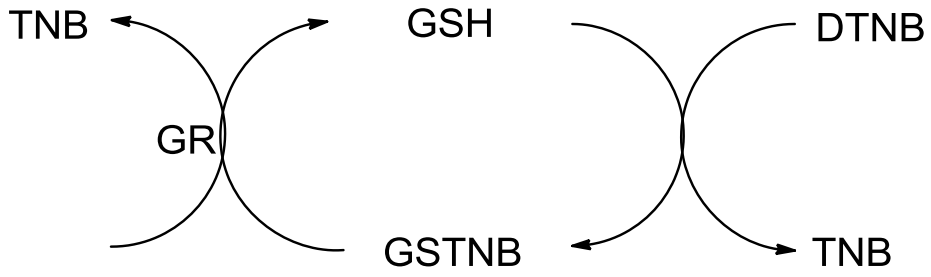

Figure 1.13: Schematic of the GSH-recycling assay. After converting all cellular to GSSG with GR, thiol groups of GSH can react with DTNB producing GSTNB and TNB. GSTNB is reduced by GR to regenerate GSH and produces more TNB. TNB formation rate is directly proportional to sample GSH concentration.

In order to determine GSSG levels, GSH must first be derivatised. This prevents GSH from taking part in the cycle shown in figure 1.13, to allow sole determination of GSSG. Initially, *N*-ethylmaleimide (NEM) was employed by Tietze[47] as a thiol masking agent for GSH. Lack of specificity and the need to eliminate excess NEM, which could potentially inhibit GR, made the technique somewhat error-prone and time-consuming.[48] However, the replacement of NEM with 1-methyl-2-vinyl-pyridinium trifluoromethane sulfonate (M2VP), or 1-methyl-4-vinyl-pyridinium trifluoromethane sulfonate (M4VP), as derivatisation agents, enabled Tietze's assay to be performed quicker and with greater accuracy.[48,49]

Once total GSH and GSSG concentrations have been determined, the [GSH]:[GSSG] ratio can be calculated. Usually, GSH and GSSG concentrations are expressed in molar concentrations and quoted against the total protein content of cells (usually reported in mg). These ratios can then be input to the Nernst equation, from which a value of cellular RP can be estimated. RP values of mammalian cells have been reported between -315 and -280 mV vs. NHE.[50] [GSH]:[GSSG] ratios outside the

homeostatic will result in potential values outside this range and serve as an indicator of cellular toxicity.

Tietze's assay is still widely in use today. While the assay is relatively simple to perform and gives the user a useful indication of toxicity, it suffers from some significant drawbacks. The assay cannot be used for live cellular RP monitoring, as it requires the harvesting of GSH from cells. In order to achieve this, cells have to be lysed.[47] Moreover neither inter- nor intra-cellular potential variation can be accounted for, as GSH is harvested indiscriminately from populations consisting of thousands of cells. The assay is also prone to inaccuracy resulting from the oxidation of GSH to GSSG in air.[48,49] Therefore, users must be extremely careful in sampling and sample handling.

1.3.2 High Performance Liquid Chromatography (HPLC)

Detection and quantification of GSH and GSSG by HPLC has also been extensively demonstrated. As may be expected, these two molecules can be easily separated on a column (mostly, reverse-phase HPLC (RP-HPLC) is used).[7] Indeed, characteristic retention times allow their resolution in complex biological samples which contain a variety of other species. Key advantages of using HPLC over the GSH recycling assay include higher sensitivity and simultaneous detection of GSH and GSSG. Derivatisation is also not always a requirement, making sample preparations easier.[51]

Unfortunately, using HPLC to measure the GSH:GSSG ratio suffers from all the drawbacks associated with the earlier GSH recycling assay. Cell lysis is still required and, therefore, the technique is unsuitable for monitoring. Neither organelle nor cell-to-cell variation can be accounted for and oxidation of GSH in air is still a concern to users.

1.3.3 Hydrocyanine Dyes

Developed in 2009 by Kundu *et al*,[52] hydrocyanines are a membrane-permeable family of ROS sensors. They can be easily synthesised from the reduction of commercially available cyanine dyes with the relatively mild reducing agent $NaBH_4$ (figure 1.14).[52]

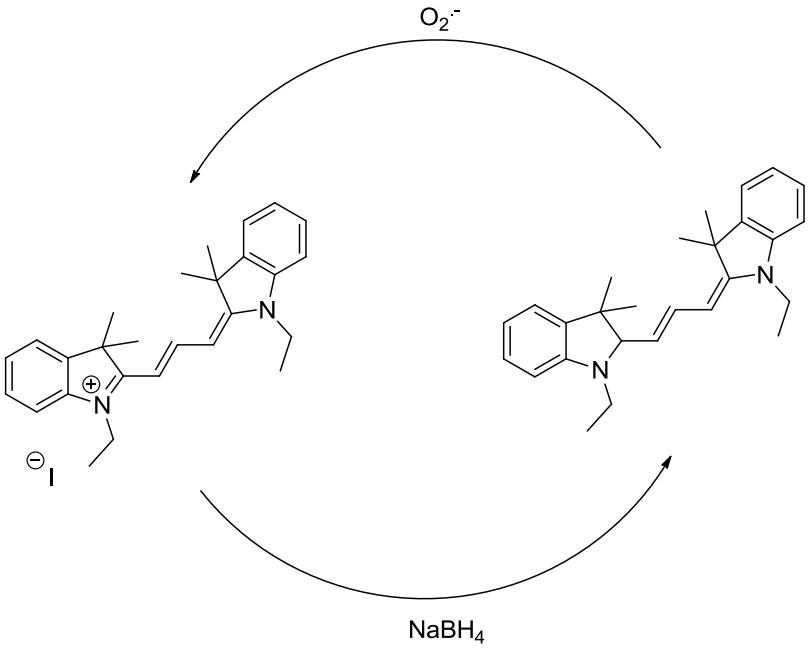

Figure 1.14: Synthesis of non-fluorescent hydro-Cy3 by a one-step reduction with $NaBH_4$. Reaction with ROS oxidises hydro-Cy3 to generate fluorescent Cy3.

These compounds offer significant advantages over other fluorescent ROS sensing dyes. They display excellent stability to autoxidation, tuneable emission wavelengths, and nanomolar sensitivity to ROS.[52] Despite this, hydrocyanines (and other fluorescent dyes) cannot be employed to report on the RP of the cell – only on the rate of formation of particular ROS. Since they operate via covalent reaction (i.e. they are non-reversible), they are unsuitable for monitoring. Furthermore, they do not take into account the mechanisms that the cell naturally puts into place for detoxification of ROS (e.g. in the presence of an efficient antioxidant system, a rise in ROS may not dramatically impact the redox state of the cell).

1.3.4 Glutathione Reductase Crystals

In 1999, Keese *et al* reported using crystals of GR to monitor the RP in the cytoplasm of human fibroblasts.[53] When oxidised, the crystals appear yellow, but upon exposure to solutions containing GSH or NADPH (reductants), they become orange-red (figure 1.15). In their reduced state, GR crystals have a free thiol at Cys-58 and a free thiolate at Cys-63. The free thiolate can form a charge transfer (CT) complex with flavin.[53] Formation of this CT complex is accompanied by the rise of a new absorption band (around 540 nm) and a colour change from yellow to orange-red.[53]

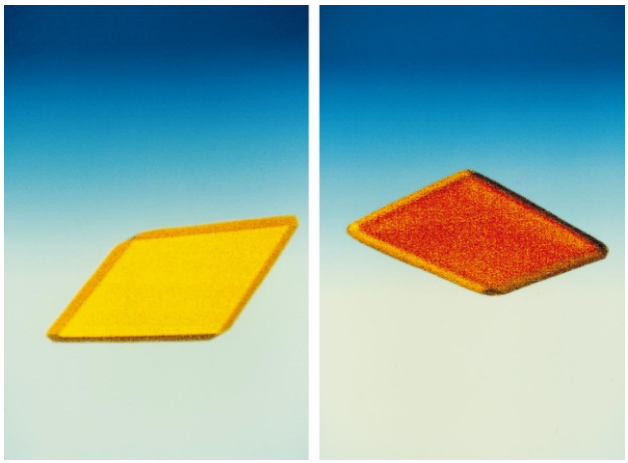

Figure 1.15: Colour changes of GR crystals. An oxidised (yellow) GR crystal is shown on the left and a reduced (orange-red) GR crystal is shown on the right.[53]

Keese *et al* micro-injected the crystals into the cytoplasm and reported on the RP through colour changes in the crystals (figure 1.15).[53] Unlike the GSH recycling assay or HPLC, these crystals offer the chance to monitor RP from inside live cells on a single cell basis. This technique is, however, cumbersome and suffers from slow kinetic responses, as well as being limited in the range of RP which it can monitor.

1.3.5 Redox-Active Green Fluorescent Proteins

First isolated from the jellyfish *Aequorea Victoria*, GFP[54] has been a revelation in fluorescence imaging and cell biology. Its importance was perhaps best highlighted in 2008, when Martin Chalfie, Osamu Shimomura, and Roger Y. Tsien were awarded the Nobel Prize for their discovery and development of GFP.[55]

In 2004, GFPs with engineered cysteines introduced into their beta-barrel structures (figure 1.16), so-called redox-active GFPs (roGFPs), were presented as a novel tool with which to monitor IRP.[10,11]

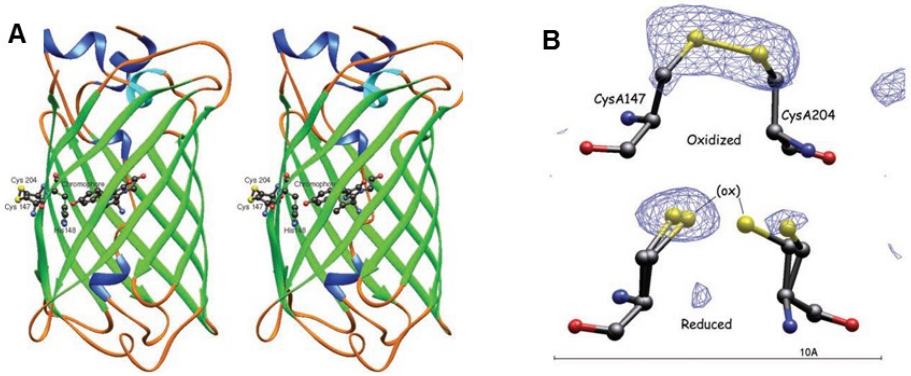

Figure 1.16: Crystal structures showing **(A)** the β-barrell secondary structure of roGFP and **(B)** the roGFP active-site with its two redox-active cysteine residues .[11]

roGFPs possess two fluorescence excitation maxima at around 400 and 490 nm.[10,11] These maxima display ratiometric changes in fluorescence intensity depending on the oxidation state(s) of the engineered cysteine residues (figure 1.17). This ratio can be mathematically linked to the Nernst equation, from which numerical RP values can be obtained.[10,11]

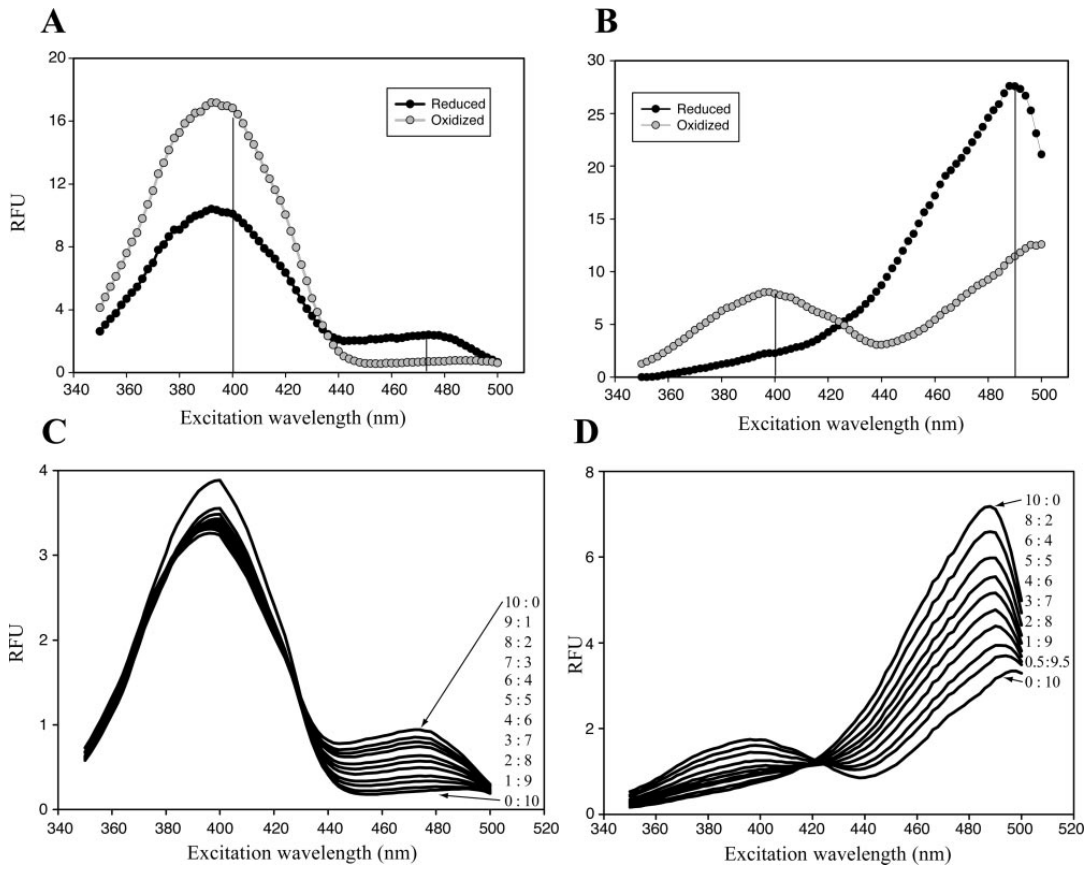

Figure 1.17: Excitation spectra for fully oxidized and reduced **(A)** roGFP1 and **(B)** roGFP2. Emission was monitored at 515 nm. **(C)** Titration of roGFP1 (1 μM) with dihydrolipoate + lipoate buffers (total 10 mM) and **(D)** titration of roGFP2 (1 μM) with reduced + oxidized Bis(2-mercaptoethyl)sulfone (BMES) (total 10 mM).[10]

Regarding monitoring IRP, roGFPs are the current 'gold standard'. They are non-toxic, accurate and can monitor RP changes reversibly and in real-time from single cells.[12] Despite their obvious benefits, roGFPs have limitations. Measurements can only be made in a narrow potential window (roGFPs have standard reduction potentials between -290 and -230 mV vs. NHE)[10,11,12] and they have been demonstrated to be insufficiently stable to oxidation to measure the potential of ER or endosomal compartments and are, therefore, unlikely to be useful for studies of oxidative stress.[12] Furthermore, protein engineering offers little scope for useful modification of these molecules for extension to wider potential ranges.

While it may be the cell's main redox governor, GSH is not the only molecular system that it harbours to modulate RP and maintain homeostasis. In order to report an overall 'global' IRP value, the other systems outlined on pages 10-11 should also be accounted for. Indeed, roGFPs (and many of the other techniques described in section 1.3) are specific for GSH and fail to consider the contributions of the other systems to IRP.

1.4 An Alternative Approach to Intracellular Redox Monitoring

With regard to live cellular imaging, fluorescence has long been the dominant spectroscopic technique used in academia and industry. While it is a well established and highly sensitive analytical technique, it does have several disadvantages when applied to cellular studies. For instance, molecules have to be 'tagged' with fluorophores which may be susceptible to photo-bleaching.[56] Often, fluorescence is limited to the visible region of light, where cells absorb and may be damaged.[57,58] Specificity is also an issue; broad spectral fluorescence can be prone to error caused by spurious background signals.[59] Furthermore, its potential for multi-plexing is limited.[59]

Surface enhanced Raman spectroscopy (SERS) offers an attractive and viable alternative to fluorescence in live cellular studies.

1.4.1 Raman Spectroscopy

In 1928, two Indian scientists, C.V. Raman and K.S. Krishnan reported the inelastic scattering of light.[60] Today this phenomenon is known as Raman scattering (figure 1.18).

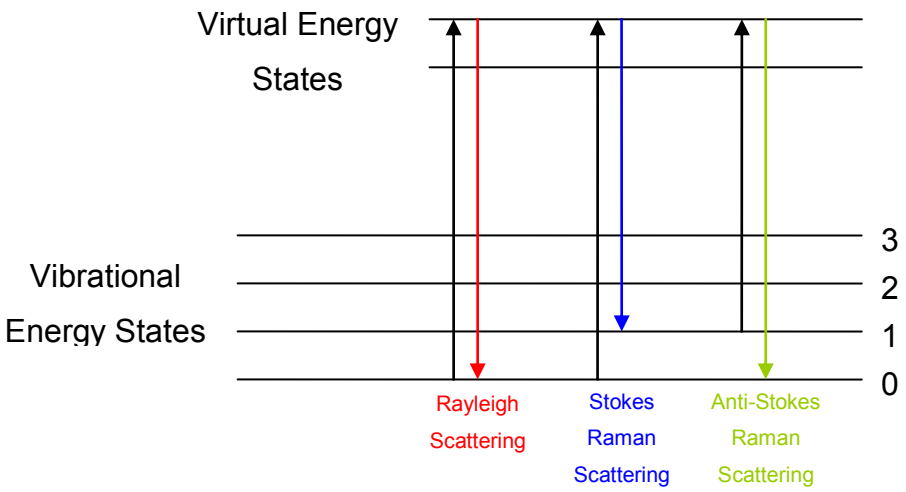

Figure 1.18: Energy level diagram showing the Rayleigh and Raman scattering processes. In Rayleigh or elastic scattering (red line), re-radiated photons possess the same energy as incident photons. In Raman or inelastic scattering, however, there is a shift in energy. Stokes scattering (blue line) results in photons being re-radiated with less energy while anti-Stokes scattering sees re-radiated photons gain energy.

In scattering, photons interact with a molecule's electron cloud around the nuclei, distorting it and leading to the formation of a short-lived 'virtual state'. These so called 'virtual states' are, however, unstable and photons are quickly re-radiated. The majority of re-radiated photons have the same energy as the incident photons interacting with the molecule. This type of scattering is known as elastic or Rayleigh scattering and is by far the most dominant form of light scattering. When energy is transferred between the molecule and the photon, an energy difference is created between the incident and re-radiated photons. This is inelastic or Raman scattering. In Raman scattering, energy can be transferred from the incident photon to the molecule, resulting in Stokes scattering, which is the strongest form of Raman scattering. Stokes scattered photons are emitted at a lower energy than the incident photons. The difference in energy according to Boltzmann's distribution means that some molecules may be present in an excited vibrational state; it is, therefore, possible for the energy of the excited state to transfer to the scattered photon. Anti-Stokes scattered photons are emitted at a higher energy than the incident photons. In

Raman spectroscopy, it is the shift in vibrational frequency (and energy) of the scattered photons from the incident photons that is measured and reported on.[61]

While Raman spectroscopy is similar to infrared (IR) spectroscopy, in that they both report on a molecule's vibrational frequencies, there are some key differences between the two. In order for a vibration to be Raman active, analytes must undergo a change in polarisability. In Raman spectroscopy, symmetric vibrations are strongest. For a vibration to be IR active, analytes must undergo a change in dipole moment. In IR spectroscopy, asymmetric vibrations are strongest.[61]

IR is a long-established analytical technique. With cheaper and simpler instrumentation, it may seem more attractive than Raman as a vibrational spectroscopy. However, Raman spectroscopy offers users numerous key advantages over IR spectroscopy. Minimal sample preparation is required for Raman analysis and fingerprint spectra of analytes can be obtained in seconds. Raman spectroscopy can also be used for remote sampling and allows samples to be analysed in glass or polymer packaging. It is relatively insensitive to water, making it ideal for biological analyses. Also, as it grows in popularity, cheaper high-performance, Raman spectrometers have become more readily available.[61]

Arguably, the main disadvantage of Raman spectroscopy is the fact that the Raman effect is weak. Roughly, only 1 in 10 million photons that are scattered by molecules are actually Raman scattered (the vast majority are elastically scattered).[61] Fortunately, the Raman effect can be enhanced.

1.4.2 Surface Enhanced Raman Scattering

SERS was first reported in 1974 by Fleischmann *et al*,[62] when they curiously observed an enhancement of Raman signal from pyridine molecules adsorbed on a roughened silver surface. Since then, enhancements of Raman signal on the order of 10^{14} have been claimed with SERS[63] and its popularity has been steadily growing (particularly in biochemical analyses).

As suggested by the name, SERS is a surface-sensitive technique. Enhancement of Raman signal occurs when analytes are in close proximity with a metal surface (most commonly, silver or gold nanoparticles), which provides a localised surface plasmon resonance (SPR). SPR occurs when a metal nano-structure has its surface electrons excited by light with a wavelength corresponding to the resonance frequency of the surface plasmons (collective oscillations of the surface electrons).[61]

The exact mechanics of how SERS takes place is still a matter of debate in the literature. However, there are two generally accepted theories as to how SERS occurs: electromagnetic enhancement and chemical enhancement.

(1) **Electromagnetic enhancement** – This theory describes an interaction between analytes adsorbed or held close to the metal surface and surface plasmons. Concisely, it describes an increase in the local electric field (equation 1.2) provided by the surface and experienced by the analyte.[61]

$$E_r = E_0 \cos \Theta + g\,(a^3/r^3)\, E_0 \cos \Theta$$

Equation 1.2: Description of the electric field at the surface of a metal sphere. Where: Er is the total electric field at a distance r from the sphere; a is the radius of the sphere; Θ is the angle relative to the direction of the electric field; and g is a constant (related to the dielectric constants).

In order for a molecule to experience an increase in polarisability, and thus Raman cross-section, it has to be orientated perpendicular to the metal surface.[61] It has also been shown that, while SERS can be observed from single nanoparticles,[63] greater enhancements are obtained from the junctions between particles in aggregates, where large electric fields are generated.[64]

(2) **Chemical enhancement –** This theory involves CT between the analyte and metal surface. Through chemical bond formation electrons and holes can be

transferred from the metal into the analyte. This serves to increase the polarisability of the analyte and thus lead to an increase in Raman signal.[61]

Owing to its high sensitivity, relative simplicity, insensitivity to water and potential for multi-plexing, it has been demonstrated that SERS is a viable alternative to fluorescence in cellular imaging and biochemical analysis.[59,65,66]

1.4.3 Gold Nanoshells

Today, colloidal suspensions of gold nanoparticles ranging in size from ~5-100 nm are among the most common SERS substrates. While these can and have been used for intracellular SERS experiments there is now an alternative class of gold nanoparticle (gold nanoshells) which offers several distinct advantages over colloidal gold. Gold nanoshells (NS) are a class of tuneable gold nanoparticle, comprising a dielectric core (silica) surrounded by a thin metallic (gold) shell.[67] NS are ideal substrates for intracellular SERS measurements, because they exhibit a strong, tuneable plasmon resonance in the near IR region (where cells absorb poorly) and exhibit low auto-fluorescence (figure 1.19).[68] It is well known that, regarding SERS from colloidal gold nanoparticles, enhancements in Raman scattering are greater when the particles are aggregated and there is overlap of the surface plasmons.[64] Plasmon overlap creates an enhanced electric field and leads to formation of local 'hot spots'.[64] With the hybridisation of the core and shell plasmons, NS are known to generate stronger SERS signals, compared to unaggregated homogenous nanoparticles. Additionally, it has been demonstrated that NS can be controllably delivered into cells without any cytotoxic side effects.[71]

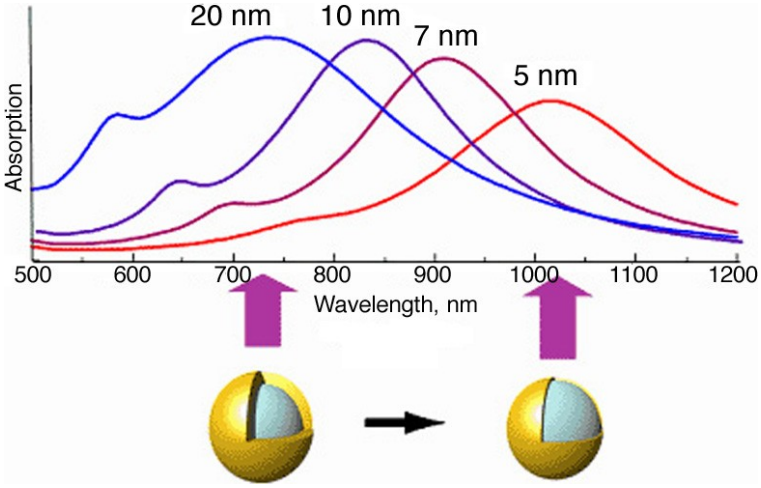

Figure 1.19: NS and their tuneable plasmon resonances. By varying the core:shell ratio the wavelength of the plasmon resonance can be tuned. Increasing the core:shell ratio by decreasing the shell radius from 20 to 5 nm results in a redshift of the plasmon resonance.[69]

1.5 Project Aims

The main aims of the project were:

(1) To design and characterise nanosensors with SERS fingerprints that are sensitive to changes in oxidation state.

Inspired by the previous work of Bishnoi *et al*, who demonstrated that pH changes could be accurately monitored through the SERS spectra of para-mercaptobenzoic acid (pMBA),[70] a range of probe molecules whose SERS spectra were expected to change with potential had to be synthesised and assembled on gold nanoparticles. A series of spectroelectrochemical proof of concept experiments also had to be designed and undertaken.

(2) To investigate the controlled delivery and toxicity of nanosensors.

Previous studies by the Campbell group, showing the unrestricted endocytotic uptake of nanoparticles by cells, were built upon.[71] It was important to establish that the introduction of nanosensors would not produce any toxic side-effects which might adversely affect IRP. Targeted delivery of nanoparticles to nuclei was also investigated.

(3) To monitor IRP changes inside cells from discrete locations in real-time.

This was the ultimate goal of the research. The ability of these nanosensors to monitor RP changes inside cells, as they responded to super-physiological stimuli and during relevant physiological events, was carefully investigated.

Chapter 2

Materials and Methods

All chemicals and reagents, unless otherwise stated, were purchased from Sigma Aldrich and used without further purification. Solvents were purchased from Fisher Scientific.

2.1 Synthetic Work

2.1.1 Probe Molecule Synthesis

All nuclear magnetic resonance (NMR) spectra were recorded using a Bruker AVA 500 MHz spectrometer and analysed with MestReC v4.5.2 software.

All melting points were recorded using Gallenkamp capillary tube melting point apparatus.

Analytical thin layer chromatography (TLC) was performed on pre-coated silica TLC plates (0.25 mm thickness). Dry-flash column chromatography was carried out on silica gel (grade 60, 230-400 mesh, 60 Å). TLC plates and silica gel were purchased from Merck.

2.1.1.1 Bis-(2-Anthraquinone carboxamide) (AQ)

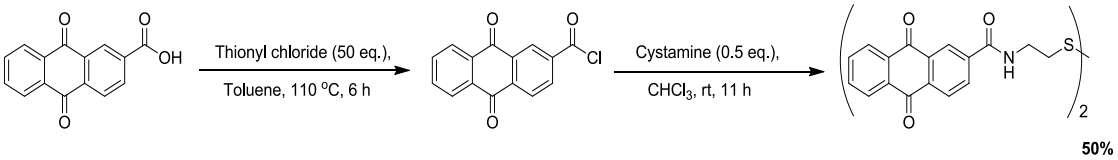

Scheme 2.1: Synthesis of AQ. Anthraquinone-2-carbonyl chloride is first made from anthraquinone-2-carboxylic acid and is subsequently reacted with cystamine to yield the product AQ.

126 mg of AQ were synthesised in 50% yield according to the procedure outlined by Nagata *et al*:[72] mp 219-221 ºC; ^{1}H NMR (500 MHz, $CDCl_3$) δ_H 3.13-3.16 (t, ^{3}J 6.3, 4H), 3.92-3.97 (q, ^{3}J 6.3, 4H), 7.41 (b s, 2H), 7.78-7.82 (m, 4H), 8.22-8.37 (m, 8H), 8.62 (s, 2H); ^{13}C NMR (500 MHz, $CDCl_3$) δ_C 37.98, 39.90, 125.29, 127.33, 127.36, 127.87, 133.24, 133.34, 134.34, 134.41, 135.16, 139.16, 166.27, 182.41.

2.1.1.2 1,8-diaza-4,5-dithia-1,8-di(2-chloro-[1,4]-naphthoquinone-3-yl)octane (NQ)

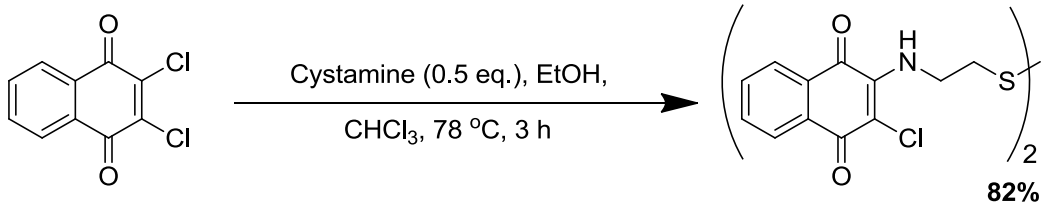

Scheme 2.2: Synthesis of NQ via a substitution reaction of 2,3-dichloro-1,4-naphthoquinone with cystamine.

582 mg of NQ were synthesised in 82% yield according to the procedure outlined by Nagata *et al*:[72] mp 193-195 ºC; ^{1}H NMR (500 MHz, $CDCl_3$) δ_H 3.02-3.05 (t, ^{3}J 6.5, 4H), 4.21-4.25 (q, ^{3}J 6.5, 4H), 6.34-6.43 (b s, 2H), 7.64-7.78 (m, 4H), 8.06-8.18 (m, 4H); ^{13}C NMR (500 MHz, $CDCl_3$) δ_C 38.64, 43.12, 126.09, 126.98, 129.76, 132.53, 132.67 135.04, 143.84, 178.876, 180.33.

2.1.1.3 2-Mercaptohydroquinone (HQ)

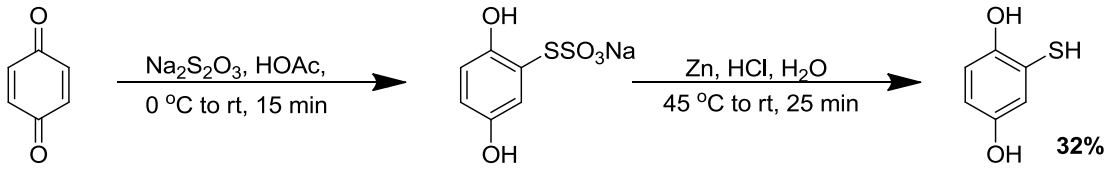

Scheme 2.3: Synthesis of HQ. Sodium thiosulfate is first added to benzoquinone before the intermediate is reduced to form the product HQ.

247 mg of HQ were synthesised in 32% yield according to the procedure outlined by Monks *et al*:[73] mp 112-114 ºC; ^{1}H NMR (500 MHz, $CDCl_3$) δ_H 3.12 (s, 1H), 4.67 (s, 1H), 5.73 (s, 1H), 6.69-6.96 (m, 3H); ^{13}C NMR (500 MHz, $CDCl_3$) δ_C 113.09, 115.73, 117.19, 121.10, 149.01, 149.84.

2.1.1.4 *N*-(2-mercaptoethyl) ferrocene carboxamide (FCBX)

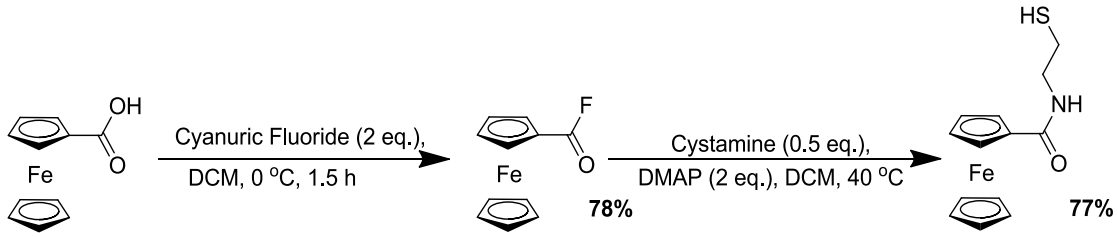

Scheme 2.4: Synthesis of FCBX. Fluorocarbonyl ferrocene is first made from ferrocene carboxylic acid and is subsequently reacted with cystamine to yield the product FCBX.

202 mg of FCBX were synthesised in 77% yield according to the procedure outlined by Schön *et al*:[74] mp 207 ºC; ^{1}H NMR (500 MHz, $CDCl_3$) δ_H 1.26 (b s, 1H), 2.99-3.01 (t, ^{3}J 6.3, 2H), 3.72-3.74 (t, ^{3}J 6.3, 2H), 4.26 (s, 5H), 4.38-4.40 (m, 2H), 4.79-4.81 (m, 2H), 6.95 (b s, 1H); ^{13}C NMR (500 MHz, $CDCl_3$) δ_C 35.21, 41.89, 72.15, 71.93, 69.99, 165.24.

453 mg of fluorocarbonyl ferrocene were synthesised as an intermediate in 78% yield according to the procedure outlined by Galow *et al*:[75] ^{1}H NMR (500 MHz, $CDCl_3$) δ_H 4.25 (s, 5H), 4.50-4.52 (m, 2H), 4.78-4.80 (m, 2H).

2.1.2 Nuclear Localisation Sequence (NLS) Peptide Synthesis

9-fluorenylmethyloxycarbonyl (Fmoc)-protected AAs, Rink amide linker and 2-(1H-Benzotriazole-1-yl)-1,1,3,3-tetramethyluronium hexafluorophosphate (HBTU) were purchased from GL Biochem.

Peptide purity was assessed by HPLC, using an Agilent 1100 series HPLC coupled with an evaporative light-scattering detector (ELSD) (Polymer Labs ELS-1000 detector).

Matrix-assisted laser desorption/ionization–time-of-flight (MALDI-TOF) mass spectra were recorded on a Voyager-DE^{TM} STR MALDI-TOF mass spectrometer (Applied Biosystems), with a matrix solution of sinapinic acid (10 mg/ml) in 49.9% H_2O, 50% acetonitrile (MeCN), 0.1% trifluoroacetic acid (TFA).

2.1.2.1 Synthesis of Fluorescein-aminohexanoic acid-PKKKRKVC (CA-NLS 1)

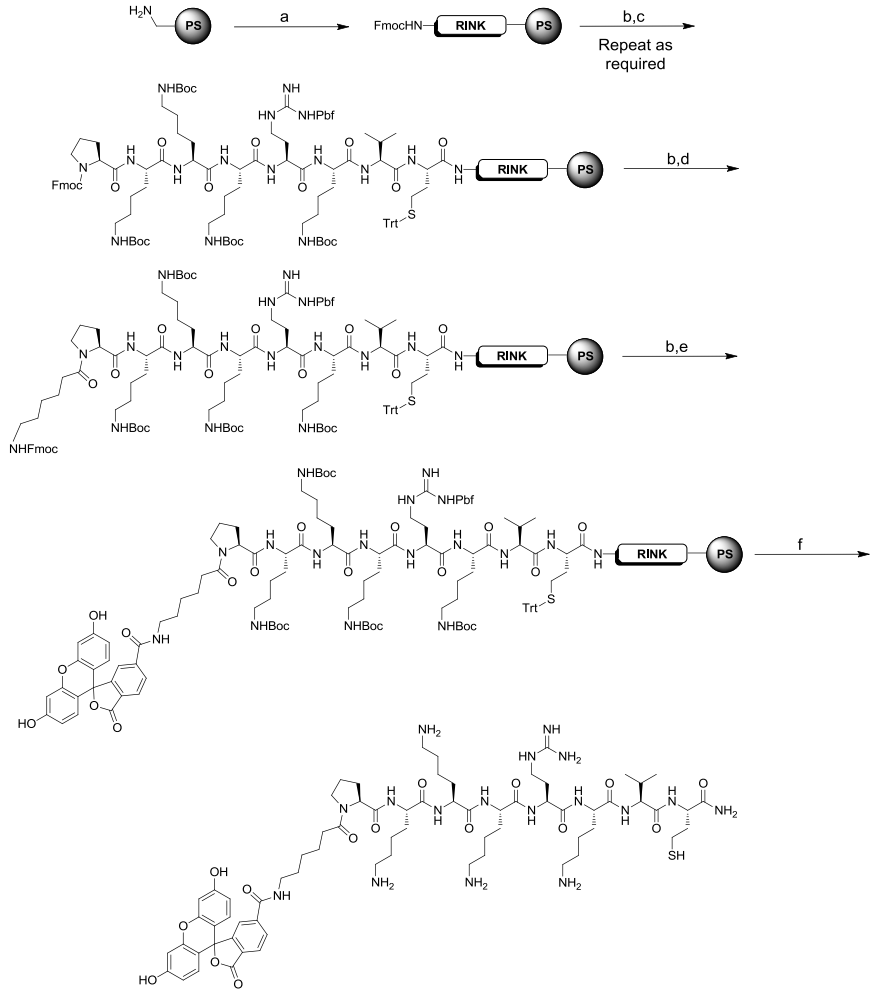

Scheme 2.5: Synthesis of CA-NLS 1. Reagents and Conditions: a) Rink amide linker (3 eq.), oxyma (3 eq.), diisopropylcarbodiimide (DIC) (3 eq.), 0.1 M in dimethylformamide (DMF), 3 h; b) 20% piperidine in DMF (2 x 5 min); c) AA (3 eq.), oxyma (3 eq.), DIC (3 eq.) 0.1 M in DMF, 1 h; d) *N*-Fmoc-6-aminohexanoic acid (3 eq.), oxyma (3 eq.), DIC (3 eq.), 0.1 M in DMF, 3 h; e) 5(6)-carboxy fluoroscein (3 eq.), oxyma (3 eq.), DIC (3 eq.), 0.1 M in DMF, 3 h f) 90% TFA, 5% triisopropylsilane (TIS), 5% dichloromethane (DCM), 3 h.

General conditions: All coupling reactions were carried out at rt unless otherwise stated. Solid-phase synthesis was performed manually using an Isolute filtration reservoir as the reaction vessel, fitted with polyethylene frits (Argonaut Technologies Inc). AAs were Fmoc protected, at the *N* terminus, with suitable acid labile protecting groups on the side chains. Each coupling step of the synthesis was assessed for completion using either the Kaiser test for primary amines, or the chloranil test for secondary amines.[76]

Kaiser Test: Solution 1: 80 g phenol in 20 ml ethanol (EtOH); Solution 2: 2 ml 0.001 M aqueous KCN in 98 ml pyridine (Solution 1 and 2 combined make Solution A); Solution 3: 5 g Ninhydrin in 100 ml EtOH. (Solution B).

Three drops Solution A and one drop Solution B were added to a few resin beads. The mixture was heated at 100 ^{o}C for 3 mins and the colour of the solution and beads was observed.

- Positive result: Resin/solution light to dark blue, i.e. primary amine present.
- Negative result: Resin/solution colourless/light yellow, i.e. no primary amine present.

Chloranil Test: Stock solutions should be kept in the refrigerator for no longer than one month. Solution A: 2% acetaldehyde in DMF; Solution B: 2% chloranil in DMF. Two drops of Solution A and two drops of Solution B were added to a few resin beads. The mixture was heated at 100 ^{o} C for 3 mins and the colour of the solution and beads was observed.

- Positive result: Resin/solution dark blue to green, i.e. primary or secondary amine present.
- Negative result: Resin/solution colourless/light yellow, i.e. no primary or secondary amine present.

Coupling the linker to the resin: Aminomethyl polystyrene resin (loading 1.23 mmol/g, 0.20 g, 0.246 mmol) in a 6 ml reaction vessel was swollen for 5 mins in DCM (3 ml) and then washed with DCM (3 x 3 ml). To a solution of rink amide linker (399 mg, 0.74 mmol) in DMF (2.46 ml), oxyma (105 mg, 0.74 mmol) was added and the solution shaken for 10 mins. DIC (116 µl, 0.74 mmol) was added and the solution shaken for 2 mins. The mixture was added to the resin and shaken for 3 h. The resin was filtered and washed with DMF (3 x 4 ml), DCM (3 x 4 ml) and methanol (MeOH) (3 x 4 ml). Kaiser test negative. The resin was washed with Et_2O (3 x 4 ml) and dried under vacuum for storage.

Coupling of AAs: The resin in a 6 ml reaction vessel was swollen for 5 mins in DCM (2.5 ml) and filtered. A solution of 20% piperidine in DMF (2.5 ml) was added, the vessel was shaken for 5 mins and the resin was filtered and washed with DMF (3 x 3 ml) and DCM (3 x 3 ml). Piperidine deprotection and washing cycle was repeated and the resin was dried under vacuum. Kaiser test positive. To a solution of the appropriate AA (0.74 mmol) in DMF (2.46 ml) was added oxyma (105 mg, 0.74 mmol) and the solution shaken for 10 mins. DIC (116 µl, 0.74 mmol) was added and the solution shaken for 2 mins. The mixture was added to the resin and shaken for 1 h. The resin was filtered and washed with DMF (3 x 3 ml), DCM (3 x 3 ml) and MeOH (3 x 3 ml). Kaiser test negative. Otherwise treatment of activated AA was repeated.

Attachment of spacer to 8-mer resin: Resin (~0.246 mmol) in a 3 ml reaction vessel was swollen for 5 mins in DCM (2.5 ml) and filtered. A solution of 20% piperidine in DMF (2.5 ml) was added. The vessel was shaken for 5 mins and the resin was filtered and washed with DMF (3 x 3 ml) and DCM (3 x 3 ml). Piperidine deprotection and washing cycle was repeated and the resin was dried under vacuum. To a solution of N-(Fmoc)-6-aminohexanoic acid (262 mg, 0.74 mmol) in DMF (2.46 ml) was added oxyma (105 mg, 0.74 mmol) and the solution shaken for 10 mins. DIC (116 µl, 0.74 mmol) was added and the solution shaken for 2 mins. The mixture was added to the resin and then shaken for 3 h. The resin was filtered and

washed with DMF (3 x 4 ml), DCM (3 x 4 ml) and MeOH (3 x 4 ml). Chloranil test negative.

Attachment of Fluorescein to Spacer-8-mer resin: Resin (~0.246 mmol) in a 6 ml reaction vessel was swollen for 5 mins in DCM (2.5 ml) and filtered. A solution of 20% piperidine in DMF (2.5 ml) was added. The vessel was shaken for 5 mins and the resin was filtered and washed with DMF (3 x 3 ml) and DCM (3 x 3 ml). Piperidine deprotection and washing cycle was repeated and the resin was dried under vacuum. To a solution of 5(6)-carboxyfluorescein (272 mg, 0.74 mmol) in DMF (2.46 ml) was added oxyma (105 mg, 0.74 mmol) and the solution shaken for 10 mins. DIC (116 μL, 0.74 mmol) was added and the solution shaken for 2 mins. The mixture was added to the resin and shaken for 3 h. The resin was filtered and washed with DMF (3 x 4 ml), DCM (3 x 4 ml) and MeOH (3 x 4 ml). Process was repeated until negative Kaiser test obtained. The resin was swollen in DCM (3 ml) and washed with 20% piperidine in DMF (2 x 2.5 ml), DMF (6 x 2.5 ml), DCM (6 x 2.5 ml) and MeOH (6 x 2.5 ml). The resin was washed with Et_2O (3 x 2.5 ml), dried under vacuum and stored in the dark.

Cleavage from resin: Resin (~0.246 mmol) in a 6 ml reaction vessel was swollen for 5 mins in DCM (2 ml) and filtered. A solution of TFA:TIS:DCM (90:5:5, 3 ml) was added, and the vessel was shaken for 3 h. The resin was removed by filtration, and ice-cold Et_2O (30 ml) was added to the filtrate. The resultant solid was pelleted by centrifugation, and the solvent removed by decantation. Solid was dried under vacuum.

Purification: CA-NLS 1 was purified using an Aglinet 1100 series HPLC:

- Column: Phenomenex prodigy 5u C18, 250 × 10 mm, 5 μm.
- Solvent: A-MeCN + 0.1% formic acid, B-H_2O + 0.1% formic acid.
- Method: 5%-95% A in B over 18 min, 2 min isocratic elution, 2 min to 5% A, 2 min isocratic elution.

CA-NLS 1 Characterisation Data: Yellow solid; HRMS (MALDI-TOF) $C_{70}H_{105}N_{17}O_{15}S$ calc 1455.7783, found 1455.9723; ELSD retention time - 2.62 min (98% pure).

2.1.2.2 Synthesis of CGGPKKKRKVGG (CA-NLS 2)

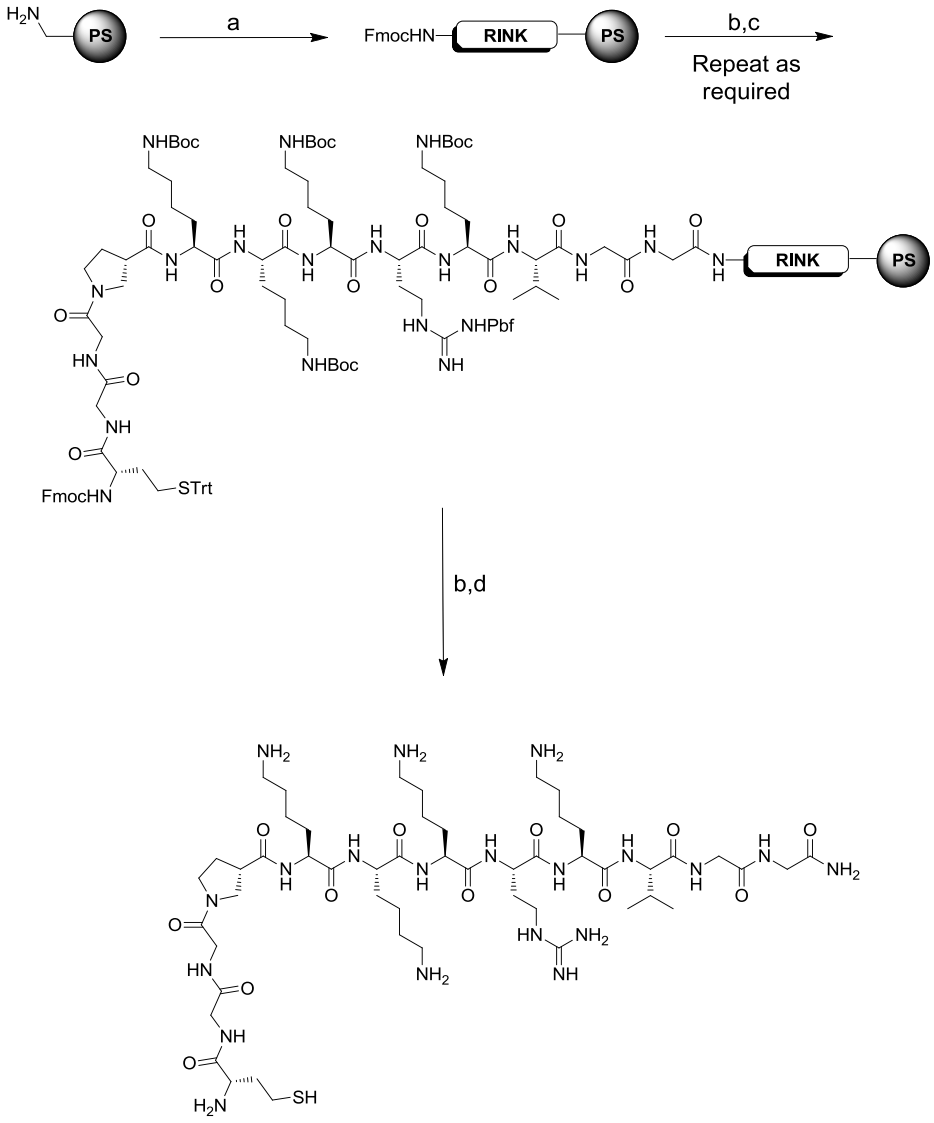

Scheme 2.6: Synthesis of CA-NLS 2. Reagents and conditions: a) Rink amide linker (3 eq.), oxyma (3 eq.), DIC (3 eq.), 0.1 M in DMF, 3 h; b) 20% piperidine in DMF (2 x 2 min); c) AA (0.2 M), HBTU (0.5 M), *N*,*N*-diisopropylethylamine (DIPEA) (2 M in *N*-methylpyrrolidone (NMP)), 0.1 M in DMF, 1 h; d) TFA, 5% TIS, 5% DCM, 3 h.

Solid-phase synthesis was performed using a CEM microwave peptide synthesiser. AAs were Fmoc protected at the *N* terminus, with suitable acid labile protecting groups on the side chains. All AA coupling reactions were carried out at 60 ºC unless otherwise stated.

CA-NLS 2 was synthesized by solid phase methods, using standard Fmoc chemistry and a CEM Liberty microwave peptide synthesiser. Rink amide linker (399 mg, 0.74 mmol) was coupled to aminomethyl PS resin (loading 1.23 mmol/g, 0.20 g, 0.246 mmol), as described on page 28. After removal of the Fmoc-group using 20% piperidine in DMF, chain elongation was performed with Fmoc-Gly-OH, Fmoc-Gly-OH, Fmoc-Val- OH, Fmoc-Lys(Boc)-OH, Fmoc-Arg(Pbf)-OH, Fmoc-Lys(Boc)-OH, Fmoc-Lys(Boc)-OH, Fmoc-Lys(Boc)-OH Fmoc-Pro-OH, Fmoc Gly-OH, Fmoc Gly-OH and Fmoc-Cys(Trt)-OH (each 0.2 M,), using 20% piperidine/DMF for Fmoc deprotection, HBTU (0.5 M) for activation, DIPEA (2 M in NMP) as base and DMF as solvent. After assembly of the linear peptide chain, the resin was transferred in several ml of DMF into a 6 ml Isolute filtration reservoir. The peptide was cleft from the resin, using TFA:TIS:DCM (90:5:5 3 ml). The resin was removed by filtration and ice-cold Et_2O (30 ml) was added to the filtrate. The resulting solid was pelleted by centrifugation and the solvent removed by decantation. Solid was dried under vacuum. No purification was necessary.

CA-NLS 2 Characterisation Data: White solid; HRMS (MALDI) $C_{51}H_{96}N_{20}O_{12}S$ calc 1213.0753, found 1213.1288; ELSD retention time – 0.52 min (100% pure).

2.2 SERS Experiments

2.2.1 General SERS Microscopy Information

All SERS spectra were recorded with a Renishaw inVia Raman Microscope and Spectrometer. A 785 nm diode laser with ~6 mW power at the sample was used, along with a 50 × Olympus Long Working Distance objective (NA = 0.45), to focus laser light onto the gold nanoshells (NS). All SERS spectra were processed using WIRE^{TM} 2.0 software. Aqueous suspensions of NS (3×10^{9} NS/ml, 5 pM) were purchased from Nanospectra Biosciences. NS were resonant at 780 nm and had a 125 nm silica core and a 25 nm gold shell thickness. Aqueous suspensions of gold nanorods (NR) (6.1×10^{11} NR/ml, 1 nM) were purchased from Nanopartz. NR were resonant at 770 nm and had a 10 nm axial diameter and a 38 nm length.

2.2.2 NS and NR Functionalisation

NS were functionalised via overnight incubation of 1 mM solutions of HQ, NQ and AQ at rt. Solutions of HQ and FCBX were aqueous, whereas NQ and AQ were water:EtOH mixtures (9:1) and contained 5 mM tris(2-carboxyethyl)phosphine (TCEP). All NS were washed twice with distilled water after functionalisation. NR were functionalised with CA-NLS 1 and CA-NLS 2 via 72 h incubation in 0.1 mM aqueous peptide solutions. All NR were washed twice with distilled water after functionalisation. UV-Vis analysis was used to confirm attachment of analytes.

2.2.3 SERS Characterisation of NLS Peptides

SERS spectra were recorded for NLS peptides from the surface of NS, immobilised on aminosiloxane functionalised glass microscope slides. 5 µl of NS solution (100 fM) were deposited on the slides. Water was left to evaporate, before 7.5 µl of coating solution (1 mM) were deposited over the NS. After overnight incubation at rt, slides were washed with distilled water to remove any loosely adsorbed

molecules. SERS spectra were acquired over 10 s and between a Stokes Raman shift range of 600-1800 cm^{-1}. Vibrational assignments were made according to the literature.

2.2.4 Spectroelectrochemistry

3-Mercatopropionic acid (2 µl of a 5 mM ethanolic solution) was deposited onto the surface of gold microfabricated electrodes, which were incubated overnight at rt. The electrodes were carefully rinsed with water and allowed to dry at rt. Aqueous 1-ethyl-3-(3-dimethylaminopropyl)carbodiimide (EDC) solution (2 µl of a 24 mM solution) was deposited on the surface of the electrodes, which were incubated for 30 min at rt. The electrodes were rinsed carefully with water and allowed to dry at rt. Poly-L-lysine solution (2 µl of a 0.1% (w/v) solution) was deposited onto the surface of the electrodes, which were incubated for a further 6 h at rt. After this time, 2 µl of NS (10 fM solution) were deposited onto the electrodes, which were subjected to a wash-dry step. Self assembled monolayers (SAMs) of the SERS reporters were formed on the NS by pipetting 2 µl of aqueous solutions of HQ, FCBX, or NQ (1 mM) onto the NS. As stated previously, solutions of NQ were incubated with 5mM TCEP. Electrodes were carefully rinsed with water, in order to remove any loosely adsorbed molecules and left to dry at rt.

Once functionalised with HQ, FCBX, or NQ, the gold microfabricated electrodes, along with a coiled platinum wire (0.1 mm diameter), serving as the auxiliary electrode, and coiled silver wire (0.5 mm diameter), serving as the reference electrode, were connected to Type III Autolab potentiostat, using GPES v4.9 software to control the potential. The electrodes were inserted into a 20 ml glass Petri dish which was charged with phosphate buffer (0.1 M, pH 7.4, 0.1 M KCl). SERS spectra were then recorded, from the surface of the electrodes, at varying potentials. SERS spectra were acquired over 10 s and between a Stokes Raman shift range of 200-1800 cm^{-1}. Vibrational assignments were made according to the literature and DFT calculations.

For the AQ probe molecule, 200 µl of a 10 fM solution of AQ-NS were pipetted into a well of a 96-well plate. Solution RP was varied according to the Nernst equation, using the $NADP^+$/NADPH redox couple. SERS spectra were recorded from the well at varying potentials. SERS spectra were acquired over 10 s and between a Stokes Raman shift range of 200-1800 cm^{-1}.

2.2.5 Redox Couple Solution Studies

For redox couple solution studies, 5 µl of NS solution (100 fM) were deposited onto aminosiloxane functionalised slides. Water was left to evaporate before 7.5 µl of NQ solution (1 mM, 9:1 H_20:EtOH, 5 mM TCEP) were deposited over the NS. RP was changed, using solutions in which ratios of reduced:oxidised species were altered with various redox couples according to the Nernst equation. Solution measurements were carried out in phosphate buffer (0.1 M, pH 7.4, 0.1 M KCl). For solution studies with NQ-NS, SERS spectra were acquired over 30 s and between a Stokes Raman shift range of 1340-1840 cm^{-1}.

2.2.6 Intracellular SERS Experiments

Cells were seeded at a density of 2×10^5 on 25 × 25 × 1 mm quartz coverslips (UQG Optics Ltd, UK) in 1 ml of media and incubated for 24 h. Functionalised NS (1,500 NS/cell, 249 fM) were then taken up by the cells through endocytosis in 2 ml of CS-free media overnight. In order to induce oxidative stress in cells, 2,2′ azobis-2-amidinopropane (AAPH) was introduced into the media at a concentration of 30 mM. In order to induce reductive changes in cells, dithiothreitol (DTT) was introduced into the media at a concentration of 1 mM. In order to induce apoptosis in cells, staurosporine was introduced into the media at a concentration of 1 µM (3 and 6 h incubations). MicroRNA (miRNA) mimics or inhibitors were reverse-transfected into cells at a final concentration of 25 nM in 0.4% DharmaFECT 1 (Thermo Fisher Scientific). miRNA sequences were obtained from miRBase and purchased from Thermo Fischer Scientific. For intracellular studies with HQ-NS, SERS spectra were acquired over 30 s and between a Stokes Raman shift range of 190-790 cm^{-1}. For

intracellular studies with NQ-NS, SERS spectra were acquired over 30 s and between a Stokes Raman shift range of 1340-1840 cm^{-1}. All spectra were processed using WIRE^{TM} 2.0 software.

2.3 Cellular Work

2.3.1 General Cell Culture Information

All cellular work was carried out using NIH/3T3 mouse fibroblast cells. Cells were cultured in Dulbecco's Modified Eagle's Medium (DMEM), supplemented with penicillin/streptomycin (10,000 units/ml), L-glutamine (200 mM) and 10% heat-inactivated calf serum (CS) (all Gibco). Cells were incubated at 37 ºC and 5% CO_2 in a humidified incubator.

When handling cells for passage, old media was removed and cells were washed with phosphate buffered saline (PBS). Cells were harvested via trypsination (1 ml) (trypsin/ethylenediaminetetraacetic acid (EDTA), Gibco) at 37 °C and 5% CO_2 for 3 mins. The detached cells were re-suspended in fresh growth media and pelleted by centrifugation at 1,100 rpm for 5 mins. Appropriate aliquots were re-seeded for continued growth.

When freezing cells for long term storage, cells were re-suspended in freezing media (90% culture media, 10% dimethyl sulfoxide (DMSO)). 1 ml aliquots (2×10^6 cells/ml) of re-suspended cells were pipetted into labelled 1.8 ml cryovials, transferred to a Nalgene Cryo 1 °C freezing container and stored overnight at -80 °C. The following day, cryovials were transferred into liquid N_2.

When thawing cells from liquid nitrogen storage, cryovials were removed from the liquid N_2 and the cells thawed slowly in a warm water bath (37 °C). The outside of the cryovial was disinfected with 70% EtOH, and its contents transferred to a clean 15 ml falcon tube, along with 10 ml of fresh media. The cells were centrifuged at

1,000 rpm for 5 mins and the supernatant discarded. The pellet was then re-suspended in 5 ml of fresh media and transferred to a new 25 cm^2 flask for culturing.

2.3.2 Haemocytometry

Cell densities were determined by haemocytometry. An aliquot (10 µl) of cells detached from a culture flask and collected media (total volume: 5 ml) was mixed with 0.2% trypan blue (40 µL, Sigma-Aldrich) and pipetted into a Bright Line™ haemocytometer (an etched glass device with an H-shaped moat forming two cell-counting areas, each with 4 quadrants and with surface features enhanced by Neubauer rulings).

Cell concentrations were determined by Equation 2.1.

$$C = (N/Q) \times 5 \times 10^4$$

Equation 2.1: Cell concentration formula. Where C = Concentration (cells/ml), N = Number of cells and Q = Number of quadrants counted.

2.3.3 DCFH-DA Assay

A 96-well plate divided into four sections (untreated cells, NQ/HQ-NS) (1,500 NS/cell, 149 fM), tBOOH +ve control (0.5 mM) and Zn +ve control (0.5 mM)) was seeded at a density of 12,000 cells per well in 200 µl of media. Cells were grown to ~60% confluence overnight and the media was changed to 2% CS. Cells were left to grow on overnight, until confluence was reached. Old media was removed and replaced with phenol-red, CS-free media. At this time, cells were treated with NQ/HQ-NS and positive controls overnight. Cells were washed twice with PBS. Old media was removed and replaced with phenol-red, CS-free media (100 µl) along with DCFH-DA (100 µl of a 40 µM solution). The plate was incubated for 30 mins. Following incubation with DCFH-DA, old media was replaced with fresh phenol-red, CS-free media. Fluorescence measurements were taken over a 24 h period at

intervals of 0, 1, 2, 3, 4, 5, 6 and 24 h, using a BioTek Synergy HT plate reader (excitation 485/20, emission 530/25 nm).

2.3.4 Total GSH and GSSG Assay

Cells were seeded at a density of 1.50×10^5 cells/well in a 6-well plate (2 ml/well) and allowed to reach confluence (approx 6×10^5 cells/well) over 48 h. The 6-well plate was divided into two sections (untreated and NQ/HQ-NS (1,500 NS/cell, 187 fM) treated cells). Cells were incubated overnight in CS-free media before being washed with PBS and harvested by trypsinisation. Harvested cells were subjected to deproteinisation with 0.1% Triton / 0.6% sulfosalicyclic acid in 0.1 M phosphate buffer with 5 mM EDTA (pH 7.5) (KPE) and homogenised by sonication. Cell debris was collected by centrifugation for 5 mins at 5,000 rpm 4 °C. Samples were stored on ice, prior to analysis of GSH content. GSH standards in KPE were prepared at concentrations of 8, 4, 2, 1, 0.5, 0.25 and 0.125 µg/ml by 2-fold serial dilutions of a 16 µg/ml stock solution. Solutions of 5,5'-dithiobis-(2-nitrobenzoic acid) (DTNB) and β-NADPH were also prepared in KPE at a concentration of 0.67 mg/ml, along with a GR solution, which was prepared at a concentration of 14 µl/ml in KPE. Standards and samples were added to the wells of a 96-well plate. Equal volumes of DTNB and GR solutions were mixed together and 120 µl of this mixture were added to each well. After incubating at rt for 30 s to allow for conversion of GSSG to GSH, 60 µl of β-NADPH solution were added to each well. Absorbance values were then read at 412 nm using a BioTek Synergy HT plate reader. From the absorbance values, the rate of 2-nitro-5-thiobenzoic acid formation was calculated and, using linear regression, total GSH concentrations were calculated in triplicate. GSH concentrations were expressed in µM/mg of protein (as determined by the bicinchoninic acid assay (BCA)). GSH standard and GR were purchased from Cayman Chemical Company.

Exclusive quantification of GSSG was achieved by derivatising GSH with 2-vinylpyridine. After deproteinising cells, 5 µl of 2-vinylpyridine were added per ml of extraction buffer. The remainder of the assay was carried out as normal.

2.3.5 BCA Protein Assay

Pierce BCA protein assay was carried out according to the manufacturer's instructions.[77] Briefly, 10 µl of cell lysate were added to the wells of a 96-well plate containing 100 µl of working reagent. The plate was incubated for 30 mins at 37 °C, allowed to cool to rt. Absorbances were then measured at 562 nm, using a BMG Labtech Polarstar microplate reader. Protein concentrations were determined from a standard curve, using bovine serum albumin (BSA) standards. The working range of BSA standards used was 25-1500 µg/ml. Working reagent and BSA standard were purchased from Thermo Fischer Scientific.

2.3.6 APO*Percentage* Apoptosis Assay

APO*Percentage* apoptosis assay was carried out according to the manufacturer's instructions.[78] Briefly, selected wells of a 96-well plate were seeded with cells at a density of 12,000/well (200 µl/well). Cells were allowed to settle and were incubated for 3 h. Old media was removed. Cells were washed three times with PBS and then incubated overnight in CS-free media with NQ/HQ-NS (1,500 NS/cell, 149 fM) or for 3 h with staurosporine (1 µM). Cells were carefully washed three times with CS-free media before wells were charged with 100 µl of fresh CS-free media and 5 µl of APO*Percentage* Dye. After 30 mins incubation, cells were washed three times in PBS. Fluorescence measurements were recorded, using a BMG LabTech Fluostar Galaxy microplate reader (excitation 485/20 nm, emission 530/25 nm).

2.3.7 Apo-ONE Apoptosis Assay

Apo-ONE apoptosis assay was carried out according to the manufacturer's instructions.[79] Briefly, selected wells of a 96-well plate were seeded with cells at a density of 12,000/well (200 µl/well). Cells were allowed to settle and were incubated for 3 h. Old media was removed. Cells were washed three times with PBS and then incubated for 5 h with concentrations of H_2O_2 ranging from 0-10 mM. Cells were carefully washed three times with CS-free media before wells were charged with 100

µl of fresh CS-free media and 100 µl of Apo-ONE Caspase-3/7 Reagent. After 3 h incubation, cells were washed three times in PBS. Fluorescence measurements were recorded, using a BMG LabTech Fluostar Galaxy microplate reader (excitation 485/20 nm, emission 530/25 nm).

2.3.8 MTT Assay

Cells were seeded at a density of 6,000/well (columns 2, 4 and 6 and rows A-H) in a 96-well plate (100 µL per well). Column 8 was used as a blank (no cells). Cells were incubated for 24 h prior to NQ/HQ-NS (1,500 NS/cell, 75 fM) / NR-NLS (6,000 NR/cell, 300 fM) treatment in CS-free media for 24 h. After the desired incubation time, old media was removed, cells were washed twice with PBS and the wells charged with fresh phenol-red free media (90 µL). 10 µL of MTT at concentration of 5 mg/ml in PBS was added to each well. Cells were incubated for 3 h, prior to dissolution of the formed formazan, using 100 µL of the MTT solubilising solution (10% TRITON X-100, 0.1 N HCl in IPA) and gently shaking until total dissolution of the crystals. Absorbance values were read, on a BIO-RAD Benchmark microplate reader, at 570 nm and cellular viability was calculated according to equation 2.2.

$$\% \text{ Cell Viability} = (A_{570\ Exp} / A_{570\ Control}) \times 100$$

Equation 2.2: Cell viability formula. Where $A_{570\ Exp}$ = Absorbance form experimental sample and $A_{570\ Control}$ = Absorbance from control sample.

2.3.9 Fluorescence Imaging of CA NLS 1-NR in Cell Nuclei

Cells were seeded at a density of 12,000 in a 96-well plate (200 µl/well) and grown to confluence (24 h). After washing the cells three times with PBS, 200 µl of fresh media containing CA NLS 1-NR (6,000 NR/cell, 598 fM) were added. Cells were incubated overnight before being washed three times with PBS. 198 µl of PBS and 2 µl of Höescht dye (1 mM aqueous solution) were added to each well. Cells were incubated with Höescht dye for 10 mins before being washed three times with PBS.

Fluorescence imaging was carried out using a Lecia fluorescence microscope with appropriate filters.

2.3.10 Transmission Electron Microscopy (TEM) of Nanoparticles in Cells

Cells were grown to confluence (approximately 1.5×10^5 cells/slip) on Agar Scientific Thermanox cover slips (10.5 × 22 mm) and were incubated overnight with NQ/HQ-NS (1,500 NS/cell, 373 fM) or CA-NLS 2-NR (6,000 NS/cell, 1.50 pM) in 1 ml of CS-free media. The cells were washed three times with PBS and were fixed for 2 h in 3% (v/v) glutaraldehyde in 0.1 M sodium cacodylate buffer. The cells were then washed three times with 0.1 M sodium cacodylate buffer, followed by post fixation overnight with 1% (w/v) osmium tetroxide in 0.1 M sodium cacodylate buffer. The cells were washed with 0.1 M sodium cacodylate buffer, then dehydrated with acetone (50%-100%, in steps of 50%, 70%, 90% and 100%) and then infiltrated and embedded in epoxy resin. Ultra-thin sections of the sample were taken using a diamond knife. The sections were positioned on grids and stained with 2% aqueous uranyl acetate. The grids were then examined and photographed at an accelerating voltage of 80 keV in a CM120 Biotwin (Philips) transmission electron microscope connected to a digital camera.

2.4 Other Experimental Techniques

2.4.1 Aminosiloxane Functionalisation of Glass Microscope Slides

Slides were immersed in a 2.5 M NaOH solution (60:40 / EtOH:H_2O) for 2 h, before being rinsed thoroughly with water and dried by centrifugation. Cleaned slides were immersed in an ethanolic solution of 3-aminopropyl trimethyl siloxane (2% v/v) for 1 h, before being rinsed thoroughly with EtOH and dried by centrifugation.

2.4.2 DFT Vibrational Assignments

The optimised geometry and Raman-active vibrational modes of oxidised and reduced probe molecules were calculated using DFT at the B3LYP/LANL2DZ level of theory. All calculations were carried out using Becke's three-parameter exchange functional, coupled with the Lee-Yang-Parr correlation functional (B3LYP),[80,81] in combination with the LANL2DZ basis set of Hay and Wadt.[82,83,84] This comprises an effective core potential (ECP) plus double zeta basis for heavy atoms, with the all electron valence double zeta basis set developed by Dunning (D95V) for lighter atoms.[85] All calculations were carried out using the Gaussian 03 software package. For each molecule, unconstrained geometry optimisations were carried out, followed by frequency calculations, in order to determine the character and frequency of the Raman-active vibrational modes. The absence of imaginary frequencies was used to confirm that each calculated structure was a minimum on the molecular potential energy surface.

To investigate any effects resulting from reporter molecule proximity to the gold surface, calculations were also run on equivalent molecules with the terminal gold atoms replaced with hydrogen atoms. No significant changes in the predicted vibrational spectra were observed.

Vibrational mode assignments were based on visual inspection of the calculated modes, which were animated using the Gabedit v2.0.7. software package.

Figure 2.1 below shows a flow diagram which outlines the process involved in the DFT calculations.

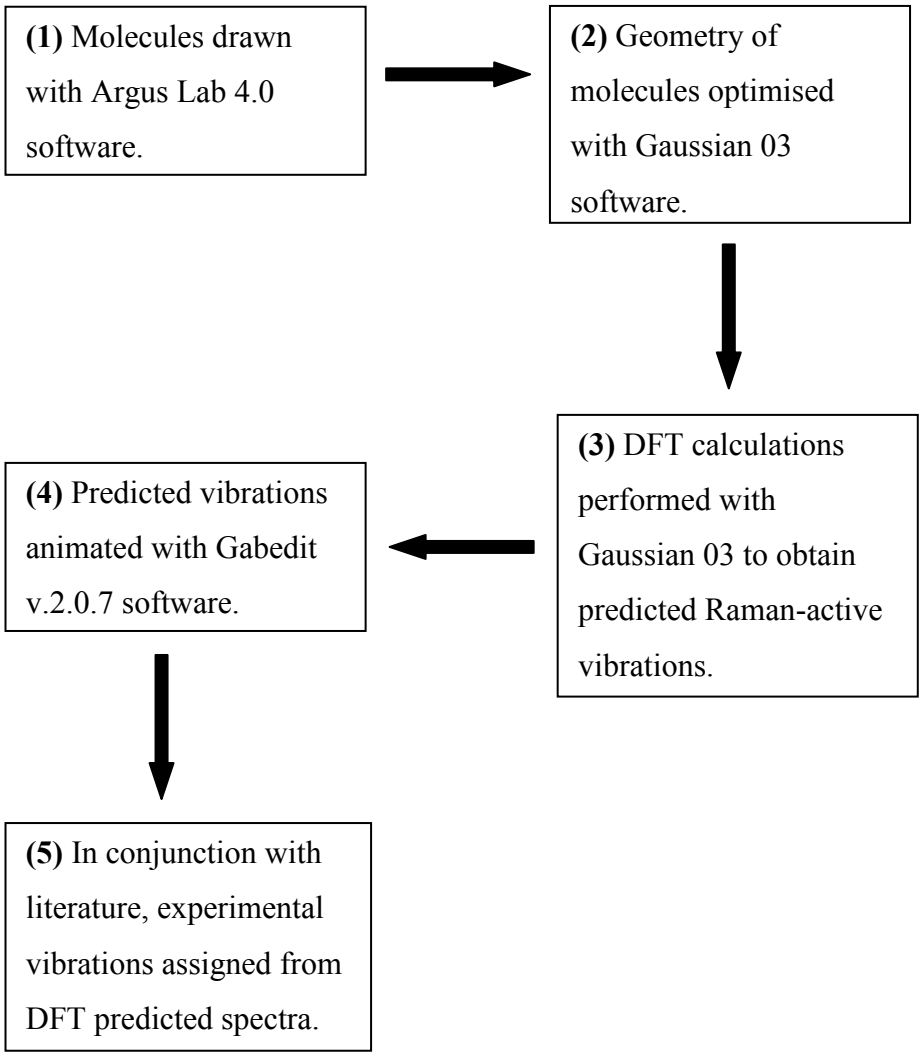

Figure 2.1: Flow chart showing the process of assigning Raman vibrations with DFT calculations. Molecules were first drawn with Argus Lab, they then had their geometry optimised and vibrational modes predicated with Gaussian 03 before the vibrations were animated with Gabedit and assigned in conjunction with the literature.

2.4.3 Cyclic Voltammetry

Cyclic voltammograms (CVs) were obtained with a Type III Autolab potentiostat using GPES v4.9 software for results analysis. A conventional three-electrode cell was used, with a coiled platinum wire (0.1 mm diameter) serving as the auxiliary electrode and a coiled silver wire (0.5 mm diameter) serving as the pseudo-reference electrode. A gold Metrohm electrode (7.07 mm^2) served as the working electrode. The CVs of the quinone and ferrocene SAMs were recorded in phosphate buffer (0.1 M, pH 7.4, 0.1 M KCl). All solutions were degassed by nitrogen bubbling for 30 mins.

2.4.4 UV-Vis Spectroscopy

Solutions containing NS, NR, probe molecule-NS and peptide molecule-NR were measured in an ATI UNICAM UV-2 UV-vis for their UV-vis spectra. The solutions were loaded in a 1 ml cuvette and the spectra recorded from 550 to 900 nm.

2.4.5 Ratio Error Calculation and Nernst Fitting

The spectral intensity ratios (a) used to determine redox potential values can be represented as a = b/c (where b and c are the intensities of the peaks used to calculate a). The errors (Δa) associated with spectral ratios were calculated using equation 2.3 by combining/propagating the individual errors (standard deviations) associated with the intensities of both peaks used to calculate the ratio.

$$\Delta a = a((\Delta b/b)^2 + (\Delta c/c)^2)^{1/2}$$

Equation 2.3: Formula used to calculate errors in spectral ratios. Where Δa = error in ratio, a = mean ratio, Δb = standard deviation of intensity in peak b, b = mean intensity of peak b, Δc = standard deviation of intensity in peak c and c = mean intensity of peak c.

The data in figures 3.10, 3.12, 3.13 and 3.15 were fitted to the Nernst equation using Origin 8.0 software and equation 2.4 below which was created in Origin 8.0 equation editor.

$$[Red] = \frac{[Q]10^{(E\Theta - E/29.5)}}{1+[Q]10^{(E\Theta - E/29.5)}}$$

Equation 2.4: Nernst fitting equation. Where [Red] = fraction of reduced species, [Q] = total quinone concentration, EΘ = standard potential and E = solution potential.

Chapter 3

Development and Characterisation of SERS-Active Redox Nanosensors

3.1 Introduction

'You must learn to walk before you can run.'

-Proverb

Before any relevant biological redox measurements were made, nanosensors that were fit for purpose had to be developed and characterised. The hypothesis that a molecule's SERS fingerprint could change quantitatively with potential also had to be investigated. In this chapter, results are presented on the design and fabrication of SERS-active redox nanosensors and their electrochemical properties. A series of spectroelectrochemical proof of concept experiments is also detailed.

As outlined in chapter 1, the prerequisite for an ideal redox monitoring system is the ability to monitor potential:

- ✓ In live cells, quantitatively and reversibly, with optimal spatiotemporal resolution.
- ✓ At a sub-cellular resolution.
- ✓ Over a wide potential range, covering hypoxia and oxidative stress.

With the above in mind, nanosensors based on SERS were conceived, constructed and assessed through novel spectroelectrochemical experiments. The SERS nanosensors in this work consist of two key components:

(1) **NS** – See section 1.4.3 (pages 26-27) for a full description of NS.

(2) **Redox-active molecules (RAMs)** – Most of the RAMs contained quinone moieties which undergo reversible $2e^-$, $2H^+$ redox reactions in buffered aqueous solutions, resulting in a change in their molecular structure.[14,86] A ferrocene-based RAM, which undergoes a reversible $1e^-$ redox process in both aqueous and organic media, was also synthesised.[14,86] All RAMs possessed thiol or disulfide functionalities to allow their irreversible chemisorption to NS.[87]

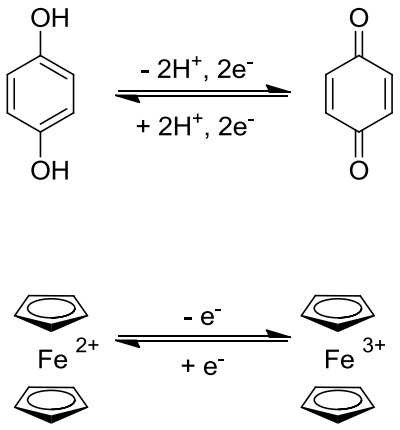

Figure 3.1: Redox reactions of: **(A)** Quinone – which undergoes reversible $2H^+$, $2e^-$ redox reactions in buffered aqueous solutions and **(B)** ferrocene – which undergoes reversible $1e^-$ reactions in buffered aqueous media .

Using standard organic chemistry, the core moieties shown in figure 3.1 can be modified to increase or decrease their reduction potentials as required. This would enable a library of compounds to be synthesised which could cover the theoretical electrochemical window of the cell from -315 mV to 820 mV as defined by NADPH and oxygen.

3.2 RAM Synthesis and Electrochemical Characterisation

3.2.1 Synthesis and Electrochemistry of AQ

Anthraquinone-2-carboxylic acid was first reacted with thionyl chloride (a powerful inorganic chlorination reagent). This converted its carboxyl group into a more reactive acyl chloride group, in order to ensure more efficient amide bond formation with cystamine in the second step. Nucleophilic attack of the acyl chloride carbonyl carbon of anthraquinone-2-carbonyl chloride (2 eq.) by cystamine's terminal amine groups yielded AQ as an off-white solid (scheme 3.1).

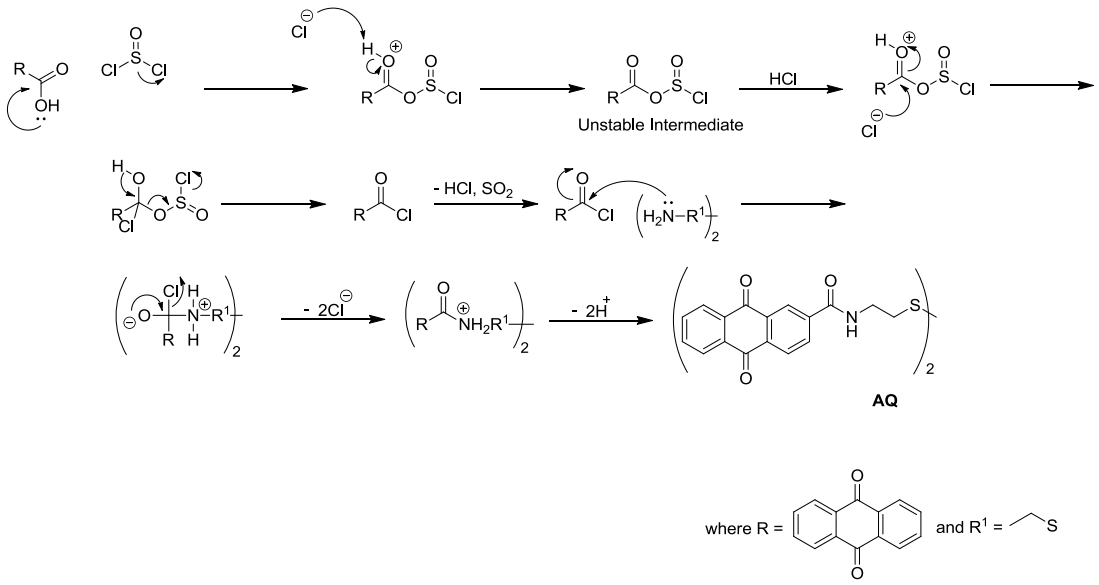

Scheme 3.1: Mechanism of AQ synthesis. Anthraquinone-2-carboxylic acid is first converted to anthraquinone-2-carbonyl chloride by thionyl chloride. Two equivalents of anthraquinone-2-carbonyl chloride are then reacted with cystamine via nucleophilic attack to yield AQ.

Electrochemical reversibility was a prerequisite for the RAMs used in this work, to enable monitoring of both oxidative and reductive changes in potential. For surface-adsorbed species in ideal conditions, electrochemical reversibility is indicated by symmetric and coincidental reduction and oxidation peaks (due to

electrode reactions being controlled only by electron transfer kinetics and not limited by diffusion).[14] Furthermore, oxidation:reduction peak height (current) and peak area (charge) ratios should equal approximately 1 and any plots of i_{Ox} vs scan rate should be linear.[14]

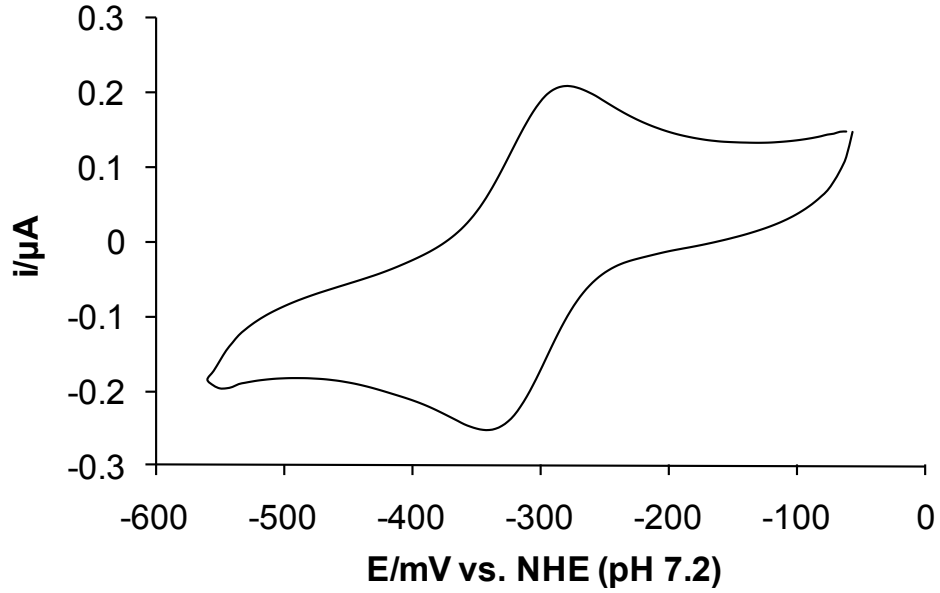

Figure 3.2: CV of an AQ SAM on a gold electrode in buffered solution (pH 7.2). Scan rate = 0.1 V/s

The CV of a SAM of AQ on a gold electrode revealed a reversible electrochemical process with a half-wave potential ($E_{1/2}$) of -312 mV (figure 3.2).

As expected, the CV of AQ's SAM did not display ideal electrochemical reversibility for a surface-adsorbed species. There was a peak separation of 59 mV between the reduction and oxidation peaks. This is because the electrode reactions involve protonation/de-protonation steps where protons are transferred to and from the buffered electrolyte solution.[14,86] These reductions and oxidations are, therefore, governed by both electron transfer kinetics *and* diffusion.[14] Indeed, this is the case for all of the quinone based RAMs. However, analysis of the AQ SAM's

oxidation:reduction peak height and peak area ratios both approximate to 1 and a plot of i_{Ox} vs. scan rate was linear (see appendix 1 for data). These traits indicated electrochemical reversibility.

3.2.2 Synthesis and Electrochemistry of NQ

NQ was formed in a substitution reaction. Cystamine's nucleophilic terminal amine groups attacked the 2-position of 2,3-dichloro-1,4-naphthoquinone to give NQ as a deep red solid (scheme 3.2).

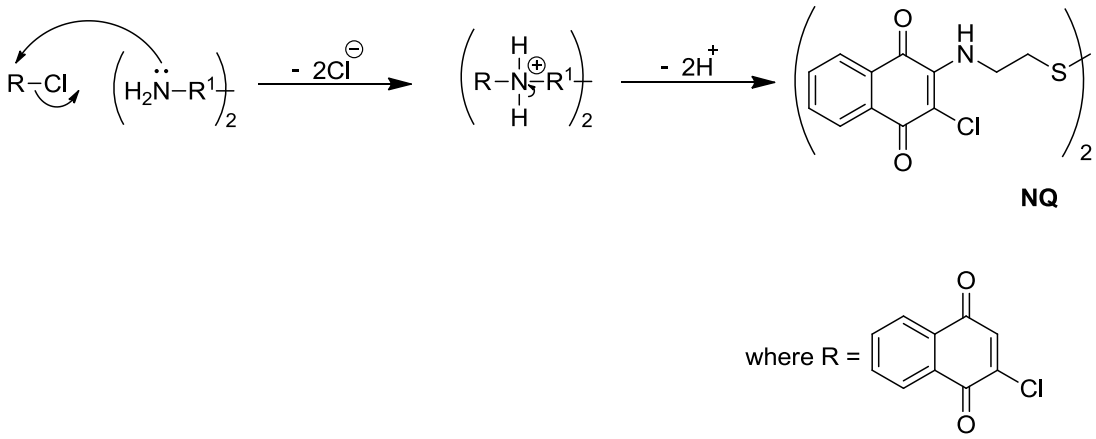

Scheme 3.2: Mechanism of NQ synthesis. The terminal amine groups of cystamine attack the 2-position of 2,3-dichloro-1,4-naphthoquinone to yield NQ.

The CV of a NQ SAM on a gold electrode revealed a reversible electrochemical process with an $E_{1/2}$ of -283 mV (figure 3.3). Due to there being less electron density within NQ, it was expected that its $E_{1/2}$ would be higher than AQ (i.e. NQ would be easier to reduce than AQ).

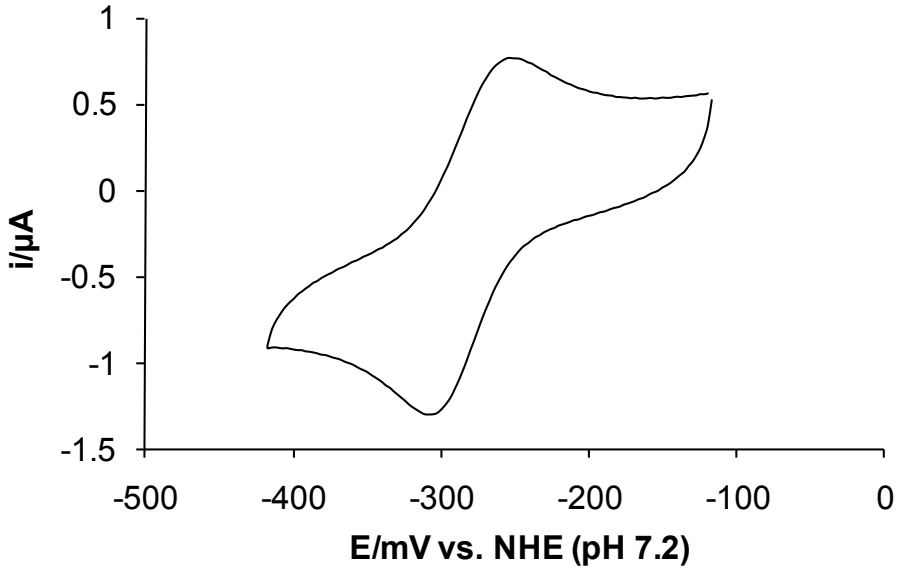

Figure 3.3: CV of a NQ SAM on a gold electrode in buffered solution (pH 7.2). Scan rate = 0.1 V/s.

As with the AQ SAM, ideal electrochemical reversibility was not observed. There was also separation between the reduction and oxidation peaks (60 mV in this case). However, this was again to be expected and further analysis revealed oxidation:reduction peak height and peak area ratios both approximate to 1 and a plot of i_{Ox} vs. scan rate was linear (see appendix 1 for data).

3.2.3 Synthesis and electrochemistry of HQ

The two-step synthesis of HQ firstly involved a Michael-type reaction of sodium thiosulfate with 1,4-benzoquinone. In the second step, the resulting 2-thiosulfate-1,4-benzoquinone was then reduced with Zn and HCl to produce HQ as a white solid (scheme 3.3).

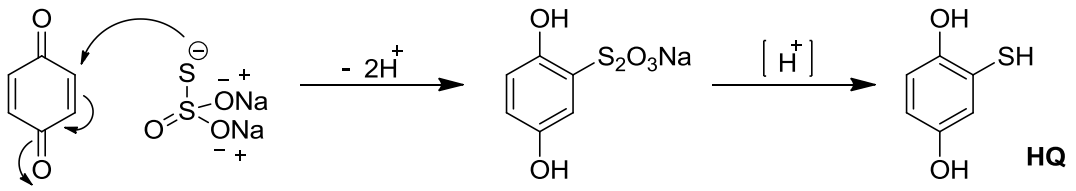

Scheme 3.3: Mechanism of HQ synthesis.

The CV of a SAM of HQ on a gold electrode revealed a reversible electrochemical process with an $E_{1/2}$ of 130 mV (figure 3.4). There is considerably less electron density within HQ than either AQ or NQ and, as such, a higher $E_{1/2}$ than NQ was observed.

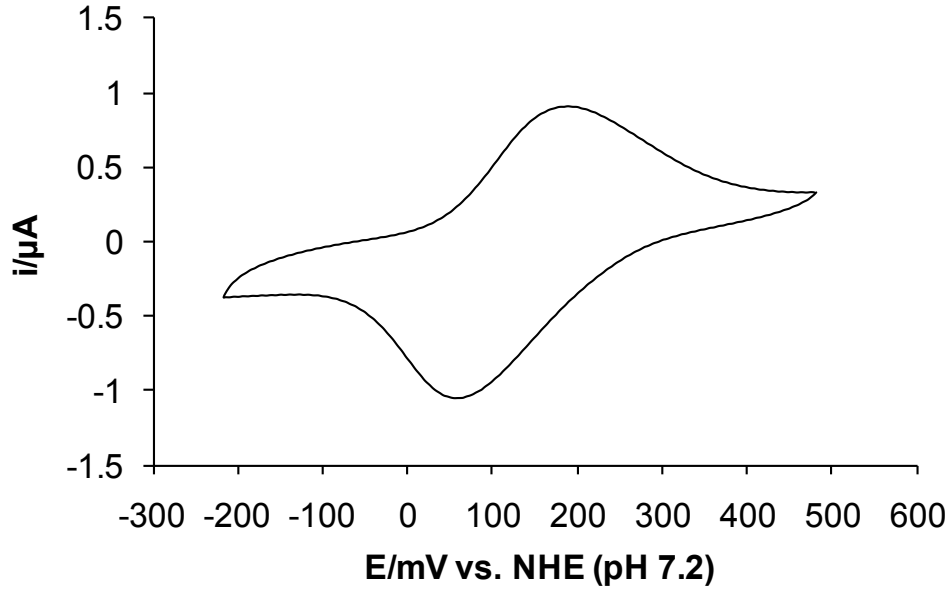

Figure 3.4: CV of a HQ SAM on a gold electrode in buffered solution (pH 7.2). The scan rate is 0.1 V/s.

Once again, there was a separation between the reduction and oxidation peaks (102 mV in this case). However, inspection of the oxidation:reduction peak height and peak area ratios revealed that both were approximate to 1 and the plot of i_{Ox} vs. scan rate for HQ was linear (see appendix 1 for data).

3.2.4 Synthesis of FCBX

In a similar fashion to AQ, FCBX was formed *via* an amide bond linkage (in this instance, between fluorocarbonylferrocene and cystamine). Ferrocene carboxylic acid was first converted into fluorocarbonylferrocene using cyanuric fluoride as a mild fluorinating reagent. As is the case with the reaction of acyl chlorides and amines, conversion of carboxyl groups to more reactive acyl fluorides ensures more efficient amide formation in their reaction with amines.[88] Fluorocarbonylferrocene was used instead of chlorocarbonylferrocene, due to the relatively low yields and instability of the latter.[75] Through nucleophilic attack by cystamine's terminal amines on the carbonyl carbon of fluorocarbonylferrocene, FCBX was formed as bright orange crystals (scheme 3.4).

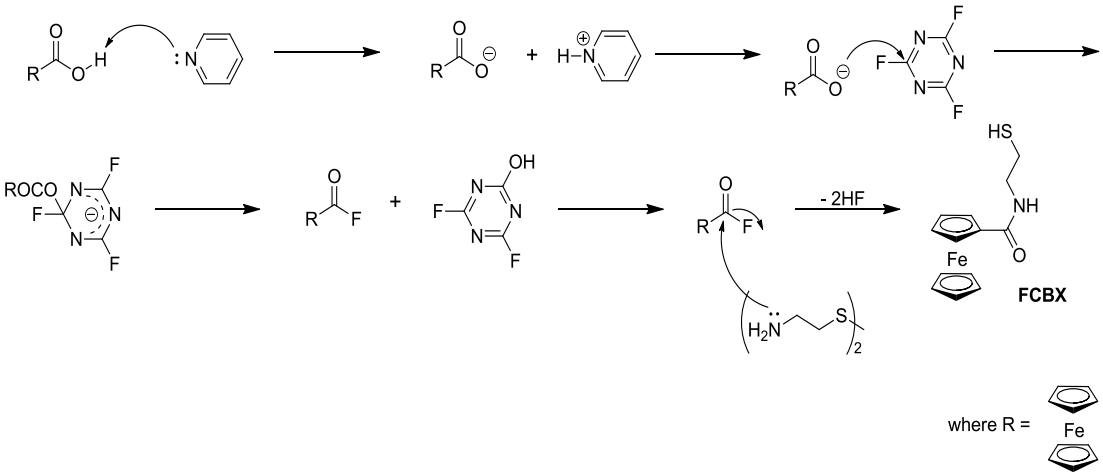

Scheme 3.4: Mechanism of FCBX synthesis.

The CV of a SAM of FCBX on a gold electrode revealed a reversible electrochemical process with an $E_{1/2}$ of 459 mV (figure 3.5).

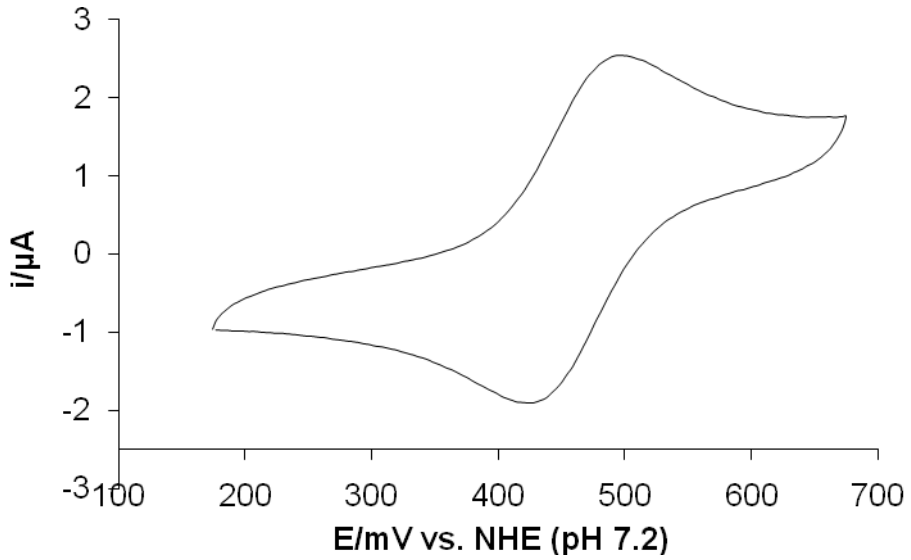

Figure 3.5: CV of a FCBX SAM on a gold electrode in buffered solution (pH 7.2). The scan rate is 0.1 V/s.

Electrochemical reversibility was indicated by the oxidation:reduction peak height and peak area ratios being approximate to 1 and the plot of i_{Ox} vs. scan rate for FCBX being linear (see appendix 1 for data). However, deviation from reversible electrochemical behaviour was observed through a peak separation of 62 mV. This was not entirely unexpected, as there is still a diffusion process involving the Cl^- counter-ions when the Fe^{2+} to Fe^{3+} oxidation occurs.

3.2.5 Theoretical Range of SERS-Active Redox Nanosensors

By taking the $E_{1/2}$ values for each probe molecule (as determined by CV) and varying the ratio of reduced:oxidised species it was possible to generate theoretical plots of the potential range in which they could monitor according to the Nernst equation (page 2). For each quinone probe molecule n was set to equal two and it was assumed that quinones were reduced in a $2H^+$, $2e^-$ redox reaction without intermediary formation of semi-quinone. For the FCBX probe molecule, n was set to equal one. Figure 3.6 below shows the theoretical potential ranges that it would be possible to monitor with the array of probe molecules described in this chapter.

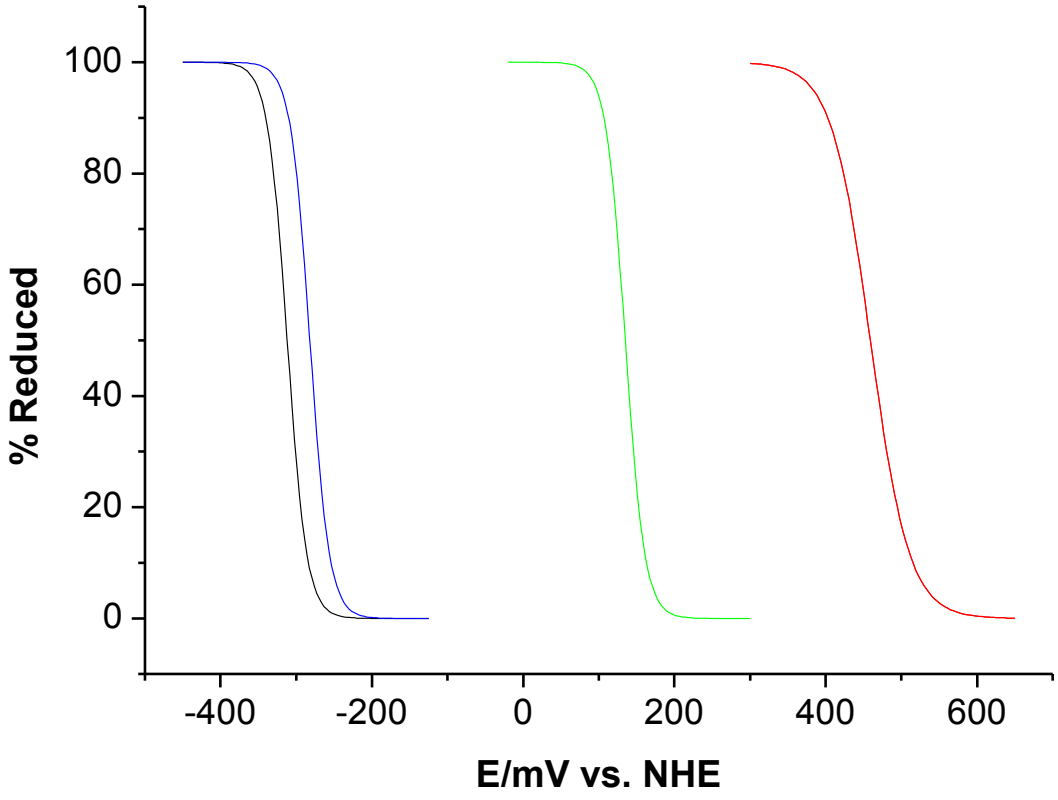

Figure 3.6: Theoretical potential window of nanosensor library as determined by the Nernst equation. Potential range of: AQ (black line); NQ (blue line); HQ (green line); and FCBX (red line).

While NQ, which as an $E_{1/2}$ similar to that of GSH, would be useful for monitoring subtle changes in IRP, the Nernstian plots reveal that AQ, with its lower, more negative $E_{1/2}$, would be useful for monitoring hypoxic potentials. On the other hand HQ and FCBX have far greater $E_{1/2}$ values than NQ and, therefore, would be potentially suited to monitoring events and processes associated with oxidative stress events. With sensitivities of the probe molecules decreasing as they are near to being fully oxidised or reduced, there is a need to 'plug the gaps' in figure 3.6 in order to be able to accurately monitor the full theoretical potential window of the cell.

3.3 SERS Spectroelectrochemistry

In order to quantify oxidation state dependent changes in the vibrational modes of the RAMs, SERS spectroelectrochemistry was employed. Two spectroelectrochemical methods were developed during this work:

(1) **Electrode Spectroelectrochemistry** – In these experiments, nanosenors were immobilised on the surface of microfabricated gold electrodes. Using a potentiostat, the potential was varied and SERS spectra were recorded from the surface to determine if it would be possible to link potential changes quantifiably with changes in the SERS fingerprints of RAMs.

To anchor nanosensors to the gold electrodes, a poly-L-lysine coating was deposited across their surface. In order to achieve this, a layer of mercaptopropionic acid was first chemisorbed onto the gold electrodes through Au-S bonds. The carboxyl groups of the acid were then activated with EDC, before forming amide bonds with poly-L-lysine. Creating a poly-L-lysine coating had the effect of fashioning the electrode surface with free amine groups. This allowed NS to bind to the electrode surface through electrostatic interactions.[89] After surface attachment of NS, a SAM of RAMs was then formed and SERS spectra were recorded at varying potentials.

Figure 3.7 below depicts how SERS spectroelectochemistry from electrodes was facilitated.

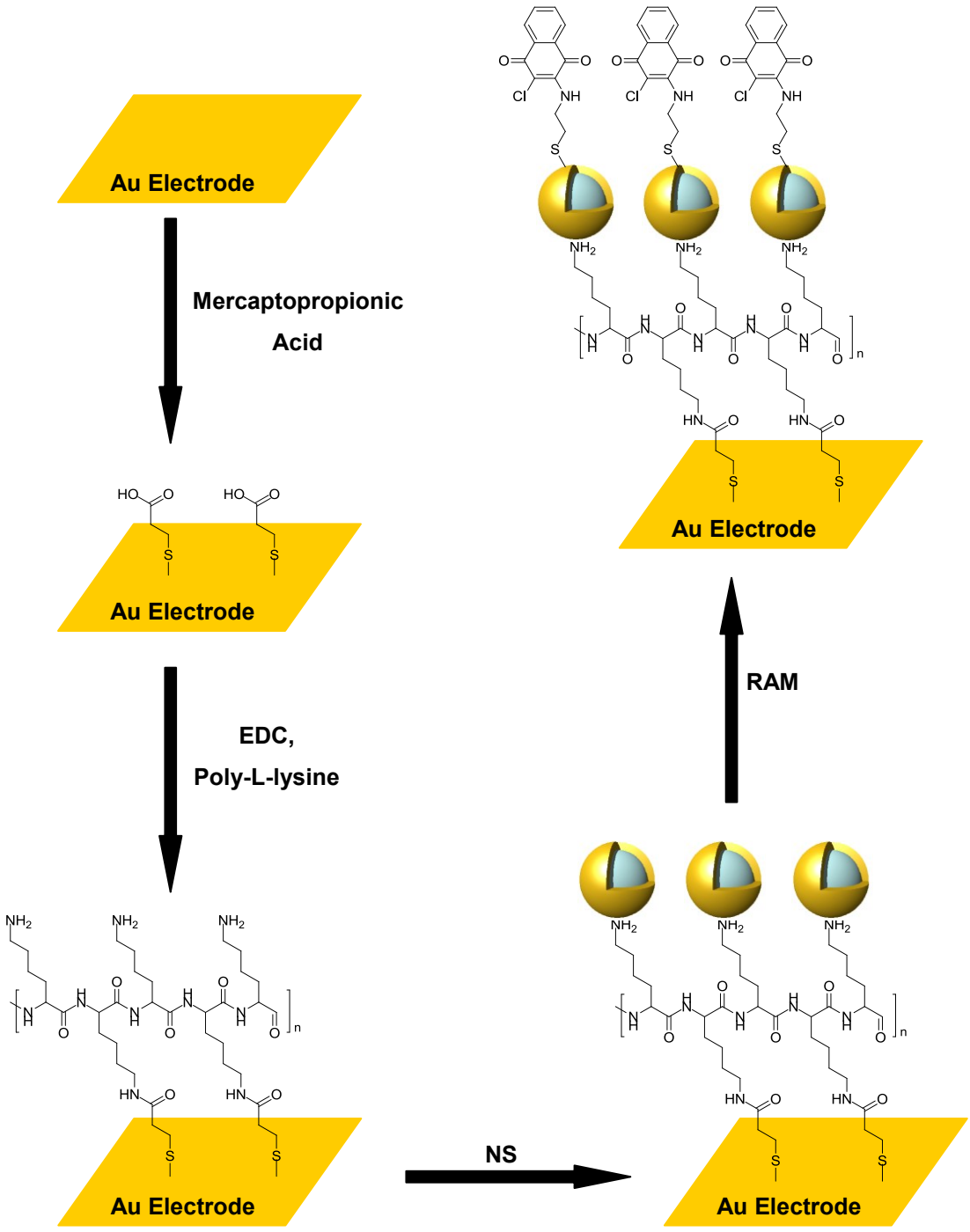

Figure 3.7: Assembly of nanosensors for spectroelectrochemistry. Gold electrodes were first functionalised with mercaptopropionic acid before being coupled to poly-L-lysine with EDC. NS were then deposited on the surface of the electrodes and functionalised with RAMs.

In order to ascertain whether nanosensors had been successfully immobilised, 3-D atomic force microscopy (AFM) images were recorded in tapping mode over the surface of the gold electrodes. AFM works by measuring the forces between the surface of a chosen sample and a probe tip attached to the end of a vertically oscillating cantilever.[90] In tapping mode, the probe tip lightly contacts the analyte surface on the bottom of its swing ensuring minimal sample damage.[90] As the probe tip moves over the sample, laser light is reflected from the top of the cantilever onto a photodiode.[90] Signals are then processed electronically and topographic images of surfaces are generated.[90]

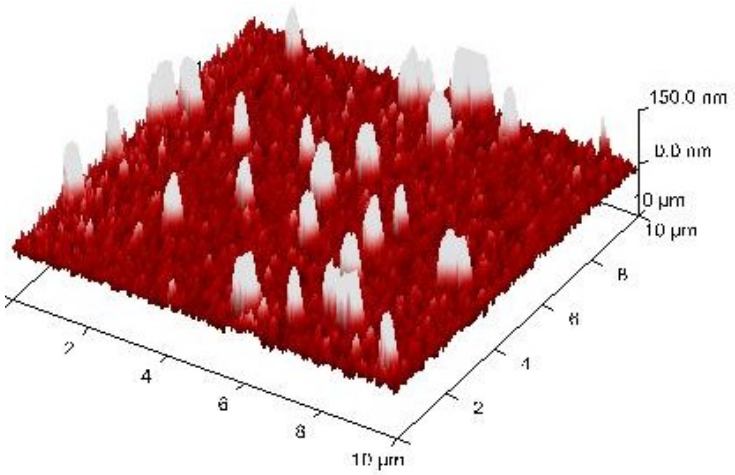

Figure 3.8: 3-D AFM image of nanosensors on the surface of a microfabricated electrode.

Figure 3.8 shows a 3-D topographic image of nanosensors (raised white columns) immobilised on the surface of a gold electrode (red background). The raised white areas are ~150 nm in height and clearly confirm the success of nanosensor (also ~150 nm) immobilisation on gold electrodes.

(2) **Redox Couple Spectroelectrochemistry** – In these experiments, the RP of aqueous solutions (containing nanosensors) was varied according to the Nernst equation - that is, by varying the ratio of [oxidised]:[reduced] species of soluble cellular redox couples. SERS spectra were then recorded from the nanosensors in

solution and any quantifiable changes in RAM fingerprint were correlated with potential.

This method was developed as an alternative to electrode spectroelectrochemistry. Like electrode spectroelectrochemistry, spectroelectrochemistry with soluble cellular redox couples is also a useful technique for investigating whether or not a particular probe molecule's SERS fingerprint is sensitive to oxidation state changes. In fact, solution spectroelectrochemistry is a more representative model of the cellular interior in which the nanosensors would be expected to operate.

3.3.1 Electrode Spectroelectrochemistry of HQ-NS

Figure 3.9 shows the structure of HQ along with its $E_{1/2}$ value and redox reaction scheme. It also shows SERS spectra of HQ-NS, immobilised on gold microfabricated electrodes, recorded at potentials from -12 to 370 mV vs. NHE (pH 7.2).

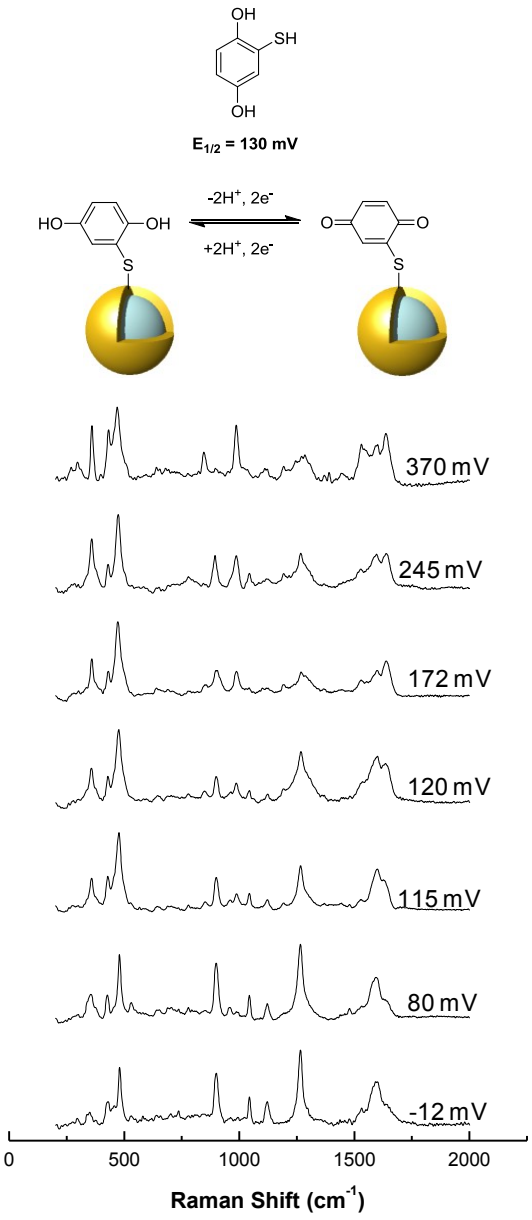

Figure 3.9: Spectroelectrochemistry of HQ-NS. SERS spectra of HQ-NS immobilised on gold electrodes were recorded at potentials ranging from -12 to 370 mV.

Using DFT at the B3LYP/6-31g(d,p) level, in accordance with the literature,[61] individual vibrational modes of oxidised and reduced HQ-NS were assigned (Tables 3.1 and 3.2). Predicted spectra showed excellent correlation with the observed spectra. DFT calculations to predict spectra were undertaken in collaboration with P. Richardson (University of Edinburgh).

Wavenumber (cm^{-1})	Assignment
356	Carbon framework angle bending
428	C-H angle bending
477	C=C angle bending
841	C-C stretching
983	Out-of-plane C-H wagging w/ C-C stretching
1263	Symmetric ring breathing
1525	C=C stretching
1602	Asymmetric ring breathing
1633	C=C stretching w/ C=O stretching

Table 3.1: Vibrational assignments of oxidised HQ.

Wavenumber (cm^{-1})	Assignment
428	C-H angle bending
477	C=C angle bending
895	Out-of-plane C-H wagging w/ carbon framework angle bending
1041	C-H angle bending w/ Ar ring stretching
1117	C-H stretching w/ O-H stretching
1263	Symmetric ring breathing
1585	Asymmetric ring breathing

Table 3.2: Vibrational assignments of reduced HQ.

Several features showed a marked potential dependent, change in intensity and frequency. Among these, the peak at 358 cm^{-1} which corresponds to carbon framework angle bending; the peak at 1263 cm^{-1} which corresponds to symmetric ring breathing; and the peak at 1585 cm^{-1} which splits from a singlet to a triplet corresponds to the asymmetric ring breathing, C=C stretching and C=O stretching vibrational modes. When the normalised intensity of the peak at 358 cm^{-1} was plotted against potential, the midpoint potential (at which equal amounts of reduced and

oxidised species are present) correlated well with the half-wave potential, further confirming that the SERS measurement reported accurately on the oxidation state of the molecule (figure 3.10).

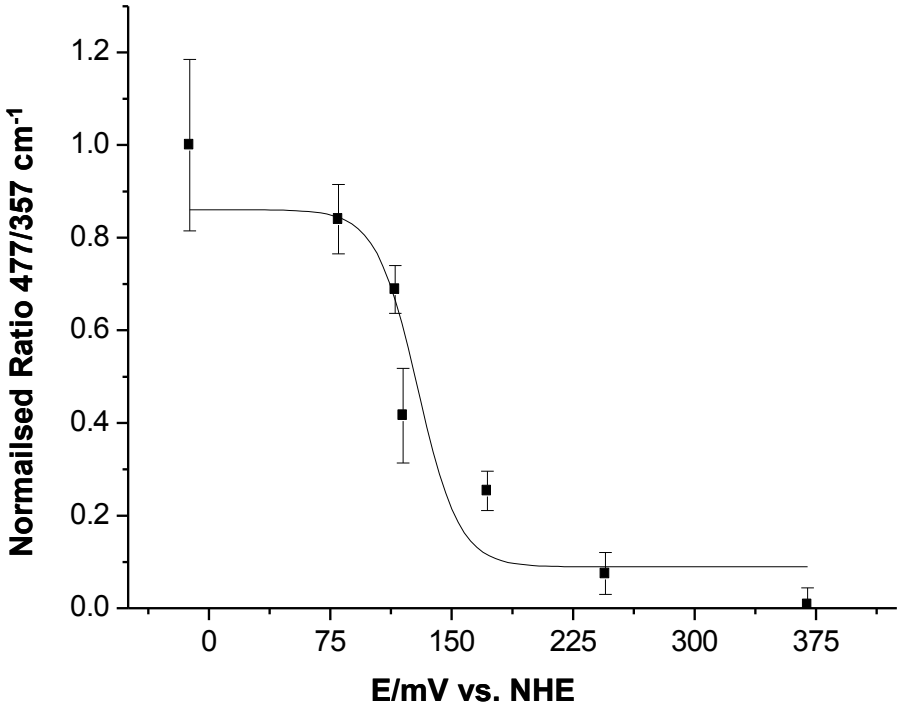

Figure 3.10: RP range covered by HQ-NS. Error bars show the standard deviation of three measurements. Points indicate SERS spectroscopic measurements. Solid lines (fitted using Origin 8.0) represent plots of the Nernst equation on the basis of $E_{1/2}$ measured by CV.

For a full description of the ratio error calculations along with the Nernst fitting procedure refer to chapter 2 pages 50-51.

3.3.2 Electrode and Redox Couple Spectroelectrochemistry of NQ-NS

Figure 3.11 shows the structure of NQ along with its $E_{1/2}$ value and redox reaction scheme. It also shows SERS spectra of NQ-NS at potentials ranging from -394 to -194 mV vs. NHE (pH 7.2), recorded using electrode spectroelectrochemistry.

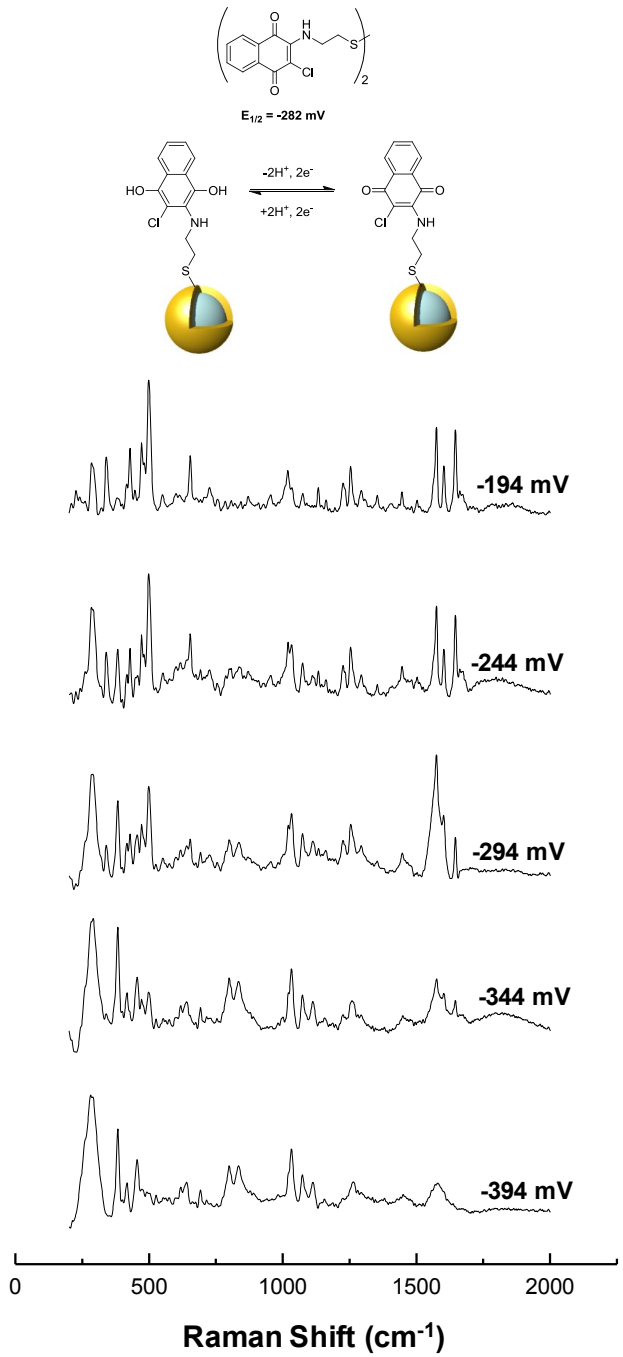

Figure 3.11: Spectroelectrochemistry of NQ-NS. SERS spectra of NQ-NS immobilised on gold electrodes were recorded at potentials ranging from -394 to -194 mV.

Similar to HQ-NS, experimental and predicted spectra for NQ-NS correlated well. Vibrational assignments are shown below in Tables 3.3 and 3.4.

Wavenumber (cm^{-1})	Assignment
280	Out-of-plane C-Cl wagging
339	S-Au stretching
417	Out-of-plane C=O wag w/ aliphatic C-C angle bending
440	Carbon framework angle bending
475	Carbon framework angle bending
654	C-S stretch
1018	Ar ring stretching
1072	Aliphatic C-C stretching
1110	Aliphatic C-H wagging w/ C-C ring stretching
1225	Out-of-plane Ar C-H wagging w/ Aliphatic C-H
1253	In-plane Ar C-H wagging w/ aliphatic C-H wagging
1577	Symmetric ring breathing
1602	Ar ring stretching w/ N-H wagging
1645	C=O stretching w/ Ar ring stretching

Table 3.3: Vibrational assignments of oxidised NQ.

Wavenumber (cm^{-1})	Assignment
280	In-plane C-Cl wagging
380	Out-of-plane O-H wagging
415	Carbon framework angle bending
455	Carbon framework angle bending
691	C-S stretch w/ carbon framework angle bending
798	Aliphatic C-H wagging
833	Ar C-H angle bending w/ O-H angle bending
1030	Aliphatic C-H wagging w/ Ar ring stretching
1071	Aliphatic C-C stretching
1111	Aliphatic C-H wagging w/ Ar ring stretching
1261	In-plane Ar C-H wagging
1577	Symmetric ring breathing

Table 3.4: Vibrational assignments of reduced NQ.

As expected, several distinct potential dependent spectral changes were noted at potentials more reducing than those of HQ-NS. Vibrational modes which changed as a result of oxidation state included the in-plane C-Cl wagging at 280 cm^{-1}, the doublet at 798-833 cm^{-1}, which corresponded to aliphatic C-H wagging and aromatic C-H angle bending and the peak at 1576 cm^{-1}, which splits from a singlet to a triplet corresponding to symmetric ring breathing, aromatic ring stretching and C=O stretching. When the normalised intensity of the peak at 1645 cm^{-1} was plotted against potential, the mid-point potential correlated well with the half-wave potential (figure 3.12). Again, this confirmed that SERS spectra report on the oxidation state of the compound.

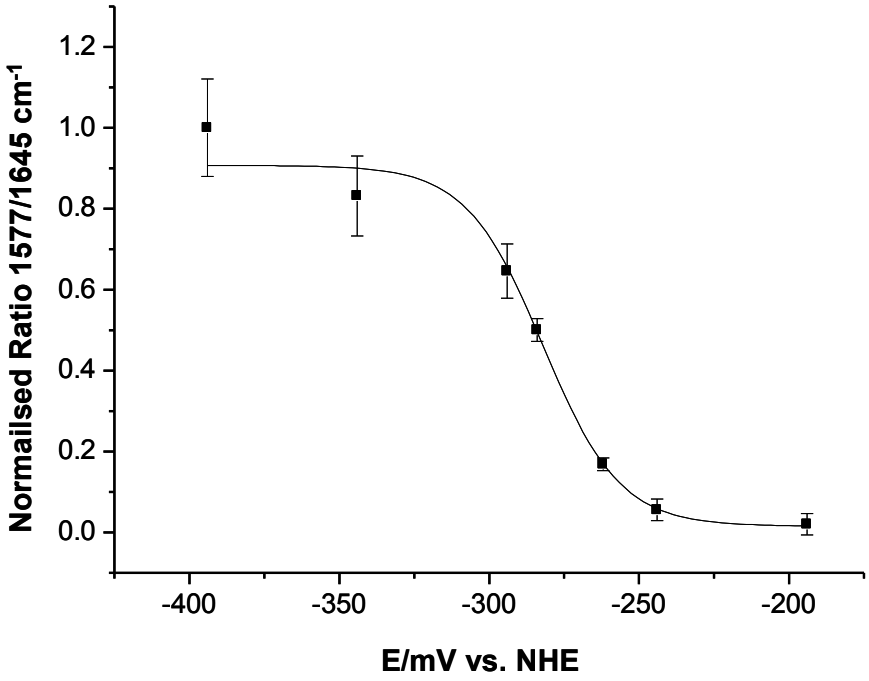

Figure 3.12: RP range covered by NQ-NS. Error bars show the standard deviation of three measurements. Points indicate SERS spectroscopic measurements. Solid lines represent plots of the Nernst equation on the basis of $E_{1/2}$ measured by CV.

In addition to electrode spectroelectrochemistry, quantifiable potential changes were observed from NQ-NS SERS spectra recorded in phosphate buffer solutions containing varying ratios of several soluble redox couples. The three redox couples

used in this work were: GSH/GSSG, cysteine/cysteine disulfide (CyS/CySSyC) and $NADPH/NADP^+$.

The Nernst equation for the GSH/GSSG and CyS/CySSyC redox couples can be represented as follows:

$$E = -252 - 30 \log ([GSH]^2/[GSSG]) \text{ mV}$$

at pH 7.2 and 25 °C.

Equation 3.1: Nernst equation for the RP of the GSSG/2GSH half-cell.

$$E = -240 - 30 \log ([CyS]^2/[CySSyC]) \text{ mV}$$

at pH 7.2 and 25 °C.

Equation 3.2: Nernst equation for the RP of the CySSyC/2CyS half-cell.

For the $NADPH/NADP^+$ redox couple, the Nernst equation can be represented as:

$$E = -327 - 30 \log ([NADPH] /[NADP^+]) \text{ mV}$$

at pH 7.2 and 25 °C.

Equation 3.3: Nernst equation for the RP of the $NADPH/NADP^+$ half-cell.

In each case, these cellular redox couples performed electron transfer to or from NQ-NS (figure 3.13). In the case of $NADPH/NADP^+$, however, only the 10% fully-oxidised $NADP^+$ was a strong enough oxidising agent to oxidise NQ-NS. This suggests that NQ-NS measures a cellular redox state which takes into account more than one redox couple.

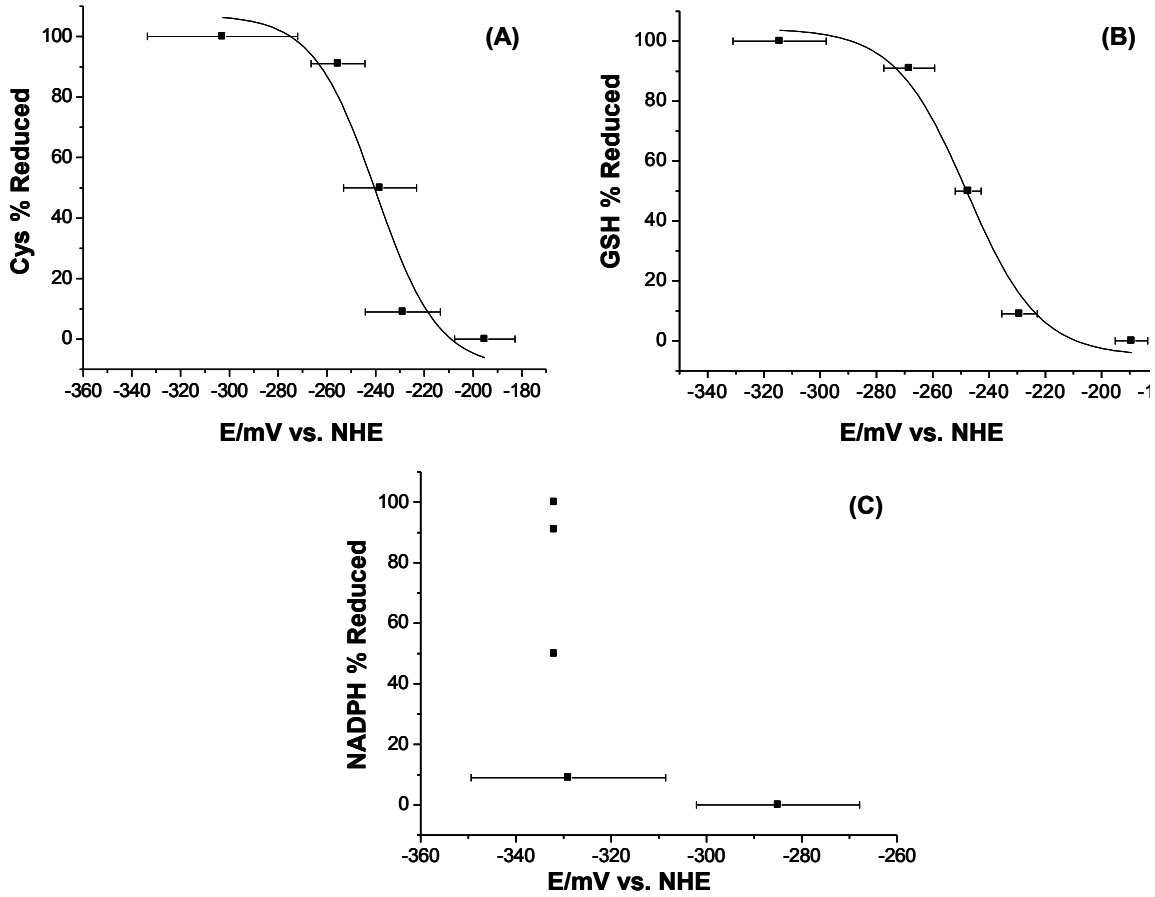

Figure 3.13: RPs, measured using NQ-NS, in the presence of varying ratios of cellular redox couples. **(A)** CyS/CySSyC; **(B)** GSH/GSSG; **(C)** $NADPH/NADP^+$. In the case of $NADPH/NADP^+$, only the 0% and 10% reduced samples are sufficiently oxidising to give a measurable sensor response. Error bars represent standard deviations of three measurements.

3.3.3 Redox Couple Spectroelectrochemistry of AQ-NS

AQ-NS has an $E_{1/2}$ value similar to that of the important cellular redox couple $NADPH/NADP^+$ ($E_{1/2}$ = -327 mV). AQ-NS SERS spectra would, therefore, be expected to vary in a Nernstian fashion in phosphate buffer solutions containing varying concentrations of the oxidised and reduced forms of this particular redox couple.

Figure 3.14 shows the structure of AQ along with its $E_{1/2}$ value and redox reaction scheme. It also shows SERS spectra of AQ-NS at potentials ranging from -417 to -271 mV vs. NHE (pH 7.2) recorded in phosphate buffer solutions containing varying concentrations of NADPH and $NADP^+$.

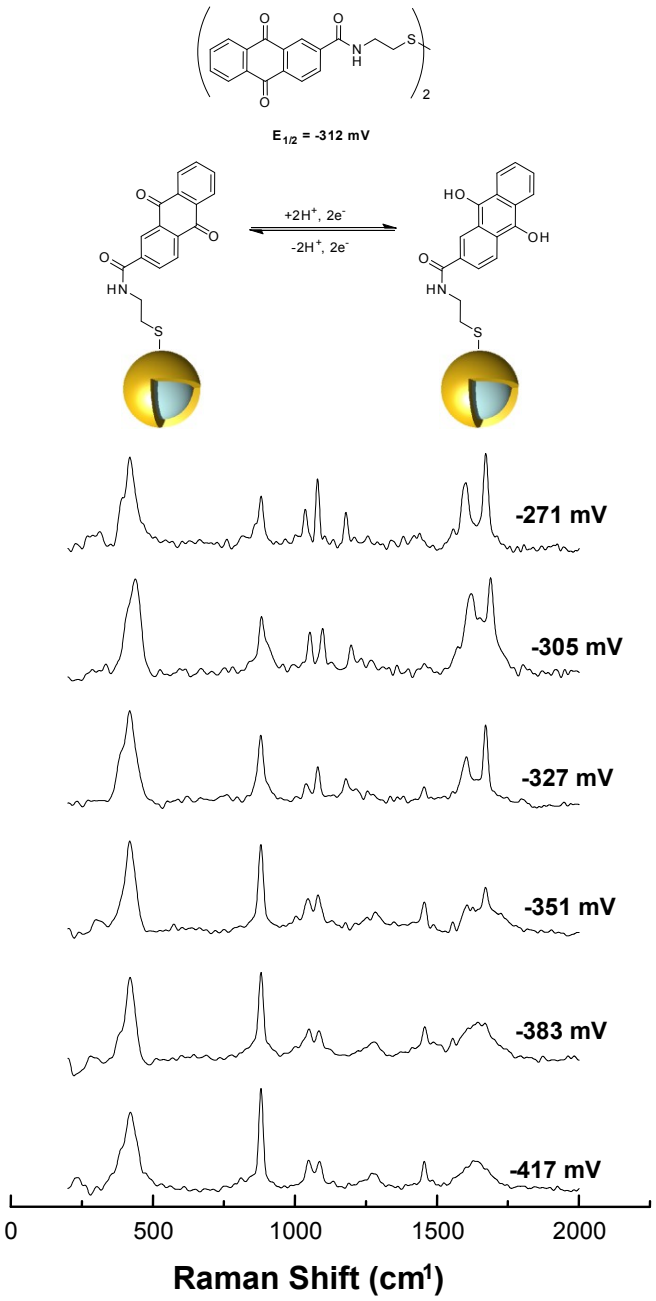

Figure 3.14: Spectroelectrochemistry of AQ-NS. SERS spectra of AQ-NS immobilised on gold electrodes were recorded at potentials ranging from -417 to -271 mV.

As expected, several distinct potential-dependent spectral changes were noted at potentials more reducing than those of NQ-NS. Vibrational modes, which notably changed as a result of oxidation state, included the out-of-plane aromatic C-H wagging at 876 cm^{-1}, the aromatic C-C stetching at 1453 cm^{-1}, the peak at 1606 cm^{-1}, which splits from a singlet to a doublet corresponding to amide stretching w/ symmetric ring breathing, and quinone C=O stretching. When the normalised intensity of the peak at 876 cm^{-1} was plotted against potential, the midpoint potential correlated well with the half-wave potential (figure 3.15).

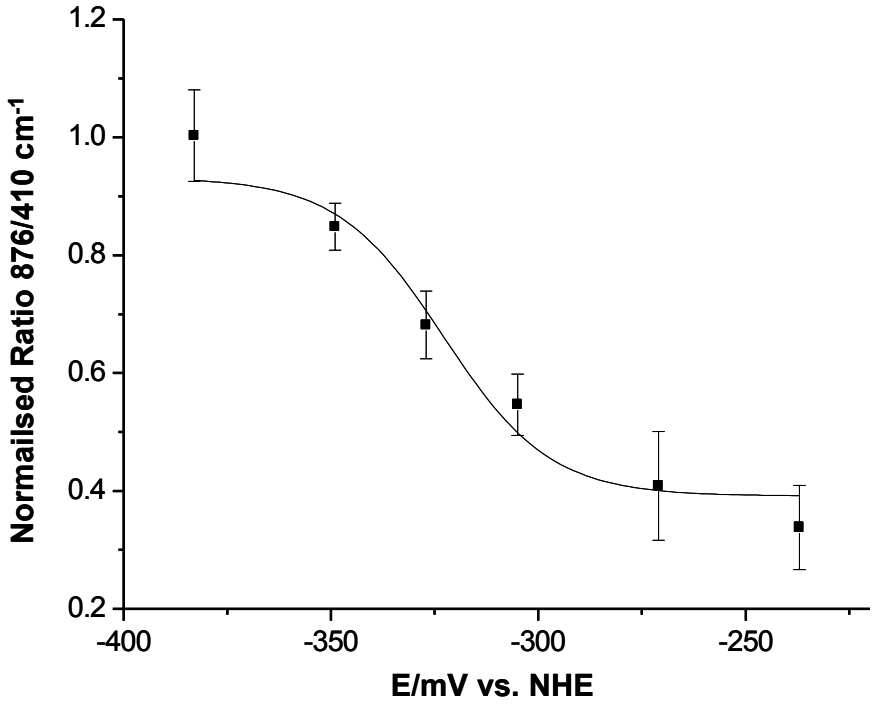

Figure 3.15: RP range covered by AQ-NS. Error bars show the standard deviation of three measurements. Points indicate SERS spectroscopic measurements. Solid lines represent plots of the Nernst equation on the basis of $E_{1/2}$ measured by CV.

Similar to NQ-NS and HQ-NS, experimental and predicted spectra for AQ-NS correlated well (Tables 3.5 and 3.6).

Wavenumber (cm^{-1})	Assignment
410	Out-of-plane amide N-H wagging w/ carbon framework angle bending
861	Out-of-plane aromatic C-H wagging
1030	Aromatic C-C stretching
1077	Aliphatic C-C stretching
1175	Aliphatic C-H stretching
1595	Amide stretching w/ symmetric ring breathing
1668	Quinone C=O stretching

Table 3.5: Vibrational assignments of oxidised AQ.

Wavenumber (cm^{-1})	Assignment
413	Out-of-plane N-H wagging w/ carbon framework angle bending
878	Out-of-plane aromatic C-H wagging
1046	Aromatic C-C stretching
1079	Aliphatic C-C stretching
1256	In-plane Ar C-H wagging w/ aliphatic C-H wagging
1450	Aromatic C-C stretching
1606	Amide stretching w/ symmetric ring breathing

Table 3.6: Vibrational assignments of reduced AQ.

3.3.4 Spectroelectrochemistry of FCBX

Figure 3.16 shows the structure of FCBX along with its $E_{1/2}$ value and redox reaction scheme. It also shows SERS spectra of FCBX-NS at potentials of 244 and 619 mV vs. NHE (pH 7.2).

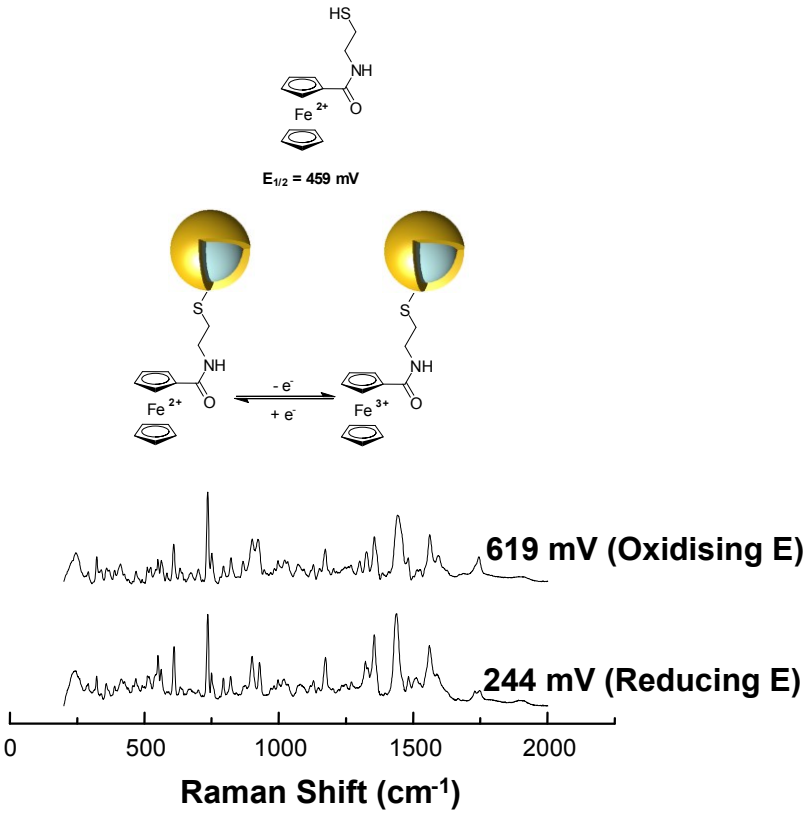

Figure 3.16: Spectroelectrochemistry of FCBX-NS at a reducing potential of 244 mV and an oxidising potential of 619 mV.

Unlike HQ-NS or NQ-NS, no potential-dependent changes were observed in the SERS spectra of FCBX-NS. DFT calculations also showed no significant changes in the spectra of FCBX-NS with oxidation state. One possible explanation is that, whereas with the quinone RAMs there is a change in molecular structure (most notably the oxidation of hydroxyl or carbonyl groups and changes in the aromaticity of the rings),[14,86] the redox reaction of FCBX is occurring at the iron centre and, whilst there is a change in the electronic structure, there appears to be no change in

vibrational modes of the ring structures. For this reason, FCBX was discounted for further experiments.

Wavenumber (cm^{-1})	Assignment
249	Framework deformations
736	Aliphatic C-C stretching
923	Cp C-C stretching
1324	Cp-amide rocking
1354	Cp C-C stretching
1440	In-plane C-H wagging
1560	In-plane N-H wagging
1741	C=O stretching

Table 3.7: Vibrational assignments for FCBX.

3.4 Conclusions

A series of redox nanosensors with SERS fingerprints, that are sensitive to oxidation state changes, has been developed.

It has been shown that, by using simple synthetic organic chemistry, the potential window in which a given probe operates can be selectively tuned. Further synthetic work would enable assembly of a larger array of SERS nanosensors, with which IRP could be studied across the theoretical electrochemical window of a cell.

It has also been shown, through two spectroelectrochemical methods, that changes in SERS traces of RAMs are quantifiable and can be correlated with RP. These changes are both rapid and reversible, which offers an opportunity to monitor both reductive and oxidative changes in real time.

To summarise, these nanosensors are exciting new analytical tools that offer users the opportunity to explore and monitor IRP and its modulation over a previously unattainable range. While FCBX does not show promise as a RAM, this is less of a concern for the study of eukaryotic systems, where the cell rarely explores the extremely oxidative range of the theoretical potential window.[6]

Chapter 4

Cellular Delivery and Nanosensor Toxicity Studies

4.1 Introduction

Before any attempts were made to measure and monitor IRPs, two important questions had to be answered:

- Would it be possible for nanosensors to be controllably delivered into cells?
- Would their introduction cause any cytotoxic side effects?

Previously, through TEM studies, the Campbell group had demonstrated the uptake of bare NS by NIH/3T3 mouse fibroblast cells in CS-free DMEM growth media.[71] While the exact mechanism of NS uptake is still under investigation, it has been shown to be independent of energy, clathrin and cholesterol.[71] With these CS-free culture conditions, NS were shown to reside predominantly in the cytoplasm after uptake and were not encapsulated in vesicles; nor were they coated in lipids.[71] The NS used in this work were functionalised with monolayers of RAMs and, as such, possessed unique surface properties which may have affected their uptake by cells. It was, therefore, important to study their intracellular fate in a similar fashion to the previous work of Ochsenkuhn *et al*.[71]

Today, the presence of nanoparticles in everyday life is widespread. They are used in a range of applications including: electronics, clothing, cosmetics and medicine.[91]

Figure 4.1: Examples of products and technologies containing nanoparticles. Top left – electronic circuit board where nanomaterials are now being used. Top right – sunscreen where ZnO nanoparticles have been used to block out harmful UV light. Bottom left – Gold nanoparticles delivering drugs. Bottom right – nanosilver socks. [92,93,94,95]

Despite their rapidly increasing popularity, some nanomaterials have been shown to cause harmful effects. Indeed, fullerenes, carbon nanotubes and metal oxide nanoparticles (such as TiO_2) have been shown to cause an increase in ROS levels which can, of course, lead to oxidative stress, excessive inflammation, or biomolecule damage.[96,97,98] Exposure to these materials has even been implicated in mesothelioma, a cancer that develops from the protective lining of internal organs.[98]

One of the accepted mechanisms of nanoparticle cytotoxicity is frustrated phagocytosis,[98,99] which leads to overproduction of ROS by activated NADPH oxidases in phagosomes.[99,100] This has been shown to be important in such conditions as asbestosis.[98] Nanoparticles can also cause toxicity by leaching of transition metals,[101] or by catalytic reduction of oxygen to $O_2^{\cdot -}$ through intracellular Fenton reactions.[102]

However, gold nanoparticles are used extensively in biology and medicine.[103] It would, therefore, be reasonable to expect the NS used in this work to have different toxicological characteristics from the nanomaterials described above. Since the ultimate goal of this work is to monitor IRP changes in cells, it was highly important to establish that nanosensor introduction did not induce any cellular toxicity or changes in IRP.

In this chapter, results are presented on investigations into targeted cellular delivery of nanosensors and their cytotoxic effects.

4.2 Cytosolic Nanosensor Delivery

The uptake of NQ-NS and HQ-NS by cells in CS-free media was investigated using TEM. This is a type of high resolution microscopy, in which a beam of electrons is passed through ultra-thin samples. Images are then formed from the interactions of the electrons transmitted through the specimen and captured on photographic film, or more commonly nowadays, with a digital camera.[104] TEM is an excellent imaging technique for examining nanosensor localisation because cells can be resolved at the organelle level and gold nanoparticles appear well contrasted against the cell due to their relatively high electron density.[105,106]

Figure 4.2 below shows that, under these culture conditions, nanosensors were taken up by cells into the cytoplasm. The TEM images in figure 4.2 also revealed that the nanosensors were neither encapsulated nor coated with lipids. Further TEM images are provided in appendix 3.

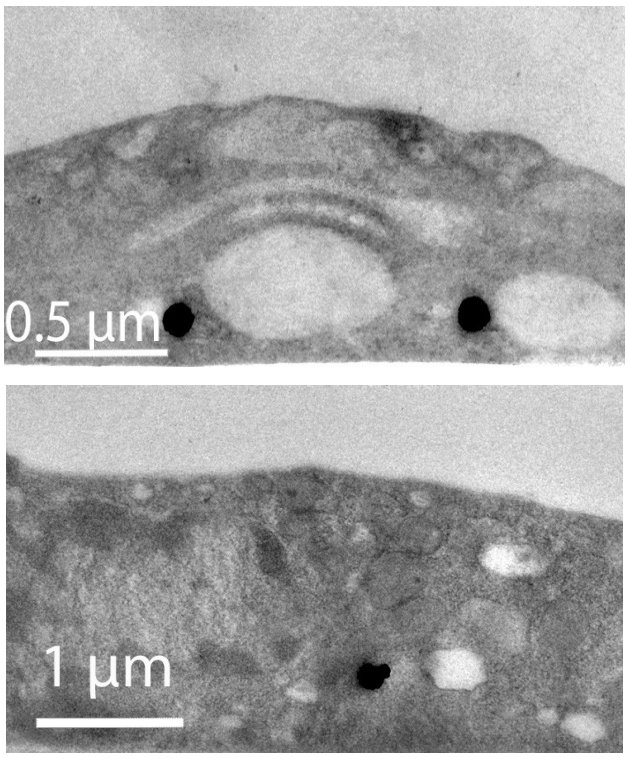

Figure 4.2: TEM images of nanosensors in cells. The top image shows nanosensors (dark spots) in the cytoplasm beside rough ER. The bottom image shows nanosensors in the cytoplasm just outside the nucleus. Scale bars in white on the images.

Figure 4.2 demonstrates that, with the correct delivery conditions, modified NS can be controllably delivered to the cytoplasm, where they reside freely. Importantly, it also demonstrates their potential utility in sensing cytoplasmic RPs.

4.3 Nuclear Nanoparticle Delivery

As outlined in chapter 1, RP varies from organelle to organelle.[6,8] With gold nanoparticles, significant scope exists for targeting organelles, other than the cytoplasm, through surface tagging with small molecules and peptides.[107,108,109]

Nuclear localisation sequences (NLSs) were first discovered in the large viral protein T-antigen, encoded by the SV40 virus.[110] This particular NLS comprises a highly basic and positively charged stretch of seven AAs (^{126}PKKKRKV^{132}).[110] The second

lysine residue Lys-128 is an absolute requirement for nuclear localisation, with the surrounding AAs being less specific.[110] Since the discovery of this NLS in 1984, several other NLSs have been reported.[111,112]

Figure 4.3 below shows a representation of the nuclear import of NLS-tagged cargo.

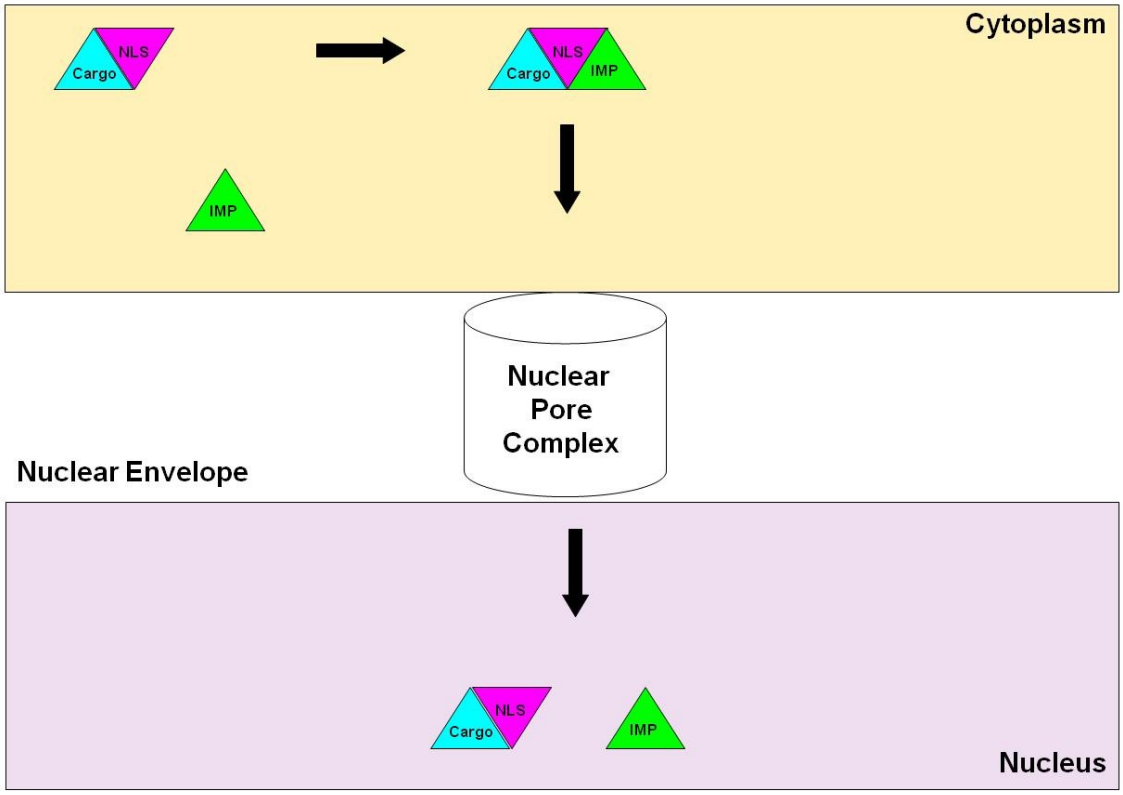

Figure 4.3: Mechanism of NLS import whereby an NLS sequence is recognised by importins and then taken into the nucleus across the nuclear pore complex with its cargo.

In the cytoplasm, NLSs are recognised by importins and form a complex that is localised to the nuclear envelope and then translocated through the nuclear pores in an ATP-dependent process.[113] Once inside the nucleus, the complex is degraded and the peptide and its cargo are released.[113]

Recently, several groups have shown that NR functionalised with a NLS can be successfully delivered to cell nuclei.[108,109]

In these experiments, two novel NLSs (CA-NLS 1 and CA-NLS 2), based on the SV40 NLS (PKKKRKV), were synthesised via solid-phase peptide synthesis (SPPS) and assembled on NR. NR were used, due to the fact that the NS used in the previous work were too large to cross the nuclear pore complexes (NPCs). NPCs are ~120 nm in diameter[114] and thus too small to allow the NS (150 nm in diameter) to cross from the cytoplasm into the nucleus. NR on the other hand are only 10 × 38 nm in size and, when functionalised with NLS peptides, should be able cross the nuclear envelope through NPCs. Like NS, the NR also had a plasmon resonance close to 785 nm, making them similarly ideal for intracellular/intranuclear SERS measurements.[115,116]

4.3.1 Solid-Phase NLS Peptide Synthesis

Pioneered by Merrifield in the 1960s,[117] SPPS proved to be something of a revolution in bio-organic chemistry. SPPS involves the construction of AA sequences on linker molecules attached to insoluble support resins.[117] Once assembled, the desired AA sequence can be cleaved from the support, using e.g. HF or TFA (preferable).[117] SPPS offers significant advantages over peptide syntheses performed in solution, including: higher coupling efficiencies, simpler purifications and orthogonal protecting group strategies for reactive AA side chains.[117]

CA-NLS 1 and CA-NLS 2 were both sequenced on aminomethyl polystyrene resin, functionalised with rink amide linker (labile under mild acidic conditions), using an Fmoc protecting group strategy. A key advantage of the Fmoc protecting group is orthogonality.[117] It is a base labile protecting group. Reactive AA side chains can, therefore, be protected with acid-labile protecting groups, which are removed and scavenged when the peptide is cleft from the resin under acidic conditions.[117]

In the synthesis of CA-NLS 1, DIC was used to activate carboxyl groups of incoming AAs to ensure faster, more efficient couplings, whereas HBTU was used for this purpose in the synthesis of CA-NLS 2. Mechanisms for AA couplings, Fmoc deprotection and peptide cleavage from the resin are shown in appendix 4.

Figure 4.4 below shows the structure of both CA-NLS 1 and CA-NLS 2.

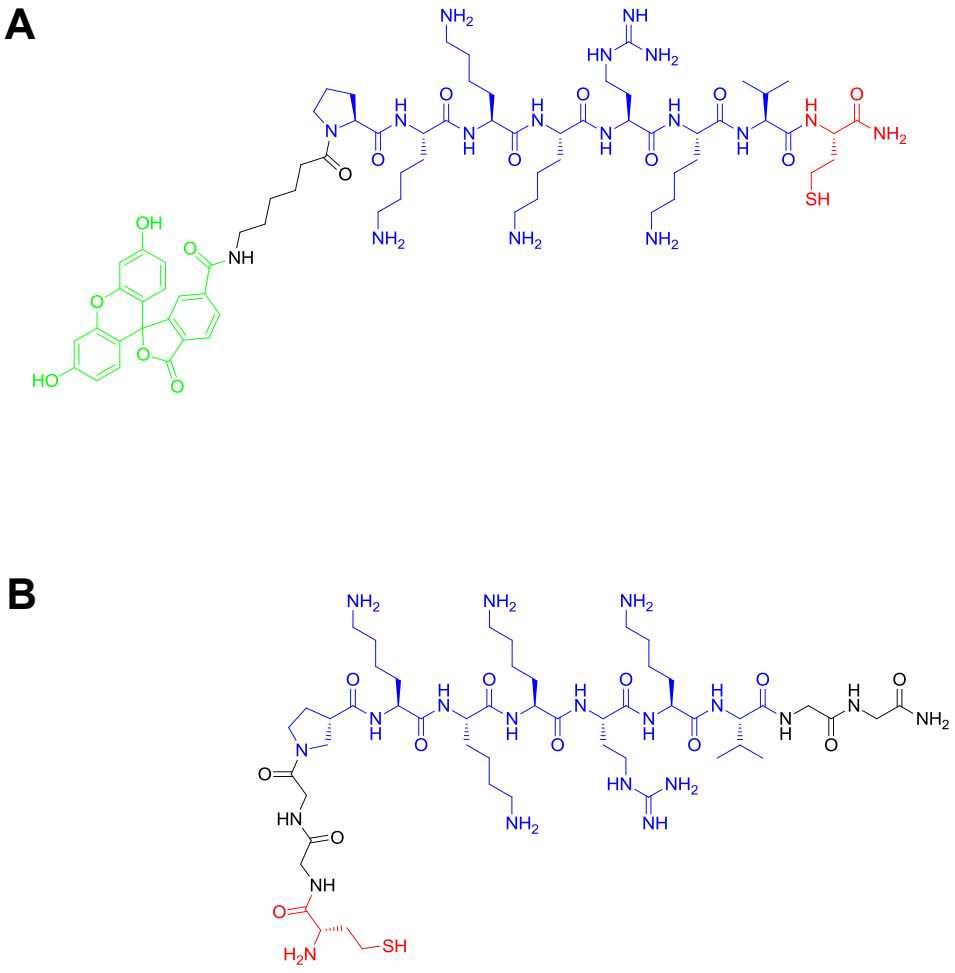

Figure 4.4: Molecular structures of **(A)** CA-NLS 1 and **(B)** CA-NLS 2. NLS is highlighted in blue, spacer groups are highlighted in black, cysteine residues are highlighted in red and fluorescein is highlighted in green.

Both CA-NLS 1 and CA-NLS 2 had the PKKKRKV NLS, in order to allow NR penetration of the nuclear membrane, spacer groups and cysteine residues, which permitted chemisorption to NR through their thiol moieties. CA-NLS 1 was also designed to incorporate fluorescein to allow intracellular detection of NR with fluorescence microscopy.

4.3.2 Characterisation of NLS Functionalised NR

The absorption spectra of NR, functionalised with both CA-NLS 1 and CA-NLS 2, displayed red-shifts, slight broadening of peaks and a dampening of peak intensity, compared to cetyltrimethylammonium bromide (CTAB)-coated NR.[108,118] These observations were a clear indication of peptide attachment to the surface of the NR.

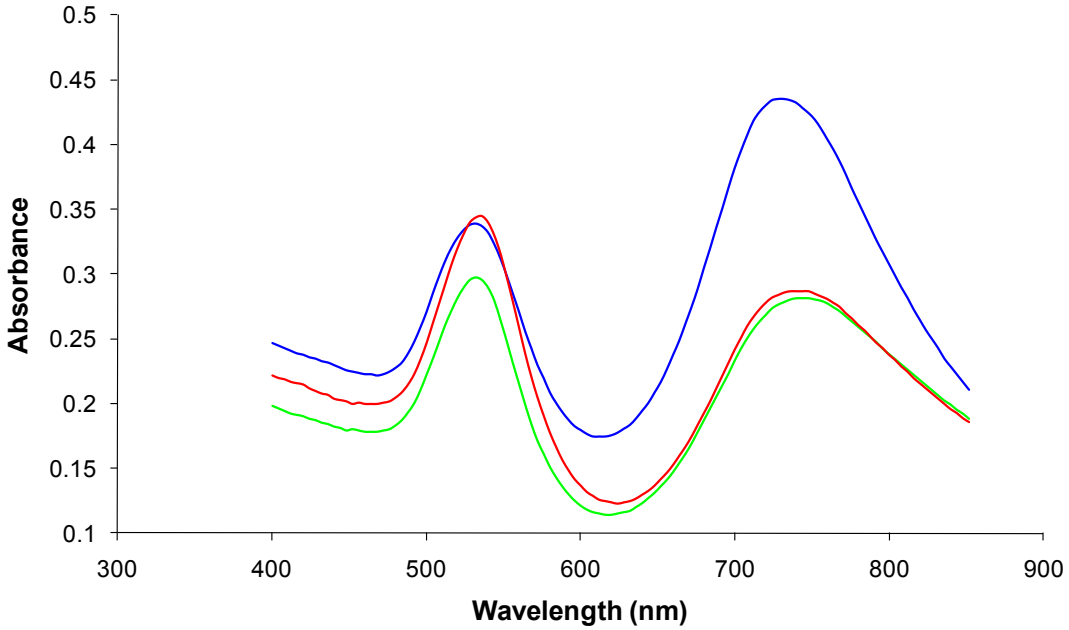

Figure 4.5: Absorption spectra of CTAB-NR (blue line), CA-NLS 1-NR (green line) and CA-NLS 2 (red line). A red-shift, peak broadening and dampening of peak absorbance is noted as NR are functionalised with NLS peptides.

SERS was also used to confirm surface attachment of the NLS peptides to NR (figure 4.6).

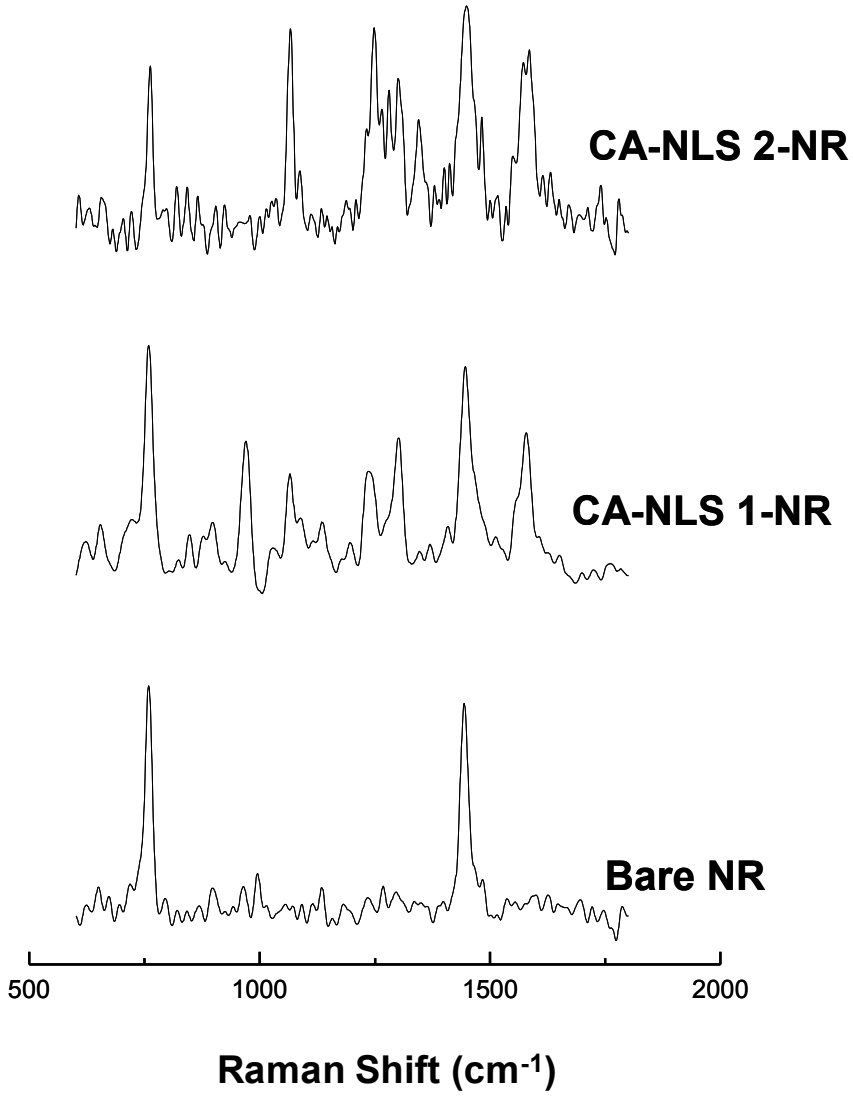

Figure 4.6: SERS spectra of bare NR, CA-NLS 1-NR and CA-NLS 2-NR.

Figure 4.6 shows a comparison of the SERS spectra from CTAB-capped NR and those functionalised with CA-NLS 1 and CA-NLS 2. It was observed that NLS functionalised NR showed some overlapping signals from the CTAB molecules. These included both the C-N stretching and CH_2 bending vibrations at 761 cm^{-1} and 1444 cm^{-1} respectively.[119] Tables 4.1 and 4.2 below provide tentative assignments of the vibrational modes observed in the SERS spectra of CA-NLS 1 and CA-NLS 2 respectively.[120,121]

Wavenumber (cm^{-1})	Assignment
1577	Amide stretching
1445	AA C-H bending overlapping with CTAB CH_2 bending
1301	Lysine CH_2 wagging
1232	Arginine CH_2 wagging
1132	Xanthene ring vibrations
1062	Proline C-N stretching
968	C-C aliphatic vibrations
758	AA COO^- deformation overlapping with CTAB C-N stretching

Table 4.1: Vibrational assignments of CA-NLS 1. Assignments were made according to the literature.

Peak Position (cm^{-1})	Assignment
1583	Amide stretching
1446	AA C-H bending overlapping with CTAB CH_2 bending
1344	Glycine CH_2 wagging
1300	Lysine CH_2 wagging
1245	Arginine CH_2 wagging
1066	Proline/glycine C-N stretching
761	AA COO^- deformation overlapping with CTAB C-N stretching

Table 4.2: Vibrational assignments of CA-NLS 2. Assignments were made according to the literature.

4.3.3 Fluorescence Imaging of NLS Functionalised NR in Nuclei

NR functionalised with CA-NLS 1 were introduced into cells using the same CS-free culture conditions for the cytoplasmic delivery of NQ-NS and HQ-NS. Fluorescence microscopy was used to investigate successful delivery of NR into the nuclei of cells.

In these experiments, nuclei were stained with Höescht dye, which binds to DNA and emits blue fluorescent light around 460 nm when excited by UV light.[122] Using a digital camera and an appropriate light filter, images of cell populations were then recorded and locations of nuclei determined according to the blue fluorescent light emitted by the Höescht molecules (figure 4.7).

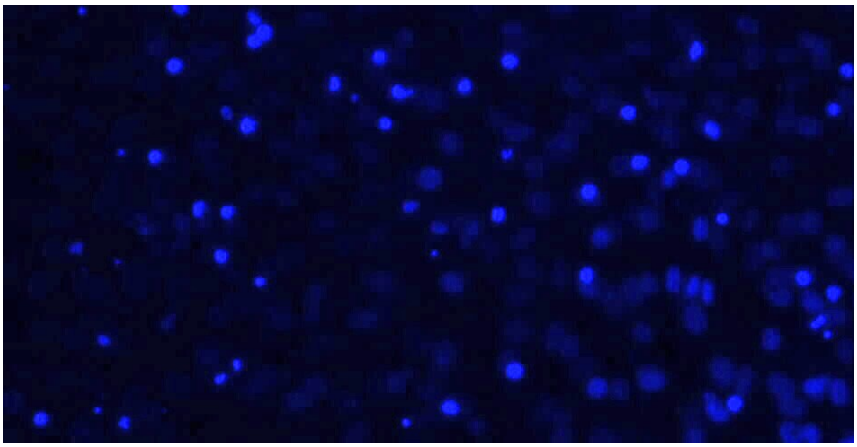

Figure 4.7: Fluorescence image of cells incubated with Höescht dye. Nuclei appear bright blue.

When excited by UV light, the fluorescein moiety possessed by CA-NLS 1 emitted green light around 520 nm.[105] As with the Höescht visualisation of cell nuclei, a digital camera and appropriate light filter were used to determine intracellular localisation of the NR (figure 4.8).

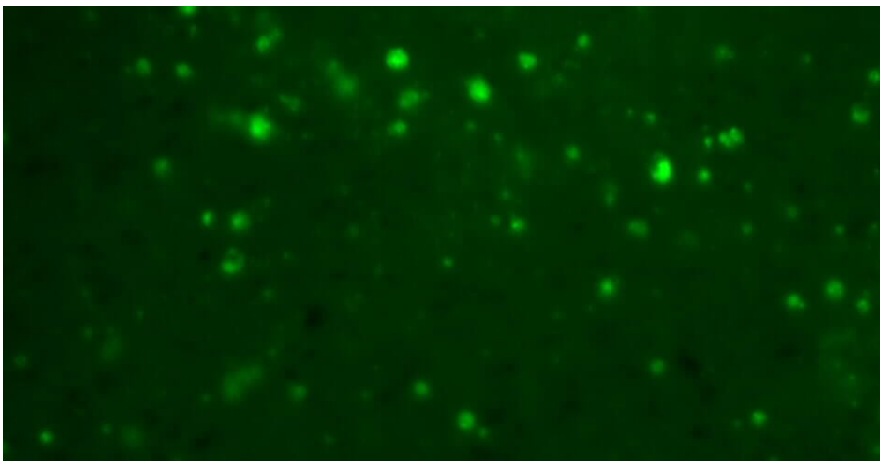

Figure 4.8: Fluorescence image of cells incubated with CA-NLS 1-NR dye. Presence of CA-NLS 1-NR indicated by bright green light emitted from fluorescein moiety.

When the images in figures 4.7 and 4.8 are superimposed, there were clearly significant overlapping regions of blue and green fluorescent light (figure 4.9). The co-localisation of green light emitted from the fluoresceins of CA-NLS 1-NR with the blue light emitted from the Höescht dye (a well established DNA stain) clearly indicated successful delivery of NR into the nuclei of cells.

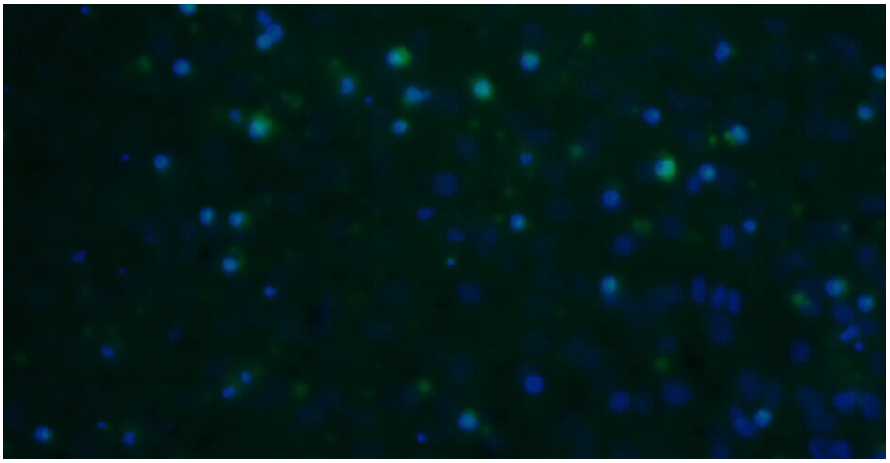

Figure 4.9: Overlay of figures 4.7 and 4.8. Turquoise areas indicate co-localisation of blue Höescht dye and green light emitted from the fluorescein moieties of CA-NLS 1-NR.

It can be seen from figure 4.9 that there are multiple regions of overlap between figures 4.7 and 4.8 where CA-NLS 1-NR have successfully transfected the nucleus. There are also regions where the NR appear to be residing in the cytoplasm (i.e. green light emitted from the fluorescein is not overlapped by the blue light of Höescht dye).

4.3.4 TEM Imaging of Functionalised NR in Nuclei

For further confirmation of nuclear delivery of NLS functionalised NR, TEM images were obtained from cells which had been incubated with CA-NLS 2-NR in a pilot study.

As with the fluorescence imaging experiments, TEM indicated successful transfection of the nucleus with NLS functionalised NR (figure 4.10).

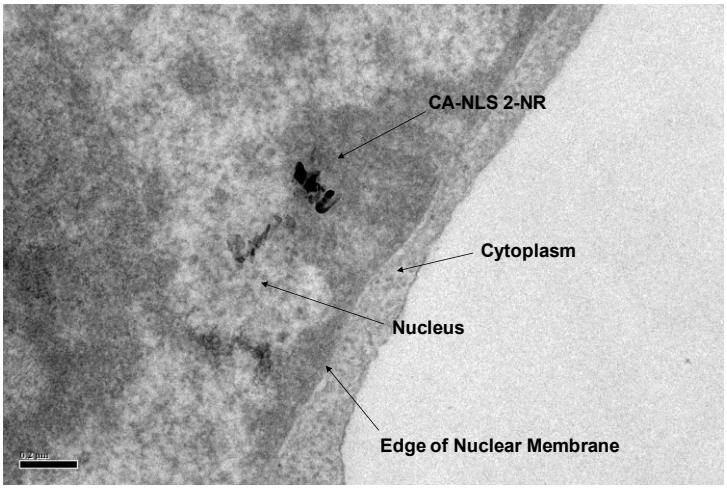

Figure 4.10: TEM of CA-NLS 2-NR (dark rod shapes) in nucleus. Nuclear membrane, nucleus and cytoplasm indicated by arrow in the image. Scale bar = 200 nm.

The TEM study did, however, present several images of CA-NLS 2-NR that appeared to be trapped in vesicles just outside the nuclear membrane (figure 4.11).

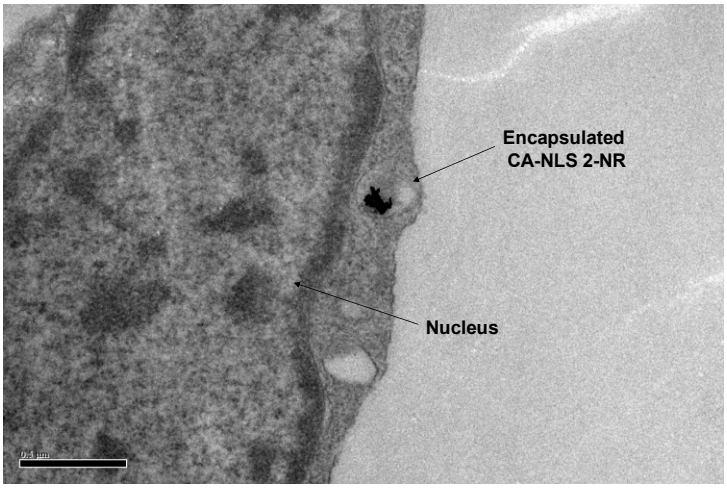

Figure 4.11: TEM of CA-NLS 2-NR trapped in vesicle outside nucleus. Encapsulated CA-NLS 2-NR indicated by arrow in the image. Scale bar = 500 nm.

This suggests that, for more efficient nuclear transfection of nanomaterials, it may be prudent to use NLS peptide sequences in conjunction with, for instance, endosomal disruption peptide sequences.[123]

4.4 Nanosensor Toxicity Study

To determine whether or not nanosensor introduction resulted in any cytotoxicity, or initiating processes known to be accompanied by a change in IRP, several standard cellular assays were employed. ROS generation, apoptosis, cell viability and cellular glutathione status were all investigated.

4.4.1 DCFH-DA Assay of Oxidative Stress

The DCFH-DA assay is a well established technique for identifying any increase or accumulation of ROS in cells.[124,125] Figure 4.12 shows the mechanism of action for DCFH-DA.

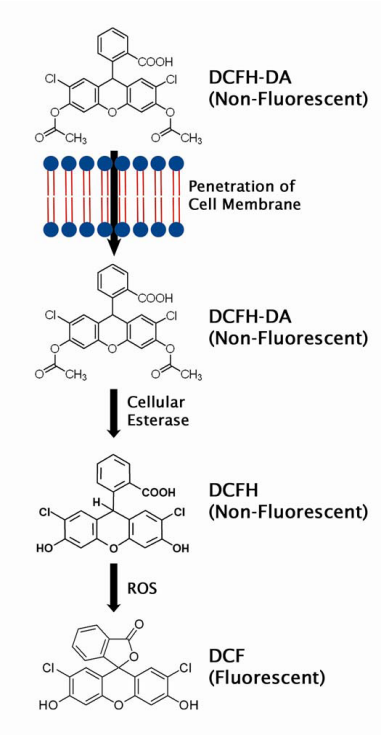

Figure 4.12: DCFH-DA mechanism of action. Non-fluorescent DCFH-DA is taken up by cells where it is enzymatically converted to DCFH. If excess ROS are present DCFH is converted to the fluorescent DCF.[126]

The membrane-permeable, non-fluorescent DCFH-DA is introduced into cells, where it is deacetylated by cellular esterase enzymes to 2',7'-dichlorfluorescein (DCFH) (which is also non-fluorescent).[126] The generation of ROS is then detected by fluorescence through the formation of the 2',7'-dichlorfluorescein (DCF).[126]

This assay was carried out on cells which had been incubated with functionalised NS in CS-free media for 5 h. Untreated cells (-ve control) and cells which had been treated with either Zn (1 mg/ml) or tBOOH (0.5 mM) (well established +ve controls)[127],[128] were also assayed for comparison. Results shown below, in figure 4.13, were obtained in collaboration with C. McGuinness (University of Edinburgh).

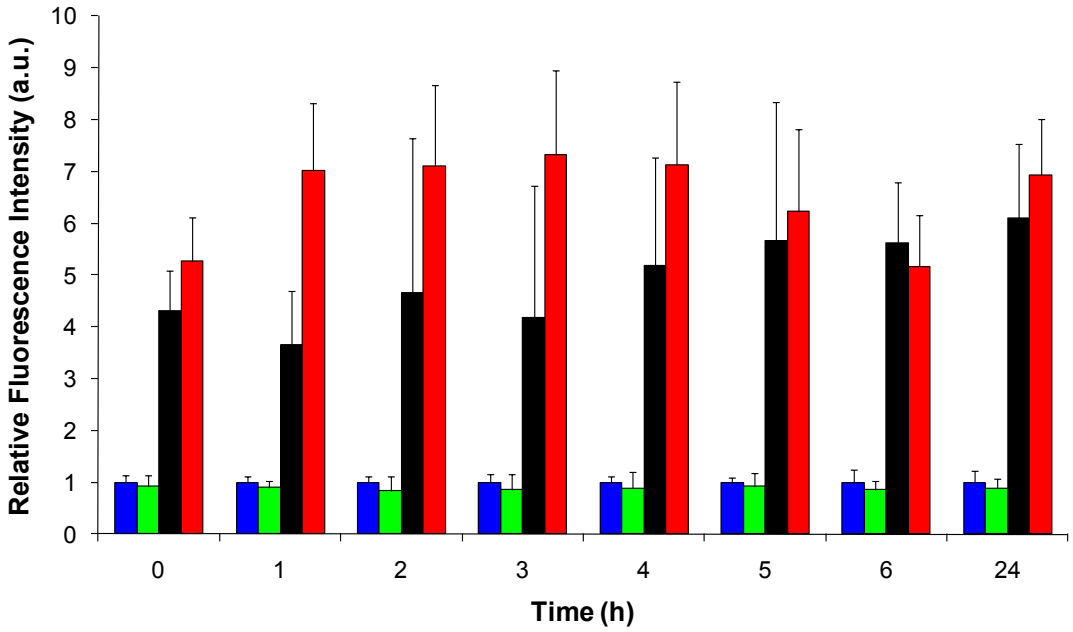

Figure 4.13: DCFH-DA assay results which show that nanosensor introduction does not result in any cellular oxidative changes. Untreated cells (blue bar), cells incubated with nanosensors (green bar), Zn +ve control (black bar) and tBOOH +ve control (red bar).

Results from the DCFH-DA assay clearly show that, while, as expected, Zn and tBOOH induced a strong oxidative change in the cells, NS did not induce any detectable oxidative changes over a 24 h time period (figure 4.13). The result of this assay confirmed that modified NS do not themselves induce formation of ROS in cells.

4.4.2 APOP*ercentage* Assay

A standard assay of apoptosis, the APOP*ercentage* assay, was used, in order to determine whether or not the introduction of nanosensors into cells was causing them to undergo programmed cell death. Progression of the apoptotic pathway is well known to be accompanied by an increase in IRP.[6,129]

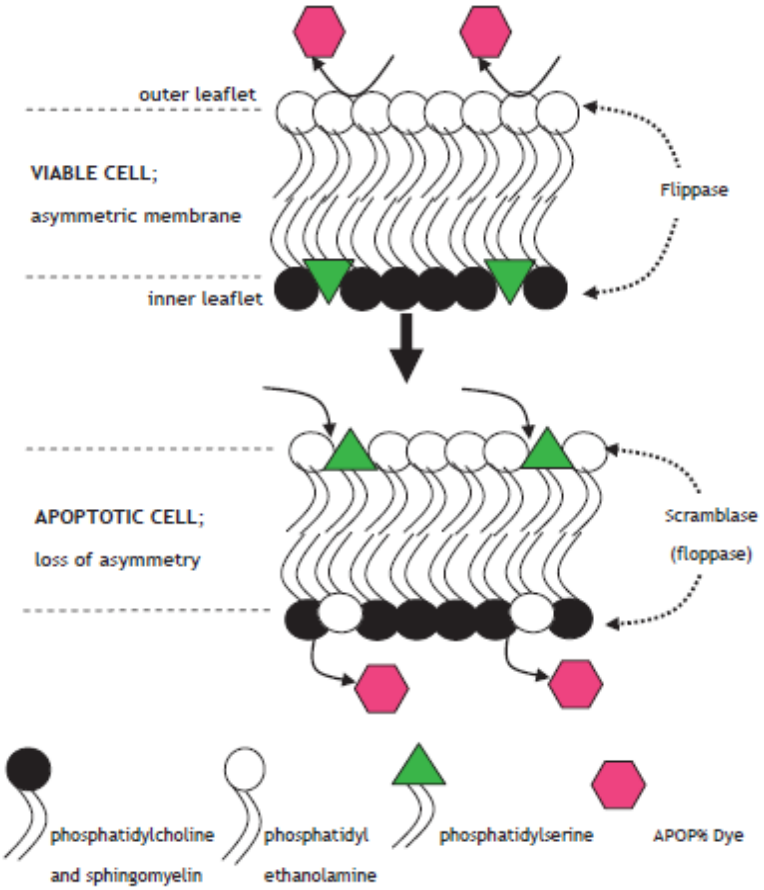

Figure 4.14: APOP*ercentage* mechanism of action. Flippase enzyme ceases to maintain the asymmetric phospholipids bilayer and APOP% dye is taken up by cells committed to apoptosis. [130]

Mammalian cell membranes are asymmetric phospholipids bilayers.[17] In order to ensure cell viability, it is crucial that membrane structure is not distorted in any way. An enzyme known as flippase helps cells to maintain an asymmetric phospholipid bilayer.[130] However, in apoptotic cells, flippase regulation is either overwhelmed, or inactivated by the activity of the enzyme 'scramblase'.[130]

In the APOP*ercentage* assay, the APOP% dye is taken up by apoptotic-committed cells that have undergone membrane scrambling as shown in figure 4.14.[130] Following transmembrane movement, the APOP% dye enters the cell and continues

to do so until blebbing occurs.[130] Once taken up by apoptotic cells, the APOP% dye is retained and its presence confirmed with a fluorescence microplate reader.[130]

This assay was applied to cells incubated with nanosensors to ascertain whether or not their introduction was resulting in apoptosis. Untreated cells were also assayed for comparison. Cells treated with staurosporine (1 μM), a compound known to induce apoptosis,[131] were assayed as a positive control. Fluorescence intensities were normalised and reported as a percentage against the positive staurosporine control (figure 4.15).

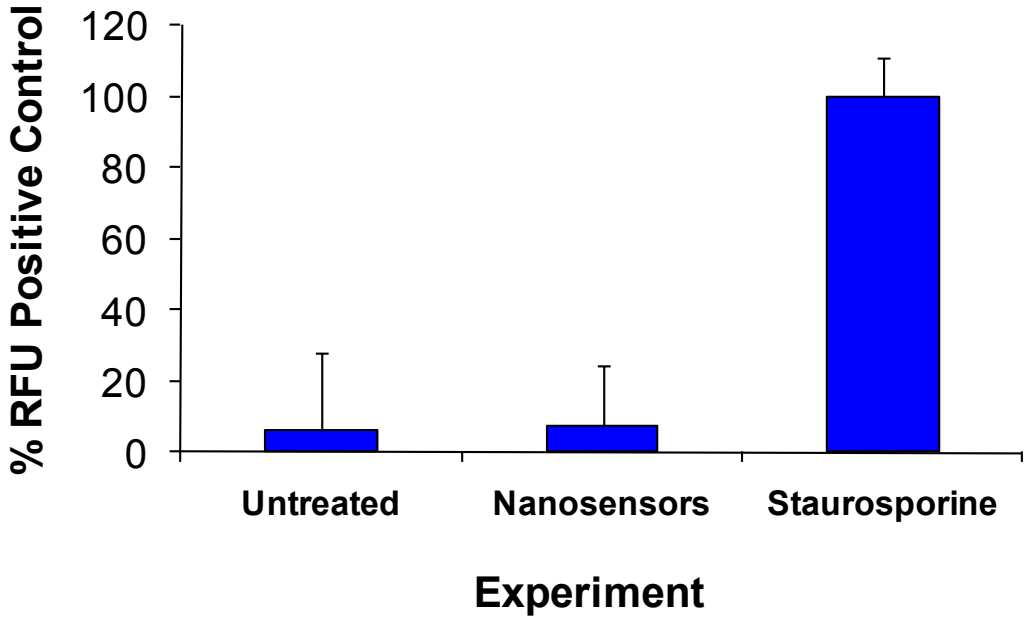

Figure 4.15: APOP*ercentage* assay results. While there is a clear increase in the % RFU of staurosporine treated cells vs. untreated cells, little difference is seen in the % RFU between the untreated cells and those treated with nanosensors. This indicates that the nanosensors are not inducing apoptosis.

As can be seen from figure 4.15, the % RFU of staurosporine for the untreated cells and those treated with nanosensors were both relatively low and comparable. The indication from this assay was that nanosensor introduction did not result in apoptosis and thus no oxidative increase in IRP.

4.4.3 MTT Assay

The MTT assay is a standard colorimetric assay, used to assess cell proliferation and viability, i.e. lack of cytotoxicity. MTT is a yellow tetrazole and, in healthy cells, is reduced by mitochondrial reductase enzymes to insoluble purple formazan crystals (figure 4.16).[132,133]

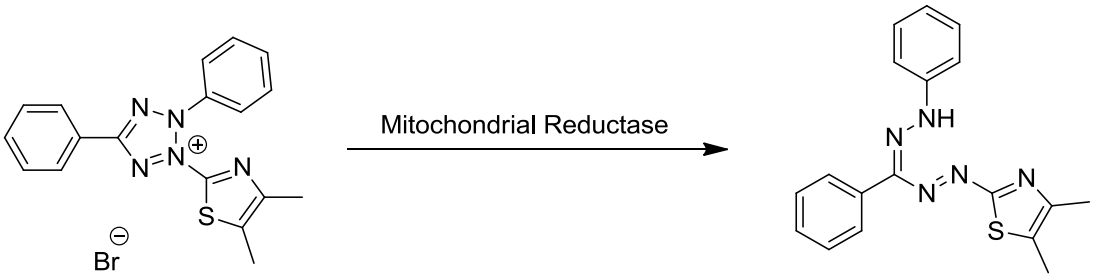

Figure 4.16: MTT reaction in healthy cells. MTT (yellow) is reduced in healthy cells by mitochondrial reductase enzymes to form formazan crystals (purple).

A solubilisation solution is added, to dissolve the insoluble purple formazan product into a coloured solution.[133] Absorbance values are then read spectrophotometrically at 570 nm and cell viability is calculated according to equation 2.2 (page 41).

Figure 4.17 below shows the viability of cells treated with NQ-NS.

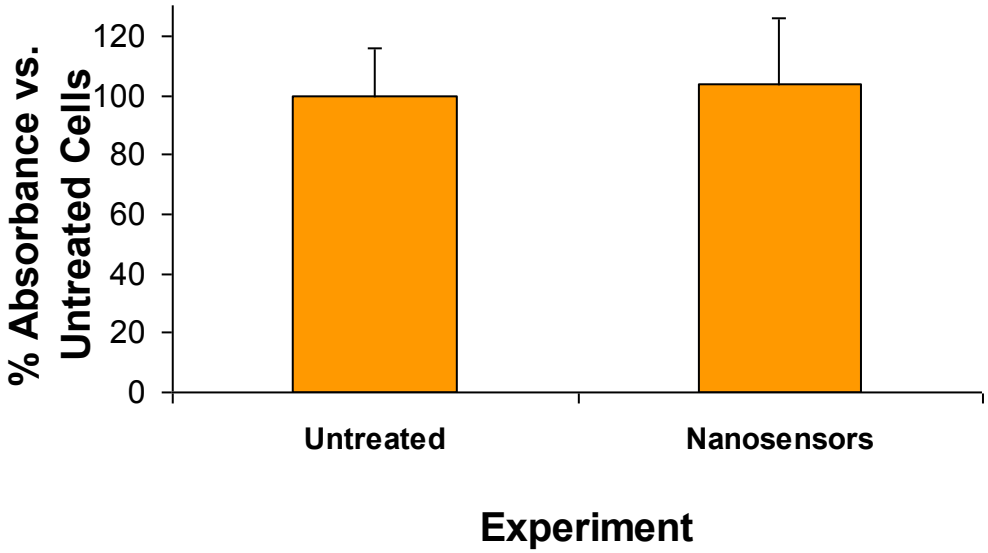

Figure 4.17: Cell viability determined from the MTT assay. Little difference is observed in the absorbance of untreated cells vs. those treated with nanosensors. This indicates that the nanosensors are not affecting cell viability.

The calculated cellular viability from the absorbance values was 103 ± 22% for NQ-NS treated cells. These results indicated no significant stimulation or inhibition of cell viability or growth, as a result of nanosensor introduction. That is, no cytotoxic effects were observed through the MTT assay.

4.4.4 GSH-Recycling Assay

As outlined in the introduction, the GSH-recycling assay is a well established indicator of cellular redox status.[47] According to the [GSH]:[GSSG] ratio, an estimate of IRP can be made with the Nernst equation.[6] This assay was used to determine whether or not the nanosensors used in this work were perturbing the [GSH]:[GSSG] ratio and thus affecting the IRP.

Total GSH and GSSG levels of untreated cells and those treated with nanosensors were determined in triplicate from standard curves (appendix 7) and quoted in μM against the total protein content of the cells, as reported by the BCA protein assay (a

colorimetric technique, in which protein concentrations of cell populations are quantified through changes in absorbance). Total protein content was also determined from a standard curve but was expressed in mg (appendix 7).

Total GSH levels were found to be 0.295 and 0.264 μM/mg for untreated and nanosensor-treated cells respectively. GSSG levels were found to be 0.0095 and 0.0074 μM/mg for untreated and nanosensor treated cells respectively. These results showed no significant difference in GSSG percentage between untreated cells (3.1%) and nanosensor-treated cells (2.8%). This confirms that the redox state of the cell remains unperturbed after treatment with nanosensors.

4.5 Conclusions

In this chapter it has been shown that SERS-active redox nanosensors can be selectively delivered to the cytoplasm of mammalian cells. Furthermore, through careful tuning of nanoparticle surface chemistry, an exciting opportunity to facilitate their access to other organelles has been presented. Monitoring redox poise in organelles such as the nucleus or mitochondria would enhance our understanding of oxidative stress.

While it has previously been demonstrated that nanomaterials such as TiO_2 fibres and carbon nanotubes can cause toxicity to cells,[96,97,98] gold nanoparticles have been used extensively in biology and in the medical field.[99] Importantly, in this work, it has been demonstrated that introduction of these nanosensors does not promote any cytotoxic events associated with oxidative stress such as ROS generation, apoptosis or necrosis. It has also been demonstrated that the cellular [GSH]:[GSSG] ratio is unperturbed by nanosensor addition.

Chapter 5

Measuring and Monitoring Intracellular Redox Potential with SERS-Active Redox Nanosensors

5.1 Introduction

In chapter 3, the possibility to quantify changes in RP rapidly and reversibly with SERS nanosensors was demonstrated. It was also shown, in chapter 4, that these sensors can be controllably delivered into cells without causing any cytotoxic side-effects. With the fundamentals for an ideal redox-monitoring system in place, the biological efficacy of the nanosensors in measuring and monitoring IRPs was investigated.

In recent years, Raman spectroscopy has emerged as a very useful cellular-imaging technique. Through confocal Raman mapping, Uzunbajakava *et al* have demonstrated the possibility of charting DNA, RNA and protein distribution in apoptotic cells.[134] The ability to use information-rich vibrational spectroscopy, in a non-invasive manner, to elucidate physiological processes is exciting and emphasises the potential of Raman spectroscopy to further our understanding of the complex biological processes which define cells.

Raman mapping has even been used to study cellular response to drug treatments. Using a single cell, Draux *et al* were able to exploit the specificity and sensitivity of Raman mapping to changes in biomolecule structure, in order to investigate the effects on Calu-1 cells of gemcitabine (a chemotherapeutic drug used in the treatment of lung cancer).[135] Through principal component analysis (PCA) of Raman maps, the inhibition of DNA synthesis and repair by the anti-tumour drug were

shown.[135] The work of Draux *et al* serves as an example of how Raman spectroscopy, specifically Raman mapping, can obtain useful clinical information from cells, which could have an impact on diagnostics and patient treatments.

Coherent anti-Stokes Raman spectroscopy (CARS) is a variant of Raman spectroscopy that has similarly been used to probe cellular environments. CARS is a type of nonlinear Raman spectroscopy that offers users similar chemical information to that of regular Raman spectroscopy.[61] By its nature, CARS makes it is possible to obtain spectra that are free from the effects of fluorescence, which is its main advantage.[61]

In February 2011, Pezacki *et al* published a review detailing the use of CARS in live cell imaging.[136] The review highlights, particularly, the utility of CARS in studying lipids, without any perturbation to live cells.[136] Through lipid studies with CARS, important information can be obtained on cellular metabolism, which may further our understanding of disease states including obesity, diabetes, cardiovascular disease, neurodegeneration and cancer.[136]

Importantly for this work, SERS has also been shown as an excellent technique for cell imaging and bio-sensing.[137,138,139] Detection of disease states and viruses, using tagged nanoparticles and SERS, is well documented.[66,140] The ability to detect changes in intracellular environmental factors, notably pH, has also been confirmed, using nanoparticles tagged with the small pMBA reporter molecules.[70]

The precedents set in these studies meant that the nanosensors developed in this work were expected to perform as bio-sensors for redox measurements. In doing so, they would allow the ultimate aims of the work to be achieved and RP could be monitored quantitatively and reversibly during interesting and relevant physiological events.

In this chapter, results are presented on normoxic cytoplasmic RP measurements, as well as the monitoring of cytoplasmic RPs in response to superphysiological reductive and oxidative stimuli. Furthermore, the abilities of the nanosensors to quantify changes in RP during apoptosis (induced by staurosporine and H_2O_2) and as cells responded to the introduction of miR-199a-3p are reported.

5.2 Measuring Homeostatic Cytoplasmic RPs

Before any attempts were made to monitor changes in IRP with the nanosensors developed in this work, it was first necessary to monitor the resting/homeostatic IRP and to ensure that this remained constant over an extended period. It would be reasonable to expect that the homeostatic IRP would be similar to those already reported as the nanosensors did not induce any cytotoxicity when introduced into cells.

Cytoplasmic potentials in live cells were measured using both NQ-NS and HQ-NS. As expected, HQ-NS is fully reduced under conditions of normal cellular physiology (figure 5.1) and can, therefore, be considered insensitive in this potential window.

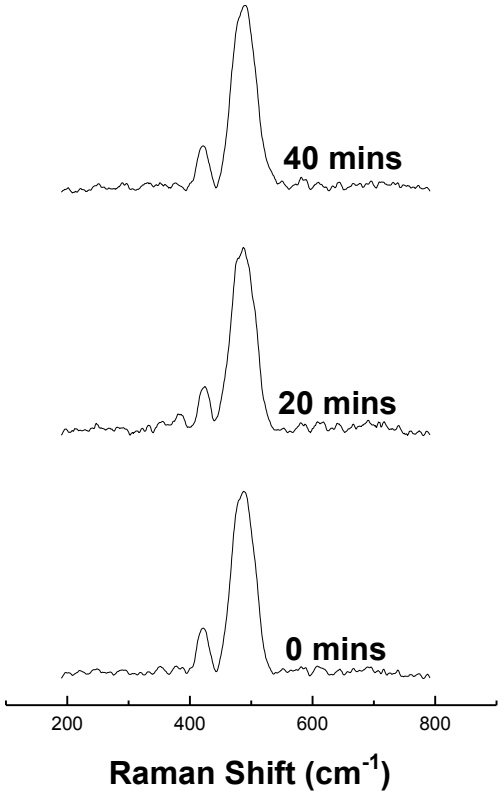

Figure 5.1: HQ-NS as a normoxic cytoplasmic RP sensor. When fully reduced no peak is visible at 356 cm^{-1} and therefore resting cellular potential cannot be accurately estimated using HQ-NS. SERS spectra of HQ-NS from single cells display no noticeable variation over a 40 min period.

Figure 5.2 shows the measured potential of NQ-NS over a 40 min period and confirms that the potential is not only invariant while making measurements over this period, but is similar throughout the three independent measurements made.

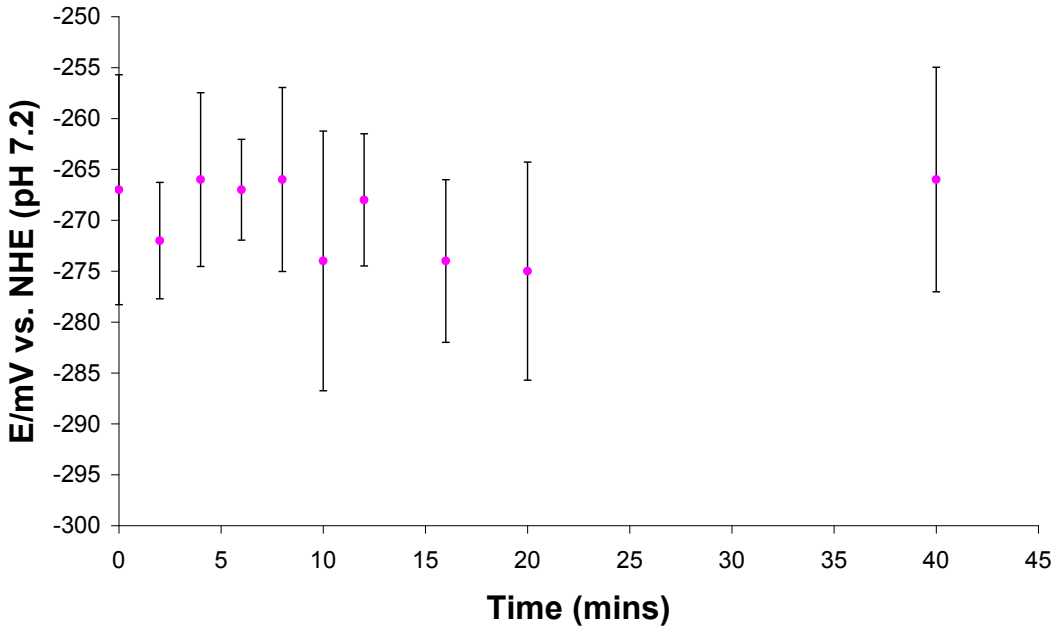

Figure 5.2: NQ-NS as a normoxic cytoplasmic RP sensor. Potential calculated from the 1577/1645 cm^{-1} peak ratio. Error bars indicate the standard deviation of measurements taken during three independent experiments from single cells.

At resting cellular potential, however, NQ-NS is approximately 36% reduced. This corresponds to a potential of -290 mV vs. NHE and is in good agreement with previously reported cytosolic potentials, which range from -315 to -280 mV vs. NHE.[6,50] This also serves to once again highlight that the nanosensors are non-toxic to cells as no oxidative or reductive variations in IRP are observed during the period of monitoring.

5.3 Monitoring Oxidative Stress

Since HQ-NS is sensitive to higher potentials outside those found under normoxic conditions, its utility was investigated under conditions known to cause oxidative stress in the cell. Oxidative stress was induced with AAPH (30 mM) – a membrane-permeable, free radical initiator, which generates a variety of ROS species, including $O_2^{\cdot -}$, through the oxidative stress pathway and which is well-known to cause cellular oxidative damage.[141,142]

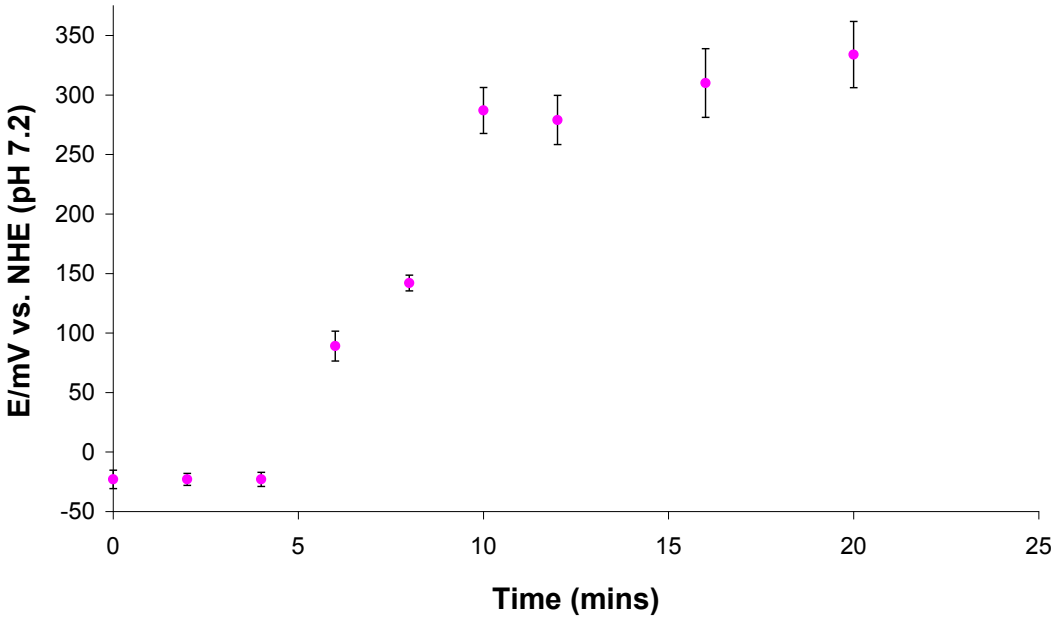

Figure 5.3: HQ-NS as a sensor of oxidative stress caused by AAPH. calculated from the 477/356 cm^{-1} peak ratio. Error bars indicate the standard deviation of measurements taken during three independent experiments.

From figure 5.3 it can be seen that only 6 mins after cells were exposed to AAPH, there is a measurable change in the cytoplasmic RP. The measured potentials are significantly more oxidative than those within the redox buffering range of the GSH system, indicating that this degree of oxidative stress cannot be dealt with by the cell's natural antioxidant system. Generation of $O_2^{\cdot -}$ by AAPH and its subsequent conversion to H_2O_2 (by SOD) are both known to proceed with rate constants in the

order of 10^9 $M^{-1}s^{-1}$.[142] It is, therefore, likely that the rapid formation of H_2O_2 leads to complete oxidation of cellular glutathione, resulting in a fast change in IRP, as observed here.

5.4 Sequential Monitoring of Reductive and Oxidative Changes in Intracellular Redox Potential

In order to maximize the potential range over which we can monitor, we combined the reductive sensitivity of NQ-NS with the oxidative sensitivity of HQ-NS and carried out a series of measurements under both oxidative and reductive stress. The combination of NQ-NS and HQ-NS means that the cytoplasmic potential can be monitored across a total of 450 mV, a previously unattainable range in a rapid and reversible manner with a gap of *ca.* 200 mV between the two sensors (figure 5.4). This functional range encompasses the hypoxic conditions in which tumours reside in order to avoid cell death mechanisms at one extreme and the oxidative conditions which are associated with a variety of inflammatory and degenerative disorders and ultimately cell death at the other. For comparison, roGFP can monitor from approximately −325 to −195 mV. REF

The cytoplasmic potential was monitored over 40 min using both NQ- and HQ-NS in tandem. During this period DTT and AAPH were added to the cell's media (indicated on figure 5.4) and changes in the ratios of the peaks at 1577/1645 and 356/477 cm^{-1} were monitored from NQ- and HQ-NS respectively.

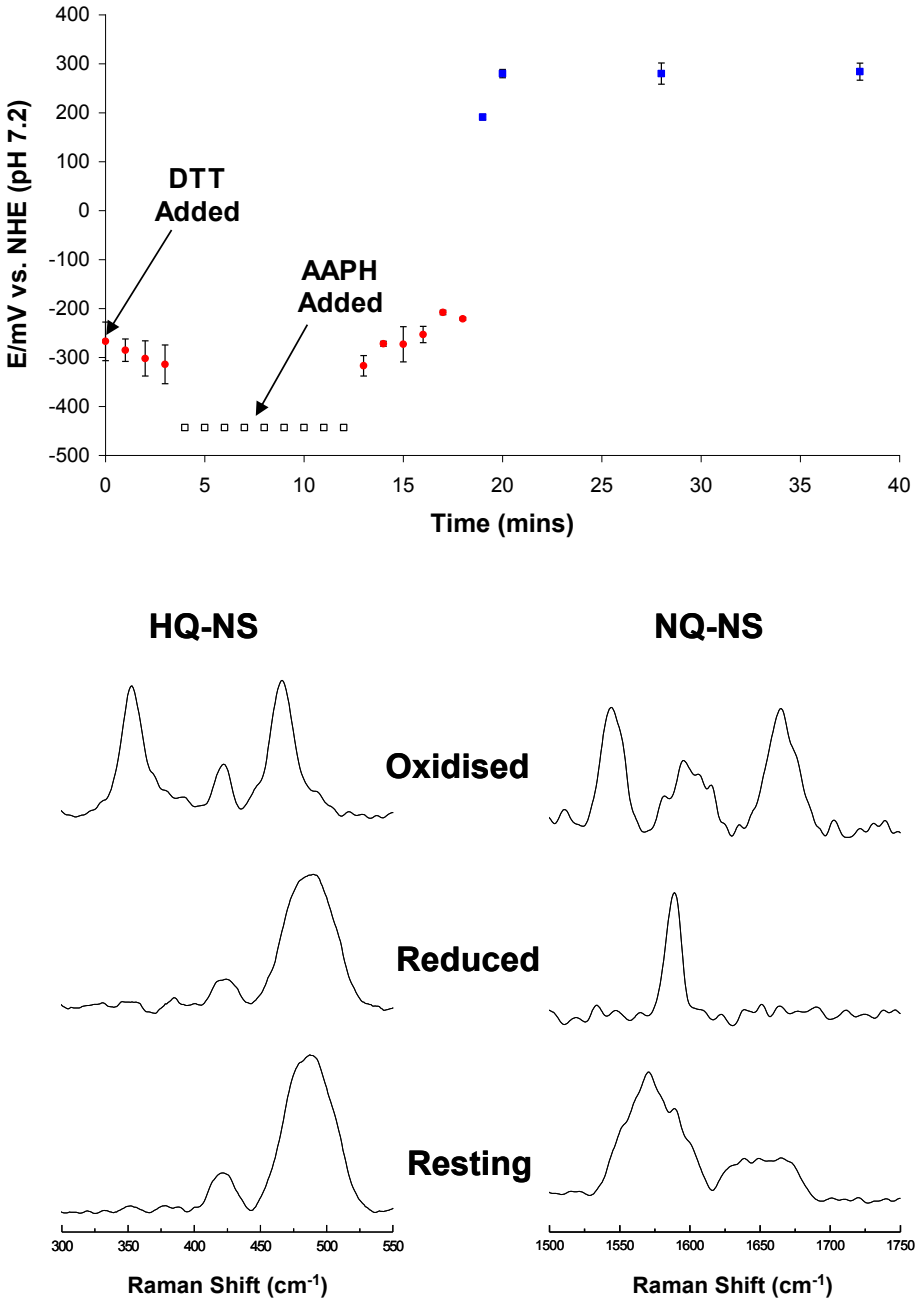

Figure 5.4: IRP measurements during the addition of DTT and AAPH. Potentials monitored by these two sensors are represented as red circles. White squares represent points in which NQ-NS is fully reduced and insensitive to further reductive changes. Blue squares represent points in which HQ-NS is fully oxidised and, therefore, insensitive to further oxidative changes. Representative spectra for sensors under normoxic conditions, when fully reduced and when fully oxidised, are also shown.

Upon addition of 1 mM DTT, a membrane-permeable, strong reducing agent,[143] reductive changes in the cell were measurable after only 1 min. After 4 mins the potential dropped from -267 to -314 mV (approaching the limit of NQ-NS reductive sensitivity). AAPH (added after 8 mins) induced an oxidative change in the cell, which were quantifiable through monitoring the SERS spectrum of NQ-NS. Oxidative changes were measurable at 13 mins and the cytoplasm became progressively more oxidative, to the extent that NQ-NS was fully oxidised (17 mins, RP = -208 mV), at which point further oxidative changes were monitored using HQ-NS.

The data from HQ-NS showed an increasingly oxidative environment and also an increased rate of oxidative change, which was to be expected, since this potential region was beyond the 'redox buffering' capacity of the GSH/GSSG pair. After 20 mins, HQ-NS was fully oxidised, indicating that the potential was at least 250 mV vs. NHE, and it maintained that status throughout the remainder of the experiment.

5.5 Monitoring Cytoplasmic RP during Apoptosis

Apoptosis is the process of programmed cell death, which occurs in multicellular organisms.[17] Unlike necrosis, apoptosis proceeds in a controlled and regulated fashion and, paradoxically, can prove advantageous for organisms.[17] Typically, during apoptosis, caspase enzymes are activated.[144] Caspases are a family of protease enzymes[145] which can degrade essential cellular components, including structural proteins in the cytoskeleton and nuclear proteins such as DNA repair enzymes.[144] Caspases can also activate enzymes such as DNases which cleave DNA in the nucleus.[146] Compared to healthy dividing cells, apoptotic cells display a number of distinctive morphological differences. Cell shrinkage, rounding, blebbing, as well as nuclear condensation, are all visible in apoptotic cells.[144,147]

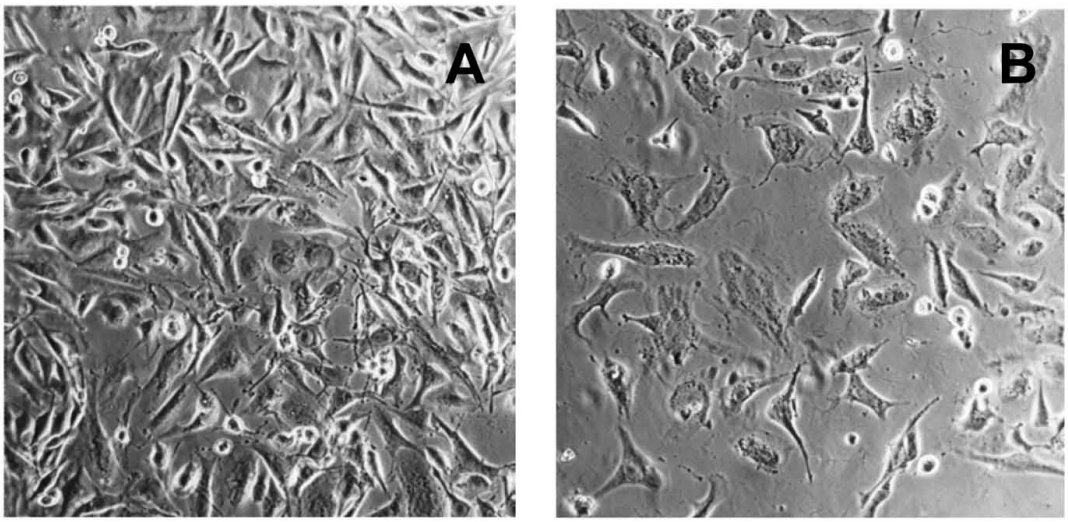

Figure 5.5: Images of **(A)** healthy cells and **(B)** apoptotic cells.[147] Apoptotic cells appear shrunken and more rounded than healthy cells.

In cells, apoptosis can result from a variety of factors, including DNA damage, growth factor depletion, viral infection and excessive ROS generation. Apoptosis can proceed via several, different, mechanisms. It may progress with the involvement of the mitochondria, after being triggered by an internal signal.[148] In this apoptotic pathway, Bcl-2 (a protein located on the surface of the mitochondrial membrane, which guards against apoptosis) is inhibited by Bax (a pro-apoptotic protein).[149] Upon inhibition of Bcl-2's protective effects, the outer mitochondrial membrane is ruptured and cytochrome C leaks into the cytoplasm, where it binds apoptotic protease activating factor-1 (APAF-1) to form apoptosomes.[150] Apoptosomes can go on to activate caspase-9.[151] Caspase-9 can, in turn, activate caspases-3 and -7 resulting in proteolysis and cell death (figure 5.6).[152]

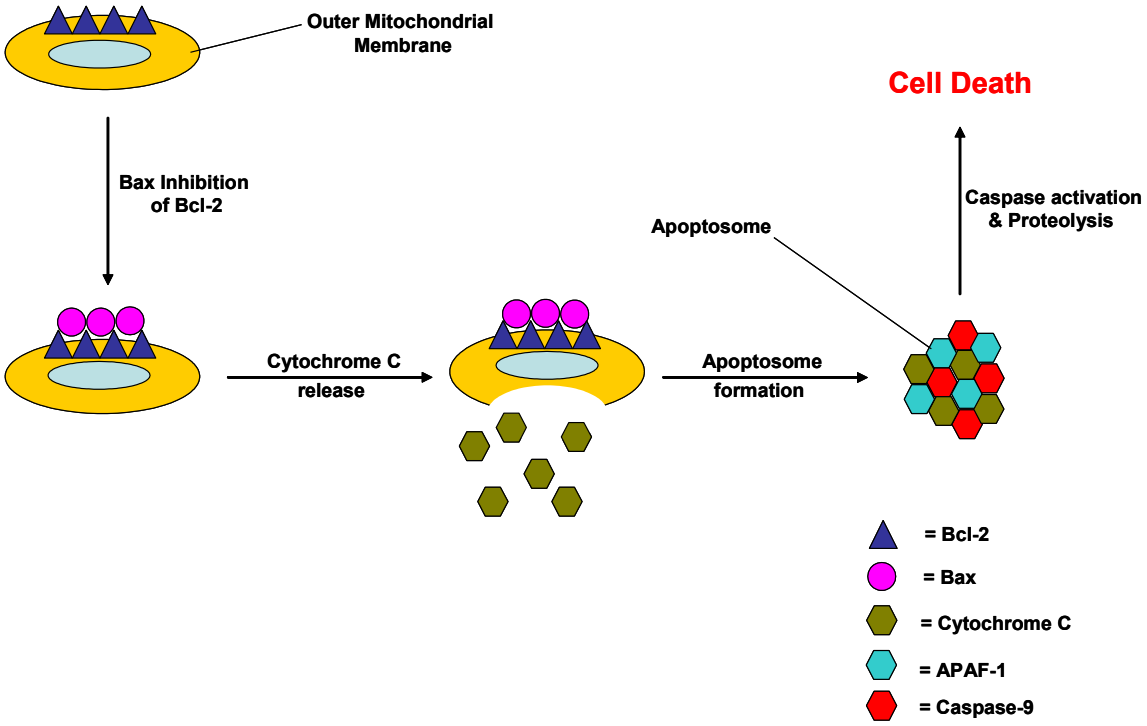

Figure 5.6: Mitochondrial apoptotic pathway. Bcl-2 is inhibited by Bax resulting in cytochrome C release into the cytoplasm. This is followed by apoptosome formation, caspase activation and ultimately cell death.

Apoptosis may also progress with the involvement of death receptors, after being triggered by an external signal. In this apoptotic pathway, the membrane proteins Fas and tumour necrosis factor (TNF)[153,154] receptors bind their complementary death activators (FasL and TNF respectively). This leads to activation of caspase-8, which initiates a signalling cascade of caspase activation, leading to proteolysis and cell death (figure 5.7).[153]

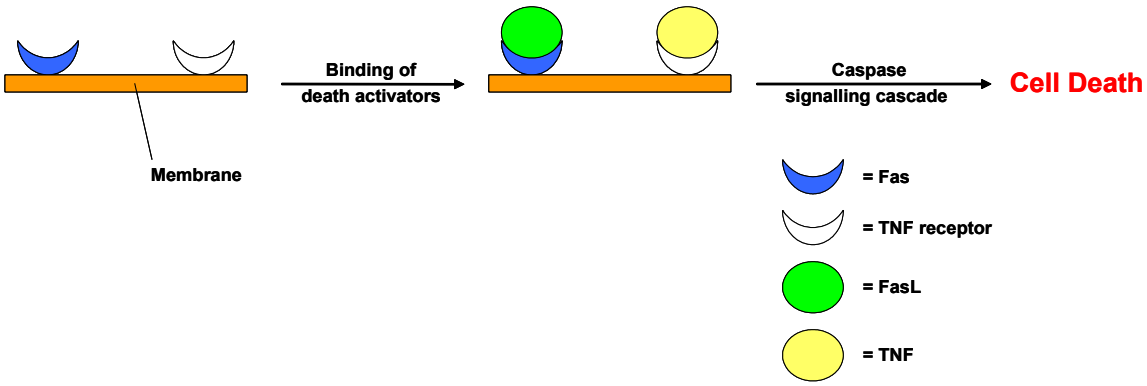

Figure 5.7: Death receptor apoptotic pathway. Fas and TNS bind their complimentary death activators resulting in caspase activation and ultimately cell death.

Not all apoptotic pathways are caspase-dependent. Apoptosis-inducing factor (AIF) is a mitochondrial protein, well known to cause cell death.[155] When the cell receives an appropriate death signal, AIF is released from the mitochondria.[155] AIF then migrates to the nucleus where it can bind to and degrade DNA, ultimately resulting in cell death (figure 5.8).[155]

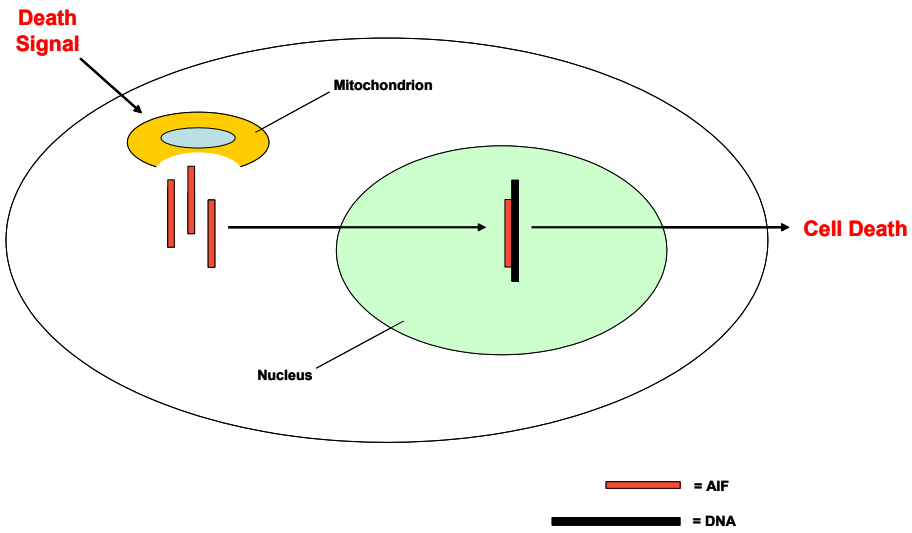

Figure 5.8: AIF apoptotic pathway. AIF is released from the mitochondria and migrates to the nucleus where it degrades DNA and causes cell death.

While the experiments detailed on pages 99-101 represent the utility of HQ-NS and NQ-NS in monitoring superphysiological stresses, NQ-NS has also been used to measure the oxidative changes which occur in cells as a result of apoptosis. Initially, apoptosis was induced with stauosporine, at a concentration of 1 μM. This was determined to be cytotoxic using an established apoptosis assay. Potential measurements were then made inside cells, as apoptosis was induced with H_2O_2 (a physiologically relevant oxidant).

Staurosporine (figure 5.9) is a protein kinase inhibitor[156] and is known to be a potent inducer of apoptosis.[157] The mechanism(s) by which staurosporine induces apoptosis is still a matter of debate in the literature.[131,157] While some reports show that caspase activation is required for staurosporine-induced apoptosis, mechanisms independent of caspase activation have also been proposed.[131]

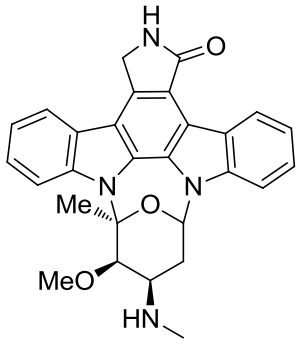

Figure 5.9: Molecular structure of staurosporine.

Figure 5.10 demonstrates that IRP became progressively more oxidative over the 6 h immediately following treatment with staurosporine (1 μM).

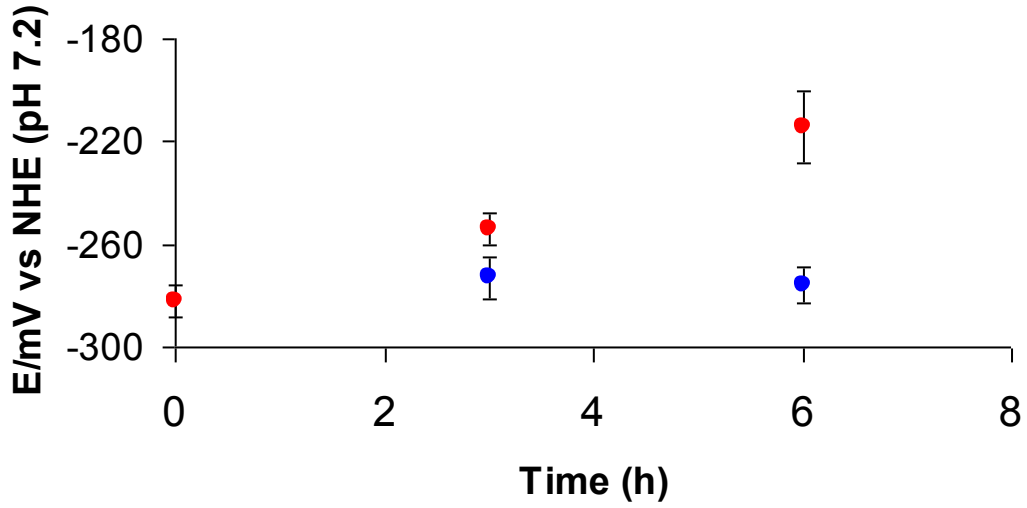

Figure 5.10: Cytosolic potential measurements from cells undergoing staurosporine-induced apoptosis. Blue circles represent potentials measured in untreated cells and red circles represent potentials measured in cells treated with staurosporine. Error bars represent the standard deviation across ten single-cell measurement.

An increase in IRP of 70 mV was observed over the 6 h incubation period. A control population of cells, untreated with staurosporine, did not undergo statistically significant oxidative changes over the same period. These changes are in agreement with measurements of apoptotic potentials, made using assays based on measurement of GSH oxidation.[50,129]

As a signalling molecule, H_2O_2 is important as a trigger in a multitude of cellular pathways. One of those pathways is mitochondrial mediated apoptosis. In order to determine a suitable concentration of H_2O_2 to induce apoptosis in cells, the APOP*ercentage* assay was used once again (figure 5.11). Results shown below, in figure 5.11, were obtained in collaboration with V. Mallikarjun (University of Edinburgh).

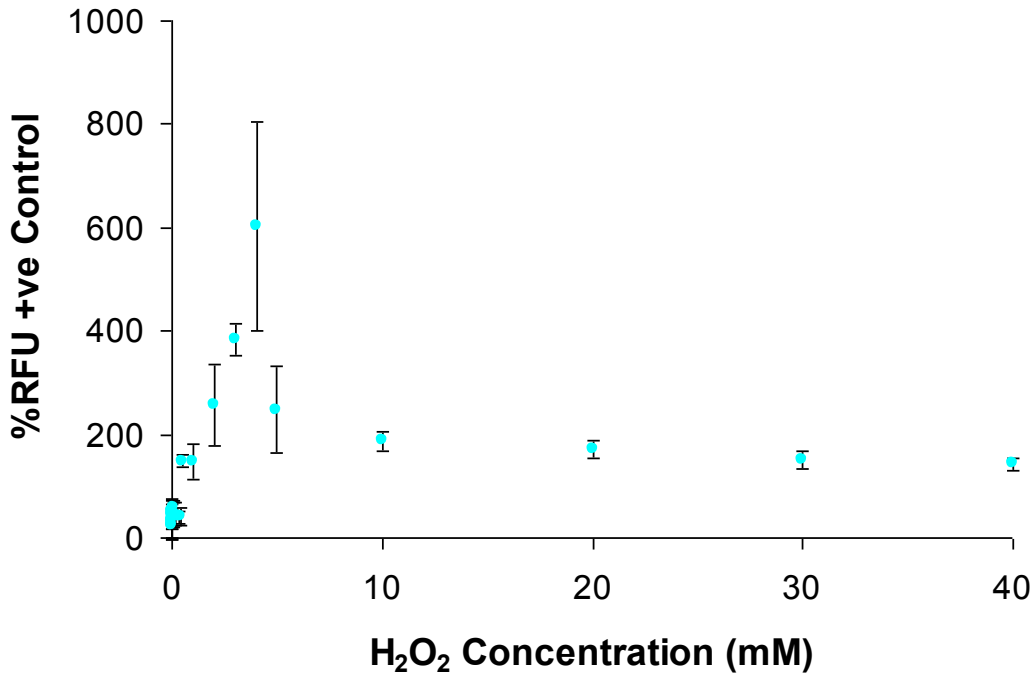

Figure 5.11: Results of the APOP*ercentage* assay for cells incubated with increasing concentrations of H_2O_2. Error bars represent the standard deviation across four populations.

Using the APOPercentage assay, 500 μM was determined to be a high enough concentration of H_2O_2 to induce apoptosis. This concentration was in good agreement with those reported to induce apoptosis in mammalian cells.[158]

Similar to staurosporine-induced apoptosis, oxidative changes were also observed with NQ-NS over a 7 h period (figure 5.13) in cells where apoptosis had been induced with H_2O_2 (500 μM). These findings were further supported by results from cells treated with H_2O_2 (500 μM) and assayed with the APO-One assay (figure 5.13).

The APO-One assay is a fluorescence assay which measures a given sample's caspase-3/7 activity.[159] In this particular assay, Apo-ONE homogeneous caspase-3/7 buffer (which efficiently lyses/permeabilises cultured mammalian cells) is mixed with the caspase-3/7 substrate rhodamine 110, bis-(N-CBZL- aspartyl-L-glutamyl-L-

valyl-L-aspartic acid amide; Z-DEVD-R110) (which exists as a pro-fluorescent substrate prior to the assay).[159] Upon cleavage and removal of the DEVD peptides by caspase-3/7 activity and excitation at 499 nm, the rhodamine 110 leaving group becomes intensely fluorescent, with an emission maximum at 521 nm (figure 5.13).[159]

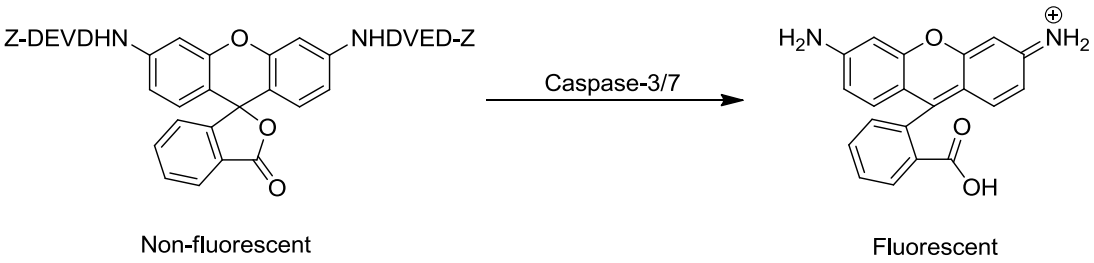

Figure 5.12: Cleavage of the DEVD groups from non-fluorescent caspase substrate Z-DEVD-R110 by caspase-3/7 to yield fluorescent Rhodamine 110. Excitation/emission of Rhodamine 110 is at 499/521 nm.

The amount of fluorescence, measured with a micro-plate reader, is proportional to caspase-3/7 activity.

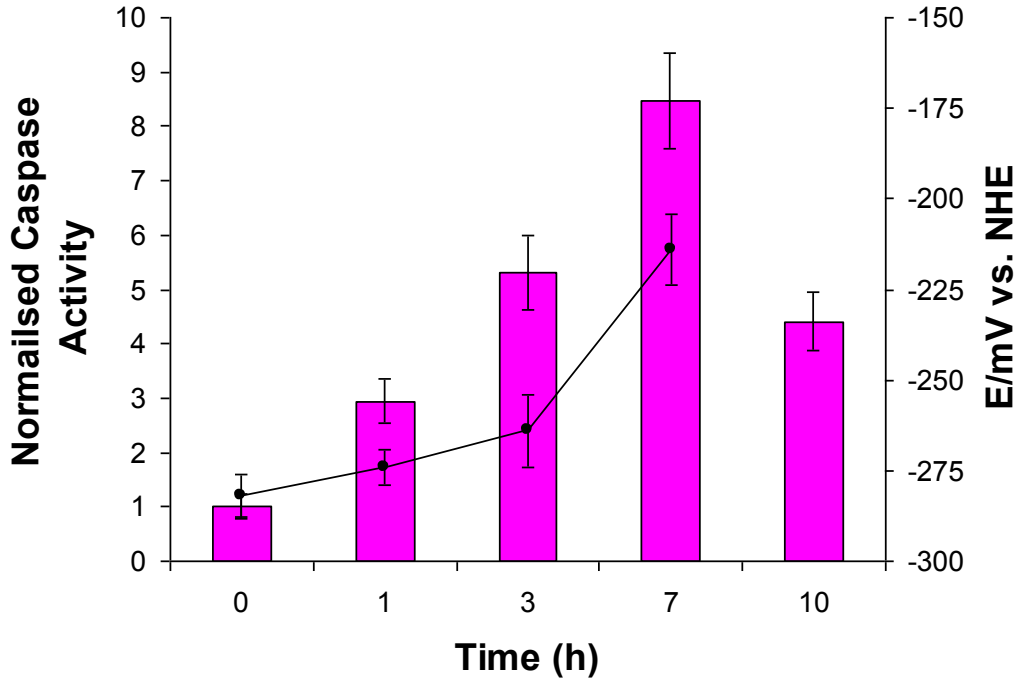

Figure 5.13: Intracellular potential measurements and caspase activity from cells undergoing H_2O_2 induced apoptosis. Diamonds represent potential measurements, and columns represent measurements of caspase 3/7 activity. Error bars in potential measurements represent the standard deviation across 10 single-cell measurements, and error bars in caspase activity represent standard deviation across 10 replicate wells.

Figure 5.13 shows that, with the NQ-NS, an increase in IRP of 68 mV can be observed over the 7 h incubation period. A control population of cells, untreated with H_2O_2, did not undergo statistically significant oxidative changes over the same period. Attempts were made to measure the RP in cells incubated with H_2O_2 after 10 h. At this time, however, the vast majority of cells in the population were either dead or detached from the coverslip on which they were grown.

Figure 5.13 also shows the caspase-3/7 activity of H_2O_2 treated cells compared to untreated cells over a 10 h time course. Caspase-3/7 activity increased over the first 7 h. After 10 h, a drop in caspase activity was noted. This may be due to oxidation of the caspase enzymes. Both caspase-3 and caspase-7 are cysteine proteases and,

therefore, contain cysteine residues in their active sites.[145] As RP increases over time, so does cysteine oxidation in the active sites of caspase-3 and caspase-7, reducing their activity and thus reducing the fluorescence signal observed from the APO-One assay. Results shown in figure 5.13 were obtained in collaboration with V. Mallikarjun (University of Edinburgh).

These measured changes in redox potential are in agreement with measurements of apoptotic potentials made using an assay based on measurement of glutathione oxidation.[129] The data in demonstrate the correlation between redox potential, protease activity, and cellular phenotype and underline the critical interplay between redox potential and physiological processes.

5.6 miR-199a-3p and Oxidative Stress Regulation

miRNAs are short (~22 nucleotide) ribonucleic acid (RNA) sequences.[160] In animals, genes for miRNAs are first transcribed to primary miRNA (pri-miRNA).[160] pri-miRNAs are processed in the nucleus to precursor miRNA (pre-miRNA) by Drosha (a class 2 RNase III enzyme).[160] Pre-miRNAs are then transported into the cytoplasm in a process mediated by exportin-5 (EXP-5).[160] In the cytoplasm, pre mi-RNAs are matured through further processing by Dicer (also an RNase III enzyme). Following maturation, miRNAs are loaded onto Argonaute (AGO) proteins, leading to formation of the effector RNA-induced silencing complexes (RISCs).[160] Figure 5.14 shows a scheme of animal miRNA synthesis.

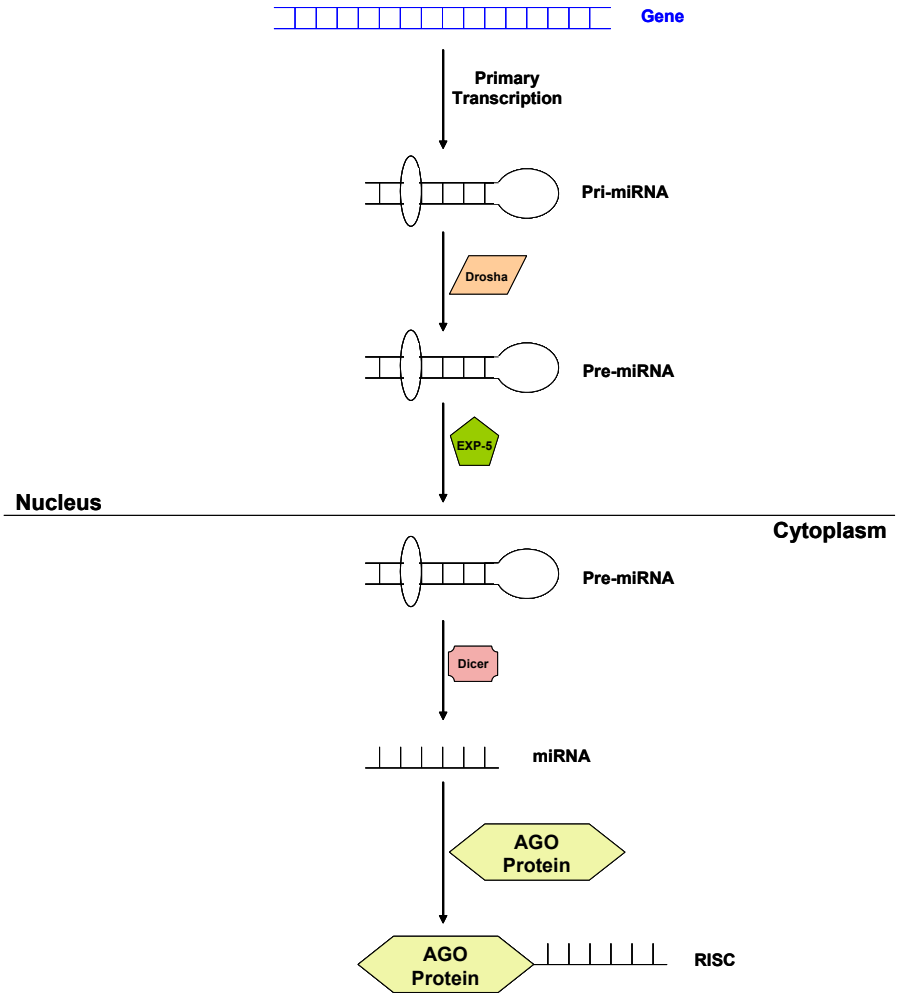

Figure 5.14: miRNA synthesis in animals. Pri-miRNAs are transcribed from genes before being processed to pre-miRNA by Drosha. Pre-miRNAs are then transported to the cytoplasm (by EXP-5) where Dicer helps them to mature before they form effector RISC complexes with AGO proteins.

miRNAs act as post-transcription regulators that bind to specific messenger RNAs (mRNAs), and usually cause suppression of translation, degradation of targets or gene silencing.[160] In animal cells, miRNAs target the non-coding three prime untranslated regions (3'UTR) of a given mRNA. miRNAs need not be fully complementary with their target mRNA, they may target different sites on the same mRNA and may target several different mRNAs (figure 5.15).[160]

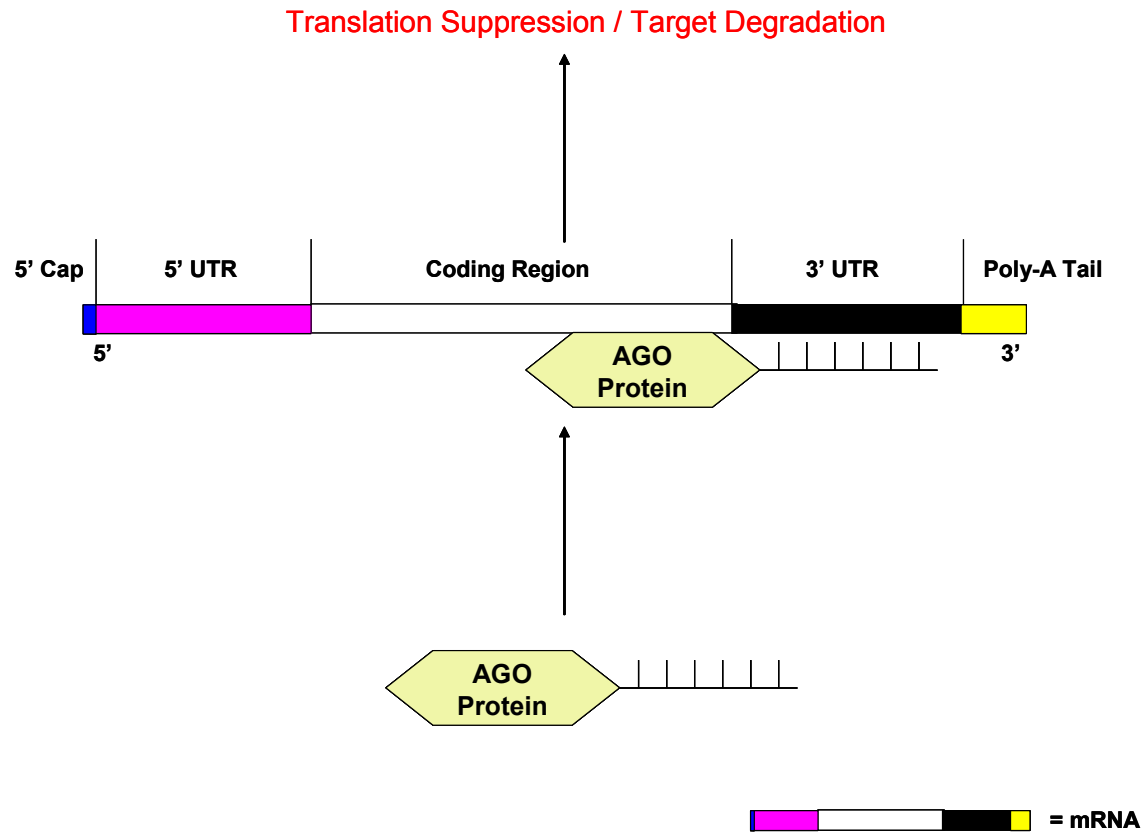

Figure 5.15: miRNA mechanism of action. RISC bind to the 3' UTR of target mRNAs to facilitate their suppression/degradation.

In 2010, Santhakumar *et al* identified that miR-199a-3p plays a regulatory role in the NRF2-mediated oxidative stress pathway.[161] NRF2 is a transcription factor that induces production of antioxidant enzymes including GSTs and NADPH quinone oxidoreductase 1 (Nqo1).[162,163] Since the NRF2 pathway is so closely implicated in the cell's response to oxidative stress, it would be reasonable to speculate that any down-regulation of these genes by miR-199a-3p would be accompanied by oxidative changes.

Using NQ-NS, the cytosolic potential was measured inside cells transfected with miR-199a-3p (figure 5.16).

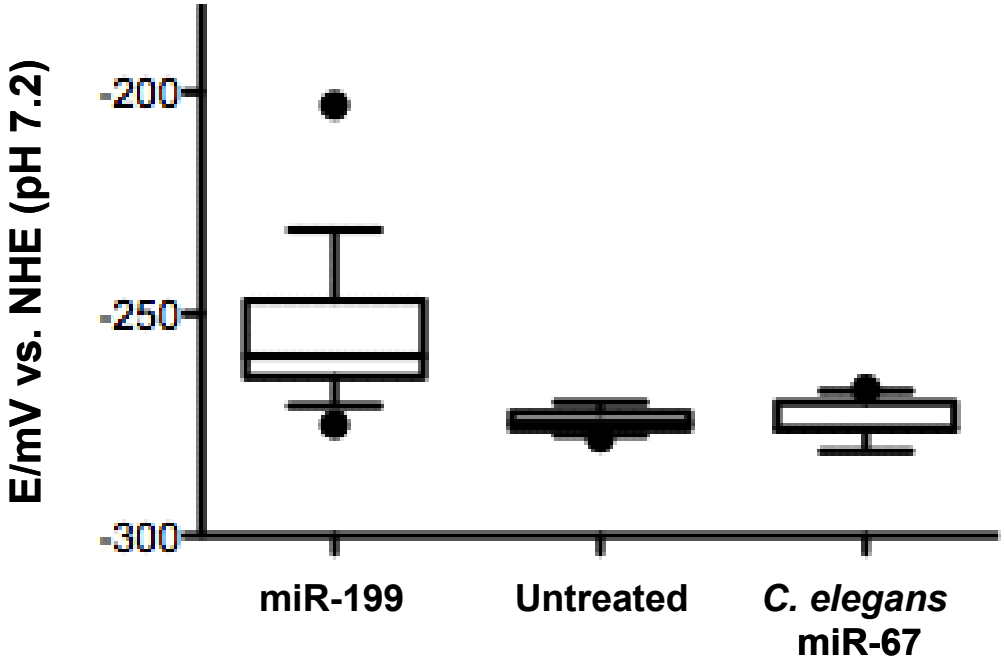

Figure 5.16: Box and whisker plot showing RP measurements of population of cells treated with a miR-199. Negative control cells were treated with non-targeting miR-67 from *C. Elegans*. Error bars represent the standard deviation of 15 measurements.

Figure 5.16 shows that cells treated with miR-199a-3p appeared to have had their cytoplasmic potential increased by 19 mV compared to untreated cells. No statistically significant variation in potential was observed between the untreated cells and those treated with *C. elegans* miR-67 negative mimic (employed as a control miRNA). It can also be seen from figure 5.16 that there was quite a large variation in the potentials measured from cells treated with miR-199a-3p. They ranged from -278 to -204 mV. This large variation may be due to the transfection process being non-uniform, i.e. some cells take up several copies of miRNA mimic whereas other take up none, something that has been observed in our collaborator's miRNA transfection studies. Overall, however, the measurements revealed an oxidative increase in potential indicating that miR-199a-3p may indeed play an important regulatory role in the NRF2-mediated oxidative stress pathway. Results in figure 5.16 were obtained in collaboration with D. Santhakumar (University of Edinburgh).

5.7 Conclusions

While the use of Raman spectroscopy and its variants are well known in cellular imaging, it has never before been used to quantitatively monitor changes in IRP. The nanosensors developed in this work, have made it possible to quantitatively monitor changes in IRP. Reversible changes in IRP were recorded in real-time as cells responded to superphysiological reductive (DTT) and oxidative (AAPH) stimuli. Additionally, changes in IRP were monitored as cells underwent apoptosis (induced by both staurosporine and H_2O_2), as well as during miRNA transcription regulation of the NRF2-mediated oxidative stress pathway. As miRNAs emerge as potential therapeutic agents, their regulation of IRP may be interesting when developing new drug targets for disease states, such as cancer or neurological disorders. These sensors have been demonstrated as a novel and exciting tool with which to monitor IRP, particularly, as has been shown in this chapter, in a biological context.

Chapter 6

Conclusions and Future Work

The overall aims of this work were to develop SERS-active nanosensors capable of:

- Quantitatively and reversibly monitoring changes in IRP with optimal spatiotemporal resolution.
- Demonstrating potential for monitoring RP at a sub-cellular level.
- Monitoring IRP from hypoxia through oxidative stress.

Today, when calculating IRP, most researchers still use Tietze's assay.[47] However, this is far from ideal. Although cheap and simple to use, its requirement for cell lysis excludes its use in IRP monitoring. Furthermore, it cannot account for intracellular, or even intercellular, variation. Instead, it is used to calculate the 'global' potential of thousands of cells in a given population. Even at the cutting edge of redox measurements, using roGFPs, there are significant drawbacks. These sensors, while usable in live monitoring,[12] operate in a narrow potential window which has little scope for extension. As they are fluorescent, they require cells to be excited in the visible region where they absorb and, thus, may be damaged through heating effects.[68]

In this thesis, a novel approach to IRP measurements, offering significant advantages over established techniques and the current state of the art, has been presented. Small molecule sensors have been developed and characterised. Crucially, these sensors displayed changes in their SERS spectra which were dependent on their oxidation state. These changes were quantifiable according to the Nernst equation and optical signatures of the nanosensors were shown to correlate well with those predicted by their half-wave potentials, which were measured independently with CV.

Through TEM, it has been shown that, with the right culture conditions, nanosensors can be selectively delivered to the cytoplasm. Two novel NLS peptides were synthesised and, with them, it was shown that NR could be selectively delivered into cell nuclei. This highlighted the fact that, through tuning of particle size and surface chemistry, considerable scope exists to access other organelles. Monitoring redox balance in compartments, such as the mitochondria or nucleus, would be highly advantageous in gaining an improved understanding of oxidative stress. For example, specific roles have been reported for mitochondrial oxidative stress in apoptosis,[5] while nuclear oxidation can lead to the formation of the mutagenic oxidative DNA adduct 8-OHdeoxyguanosine.[164] Redox imbalances in the ER have also been shown to trigger the unfolded protein response (UPR), a process which has been implicated in several disease states, including cardiovascular disease.[165] Co-functionalisation of NR with a NLS peptide and sensor molecule may offer an opportunity to deliver functional nanosensors to cell nuclei. The NLS, while allowing particles to transfect nuclei, would be expected to have a smaller Raman cross-section than the sensor molecules, which would hopefully allow their spectra to be sufficiently de-convoluted, in order to allow useful information pertaining to the nuclear RP to be obtained.

When developing new bio-sensing modalities, it is important to establish that the act of making a measurement will not unduly perturb the system. To this end, it has been shown, using a variety of assays, that the nanosensors used in this work were non-toxic and, upon their introduction, cells remained viable and did not die. It has also been shown, using established independent assays of oxidative stress, that the nanosensors did not induce oxidative changes. Results of these assays were further supported by spectroscopic measurements revealing that IRP was invariant throughout a period of regular monitoring. The potential values obtained through SERS measurements were in good agreement with previous cytosolic potential measurements conducted under conditions of normal cell physiology.[6,50] While nanomaterials, such as TiO_2 fibres, fullerenes and carbon nanotubes, are known to cause toxicity in cells and animals,[96,97,98] gold nanoparticles have been used extensively in biology and medicine.[103] It is unsurprising, therefore, that the

nanosensors used in this work were similarly non-toxic and did not unduly perturb cellular systems.

In terms of bio-functionality, the nanosensors performed well. They were able to monitor cytoplasmic potentials in a quantitative and reversible way, during both superphysiological stress events and throughout physiological processes. Importantly, they were able to do so in real-time and over a previously unattainable potential range.

While the potential window covered by these sensors is significantly larger than that covered by fluorescent proteins, there is a need for further sensors which cover the region between NQ and HQ (from -200 to -50 mV vs. NHE). The ability to measure and monitor potentials accurately in this region could prove valuable in the study of diseases such as cardiovascular disease, neurodegenerative conditions and chronic inflammation, where oxidative stress is known to ensue.[24,31,32] In this regard, a substantial advantage of using small molecules, rather than proteins, is that their standard potentials can be tuned relatively easily and predictably, using standard synthetic modifications.

Overall, it can be said that the aims of the research have been met. The nanosensors developed here represent a new and noteworthy bio-analytical tool. In conjunction with proteomic studies, the measurements possible with them can be used to gain a fuller understanding of redox biochemistry. They offer users several key advantages over established techniques and current practice. Most notable are their abilities to monitor IRP quantitatively, reversibly and over a wider potential range than ever before, without system perturbation. With the approach detailed here, significant capacity now exists to target nanosenors at organelles, in order to make original RP measurements that can further our understanding of the multitude of electrochemically controlled systems that underpin and have such pivotal roles in cell physiology.

In terms of the future direction of the research, there are many exciting challenges and possibilities to be explored. Below is a list of key issues which should be addressed:

(1) Development of a sensor which monitors IRP from -200 to -50 mV vs. NHE - It should be possible to modify the aromatic ring of NQ-NS with electron withdrawing groups (e.g. NO_2 or CN) using standard organic chemistry. This should make its $E_{1/2}$ and indeed the potential range it can cover more oxidative. By developing a sensor which monitors IRP at a more oxidative poise than NQ-NS it may prove possible to gain a more insightful understanding of the progression of cellular oxidative stress.[6]

(2) Measure/monitor the redox poise of the nucleus - Having successfully delivered NR into the nuclei of cells, the possibility of making a nuclear potential measurement should be explored. Co-functionalisation of NR with NLS peptides and sensor molecules should be attempted. It would be reasonable to expect that Raman signals from the probe molecules would be easily discernable as they would be expected to have greater Raman cross-sections. Concentrations of NLS peptides and probe molecules as well as incubation times in NR functionalisation would need to be thoroughly screened. Cellular delivery conditions and toxicity studies would again need to be carefully investigated for any such experiments.

(3) Investigate the delivery of nanosensors into other organelles - As well as the nucleus, it would be interesting to explore the possibility of delivering nanosensors into other cellular compartments. The mitochondria would be an interesting target as it is here where much of a cell's pivotal redox biochemistry happens.[2,17,] It has recently been shown that cargos with PPh_3 moieties can lead to their entry into the mitochondria.[166] Tagging nanosensors with such functional groups may facilitate their delivery into the mitochondria. The ability to monitor redox changes in the mitochondria may provide a richer understanding of the fundamental redox process on which cells thrive.

(4) Use AQ-NS to measure/monitor redox poise in hypoxic cells - The delivery of AQ-NS into hypoxic cells (such as cancer cells) should be attempted in similar conditions to those outlined in chapter 4. While AQ-NS has also been shown to undergo quantifiable changes in potential, it would be useful to explore its ability to measure and monitor IRP hypoxic cells (such as cancerous cells).[167] If it should prove possible to use the AQ-NS sensor in such circumstances, this would potentially offer fresh and useful insights into tumour biology and its progression.

(5) Development of an integrated vision of apoptotic redox control - By using the sensors developed here in conjunction with the Fourier transform mass spectrometry (FT-MS) facilities available at the University of Edinburgh; it should be possible to correlate changes in IRP during apoptosis with redox-related modifications to proteins involved in the core apoptotic pathway. This would enable the assembly of a comprehensive model of apoptosis where redox modifications of individual proteins could be predicted on the basis of their E^{Θ} and the cell's redox potential.

References

[1] Menon, S.G.; Goswami, P.C. *Oncogene* **2007**, *26*, 1101-9.

[2] Paulsen, C.E.; Carroll, K.S. *ACS Chem. Biol.* **2010**, *5*, 47-62.

[3] Rybicka, J.M.; Balce, D.R.; Khan, M.F.; Krohn, R.M.; Yates, R.M. *Proc. Natl. Acad. Sci. USA* **2010**, *107*, 10496–501.

[4] Liu, J.; *et al*. *Nature* **2009**, *459*, 387-92.

[5] D'Autréaux, B.; Toledano, M.B. *Nature Rev. Mol. Cell. Biol.* **2007**, *8*, 813-24.

[6] Schafer, F.Q.; Buettner, G.R. *Free Radical Biol. Med.* **2001**, *30*, 1191-212.

[7] Monostori, P.; Wittmann, G.; Karg, E.; Túri, S. *J. Chromatogr., B* **2009,** *877*, 3331-46.

[8] Hwang, C.; Sinskey, A.J.; Lodish, H.F. *Science* **1992**, *257*, 1496-502.

[9] Evans, M.D.; Dizdaroglu, M.; Cooke, M.S. *Mutat. Res.* **2004**, *567*, 1-61.

[10] Dooley, C.T.; Dore, T.M.; Hanson, G.T.; Jackson, W.C.; Remington, S.J.; Tsien, R.Y. *J. Biol. Chem.* **2004**, *279*, 22284-93

[11] Hanson, G.T.; Aggeler, R.; Oglesbee, D.; Cannon, M.; Capaldi, R.A.; Tsien, R.Y.; Remington, S.J. *J. Biol. Chem.* **2004**, *279*, 13044-53.

[12] Gutscher, M.; Pauleau, A.L.; Marty, L.; Brach, T.; Wabnitz, G.H.; Samstag, Y.; Meyer, A.J.; Dick, T.P. *Nature Meth.* **2008**, *5*, 553-9.

[13] Austin, C.D.; Wen, X.; Gazzard, L.; Nelson, C.; Scheller, R.H.; Scales, S.J. *Proc. Natl. Acad. Sci. USA* **2005**, *102*, 17987-92.

[14] Fisher, A.C. *Electrode Dynamics*, Oxford University Press, 1996.

[15] Szabo, C.; Ischiropoulos, H.; Radi, R. *Nat. Rev. Drug Discovery* **2007**, *6*, 662-80.

[16] Giorgio, M.; Trinei, M.; Migliaccio, E.; Pelicci, P.G. *Nature Rev. Mol. Cell. Biol.* **2007**, *8*, 722-8.

[17] Campbell, N.A.; Reece, J.B. *Biology*, 6th ed.; Benjamin Cummings, 2002.

[18] Chelikani, P.; Fita, I.; Loewen, P.C. *Cell. Mol. Life Sci.* **2004**, *61*, 192-208.

[19] Thomas, C.; Mackey, N.M.; Diaz, A.A.; Cox, D. *Redox Report* **2009**, *14*, 102-8.

[20] Reiter, R.J.; Melchiorri, D.; Sewerynek, E.; Poeggeler, B.; Barlow-Walden, L.; Chuang, J.; Ortiz, G.G.; Acuña-Castroviejo, D. *J. Pineal Res.* **1995**, *78*, 1-11.

[21] Daff, S. *Nitric Oxide* **2010**, *23*, 1-11.

[22] Pompella, A.; Visvikis, A.; Paolicchi, A.; De Tata, V.; Casini, A.F. *Biochem. Pharmacol.* **2003**, *66*, 1499-503.

[23] Dessy, C.; Ferron, O. *Curr. Med. Chem.: Anti-Inflammatory Anti-Allergy Agents* **2004**, *3*, 207-16.

[24] Nordberg, J.; Arnér, E.S.J. *Free Radical Biol. Med.* **2001**, *31*, 1287-312.

[25] http://www.sigmaaldrich.com/life-science/cell-biology/learning-center/pathway-slides-and/oxidative-stress.html [Accessed September 2011].

[26] Segura-Aguilar, J.; Metodiewa, D.; Welch, C.J. *Biochim. Biophys. Acta* **1998**, *1381*, 1-6.

[27] Wiseman, H.; Halliwell, B. *Biochem. J.* **1996**, *313*, 17-29.

[28] http://www.cyberlipid.org/perox/oxid0002.htm [Accessed September 2011].

[29] Berlett, B. S.; Steadman, E. R. *J. Biol. Chem.* **1997**, *272*, 20313-6.

[30] Halliwell, B. *Biochem. J.* **2007**, *401*, 1-11.

[31] Parthasarathy, S.; Khan-Merchant, N.; Penumetcha, M.; Santanam, N. *J. Nucl. Cardiol.* **2001**, *8*, 379-89.

[32] Barnham, K.J.; Masters, C.L.; Bush, A.I. *Nat. Rev. Drug Discovery* **2004**, *3*, 205-14.

[33] Sheehan, D.; Meade, G.; Foley, V.M.; Dowd, C.A. *Biochem. J.* **2001**, *360*, 1-16.

[34] http://www.epc.bio.dtu.dk/Forskning.aspx [Accessed September 2011]

[35] Hoshino, T.; *et al. Am. J. Respir. Crit. Care Med.* **2003**, *168*, 1075-83.

[36] Rancourt, R.C.; Lee, R.L.; O'Neill, H.; Accurso, F.J.; White, C.W. *Free Radical Biol. Med.* **2007**, *42*, 1441-53.

[37] Bloomfield, K.L.; Osborne, S.A.; Kennedy, D.D.; Clarke, F.M.; Tonissen, K.F. *Gene* **2003**, *319*, 107-16.

[38] Inoguchi, T.; *et al. J. Am. Soc. Nephrol.* **2003**, *14*, 227-32.

[39] Hayes, J.D.; *et al. Free Radic. Res.* **1999**, *31*, 273-300.

[40] McCord, J.M.; Fridovich, I. *Free Radical Biol. Med.* **1988**, *5*, 363-9.

[41] Valko, M.; Morris, H.; Cronin, M.T.D. *Curr. Med. Chem.* **2005**, *12*, 1161-208.

[42] Dalton, T.; Shertzer, H. G.; Puga, A. *Annu. Rev. Pharmacol. Toxicol.* **1999**, *39*, 67-101.

[43] Griendling, K. K. *et al*. *Arterioscler Thromb Vasc Biol*. **2000**, *20*, 2175-83.

[44] Dunn, L. L.; Rahmanto, Y.S.; Richardson, D. R. *Trends Cell Biol.* **2006**, *17*, 93-100.

[45] Finney, L. A.; O'Halloran, T. V. *Science*, **2003**, *300*, 931-6.

[46] Thompson, K. H.; Orvig, C. *Science*, **2003**, *300*, 936-8.

[47] Tietze, F. *Anal. Biochem.* **1969**, *27*, 502-22.

[48] Shaik, I.H.; Mehvar, R. *Anal. Bioanal. Chem.* **2006**, *385*, 105-13.

[49] Wiseman, D.A.; Sharma, S.; Black, S.M. *Biometals* **2010**, *23*, 19-30.

[50] Kemp, M.; Go, Y-M.; Jones, D.P. *Free Radical Biology & Medicine* **2008**, *44*, 921-37.

[51] Smith, N.C.; Dunnett, M.; Mills, P.C. *J. Chromatogr., B* **1995**, *673*, 35-41.

[52] Kundu, K.; Knight, S.F.; Willett, N.; Lee, S.; Taylor, W.R.; Murthy, N. *Angew. Che. Int. Ed.* **2009**, *48*, 299-303.

[53] Keese, M.A.; Saffrich, R.; Dandekar, T.; Becker, K.; Schirmer, R.H. *FEBS Lett.* **1999**, *447*, 135-8.

[54] Shimomura, O.; Johnson, F.H.; Saiga, Y. *J. Cell. Comp. Physiol.* **1962**, *59*, 223-9.

[55] http://www.nobelprize.org/nobel_prizes/chemistry/laureates/2008 [Accessed September 2011].

[56] Sauer, M.; Hofkens, J.; Enderlein, J. *Handbook of Fluorescence Spectroscopy and Imaging: From Ensemble to Single Molecules*, 1st ed.; Wiley, 2011.

[57] Dixit, R.; Cyr, R. *Plant J.* **2003**, *36*, 280-90.

[58] Cohen B.E. *Nature* **2010,** *467*, 407-8.

[59] Le Ru, E.C.; Etchegoin, P.G. *Principles of Surface-Enhanced Raman Spectroscopy and Related Plasmonic Effects*, Elsevier, 2009.

[60] Raman, C.V.; Krishnan, K.S. *Nature* **1928**, *121*, 501-2.

[61] Smith, E.; Dent, G. *Modern Raman Spectroscopy: A Practical Approach*, Wiley, 2005.

[62] Fleischman, M.; Hendra, P.J.; McQuillan, A.J. *Chem. Phys. Lett.* **1974**, *26*, 163-6.

[63] Nie, S.; Emory, S.R. *Science* **1997**, *275*, 1102-5.

[64] Moskovits, M. *J. Raman Spectrosc.* **2005**, *36*, 485-96.

[65] Faulds, K.; Barbagallo, R.P.; Keer, J.T.; Smith, W.E.; Graham, D. *Analyst* **2004**, *129*, 567-8.

[66] Cao, Y.C.; Jin, R.; Mirkin, C.A. *Science* **2002**, *297*, 1536-9.

[67] Brinson, B.E.; Lassiter, J.B.; Levin, C.S.; Bardhan, R.; Mirin, N.; Halas, N.J. *Langmuir* **2008**, *24*, 14166-71.

[68] Hirsch, L.R.; *et al. Proc. Natl. Acad. Sci. USA* **2003**, *100*, 13549-54.

[69] http://bme240.eng.uci.edu/students/06s/amazhar/properties.htm [Accessed September 2011].

[70] Bishnoi, S.W.; Rozell, C.J.; Levin, C.S.; Gheith, M.K.; Johnson, B.R.; Johnson, D.H.; Halas, N.J. *Nano Lett.* **2006**, *6*, 1687-92.

[71] Ochsenkühn, M.A.; Jess, P.R.T.; Stoquert, H.; Dholakia, K.; Campbell, C.J. *ACS Nano* **2009**, *3*, 3613-21.

[72] Nagata, M.; Kondo, M.; Suemori, Y; Ochiai, T.; Dewa, T.; Ohtsuka, T.; Nango, M. *Colloids Surf., B* **2008**, *64*, 16-21.

[73] Monks, T.J.; Highet, R.J.; Chu, P.S.; Lau, S.S. *Mol. Pharmacol.* **1988**, *34*, 15-22.

[74] Schön, P.; Degefa, T.H.; Asaftei, S.; Meyer, W.; Walder, L. *J. Am. Chem. Soc.* **2005**, *127*, 11486-96.

[75] Galow, T.H.; Rodrigo, J.; Cleary, K.; Cooke, G.; Rotello, V.M. *J. Org. Chem.* **1999**, *64*, 3745-6.

[76] http://www.chempep.com/ChemPep-Fmoc-Solid-Phase-Peptide-Synthesis.htm [Accessed September 2011].

[77] http://www.piercenet.com/browse.cfm?fldID=02020101 [Accessed September 2011].

[78] http://www.biocolor.co.uk/manuals/apopercentage.pdf [Accessed September 2011]

[79] http://www.promega.com/~/media/Files/Resources/Protocols/Technical%20Bulletins/0/ApoONE%20Homogeneous%20Caspase%203%207%20Assay%20Protocol.ashx [Accessed September 2011]

[80] Becke, A.D. *J. Chem. Phys.* **1993**, *98*, 5648-52.

[81] Lee, C.; Yang, W.; Parr, R.G. *Phys. Rev. B* **1988**, *37*, 785-9

[82] Hay, P.J.; Wadt, W.R. *J. Chem. Phys.* **1985**, *82*, 270-83.

[83] Hay, P.J., Wadt, W.R. *J. Chem. Phys.* **1985**, *82*, 299-310.

[84] Wadt, W.R.; Hay, P.J. *J. Chem. Phys.* **1985**, *82*, 284-98.

[85] Dunning, T.H.; Hay, P.J. *Modern Theoretical Chemistry*, Ed. Schaefer, H.F. Vol. 3, Plenum, New York, 1976.

[86] Quan, M.; Sanchez, D.; Wasylkiw, M.F.; Smith, D.K. *J. Am. Chem. Soc.* **2007**, *129*, 12847–56.

[87] Ulmann, A. *Chem. Rev.* **1996**, *96*, 1533-54.

[88] Clayden, J.; Greeves, N.; Warren, S.; Wothers, P. *Organic Chemistry*, Oxford University Press, 2001

[89] de Brabander, M.; Nuydens, R.; Ishihara, A.; Holifield, B.; Jacobson, K.; Geerts, H. *J. Cell Biol.* **1991**, *112*, 111-24.

[90] http://www.nanoscience.com/education/afm.html [Accessed September 2011]

[91] *Proceedings of the 2nd International Conference on Nanotechnology: Fundamentals and Applications*, International AEST, Ottawa, 2011.

[92] http://www.electronicsandyou.com/electronics-images/electronic.jpg [Accessed September 2011]

[93] http://bellafloria.files.wordpress.com/2010/06/istock_sunscreen-small1.jpg [Accessed September 2011]

[94] http://whyy.org/cms/radiotimes/files/2010/01/nanoparticles3.jpg [Accessed September 2011]

[95] http://www.listen2yourgut.com/blog/blog/blogimages/2010/04/nano-silversocks.jpg [Accessed September 2011]

[96] Oberdörster, G.; Oberdörster, E.; Oberdörster, J. *Environ. Health Perspect.* **2005**, *113*, 823-39.

[97] Xia, T.; Li, N.; Nel, A.E. *Annu. Rev. Public Health* **2009**, *30*, 137-50.

[98] Donaldson, K.; Murphy, F.A.; Duffin, R.A.; Poland, C.A. *Part. Fibre Toxicol.* **2010**, *7*, 1-17.

[99] Dostert, C.; Pétrilli, V.; Van Bruggen, R.; Steele, C.; Mossman, B.T.; Tschopp, J. *Science* **2008**, *320*, 674-7.

[100] Dahlgren, C.; Karlsson, A. *J. Immunol. Methods* **1999**, *232*, 3-14.

[101] Pachón, L.D.; Rothenberg, G. *Appl. Organomet. Chem.***2008**, *22*, 288-99.

[102] Boyer, C.; Whittaker, M.R.; Bulmus, V.; Lui, J.; Davis, T.P. *NPG Asia Mater.* **2010**, *2*, 23-30.

[103] Giljohann, D.A.; Seferos, D.S.; Daniel, W.L.; Massich, M.D.; Patel, P.C.; Mirkin, C.A. *Angew. Chem. Int. Ed.* **2010**, *49*, 3280-94.

[104] http://www.nobelprize.org/educational/physics/microscopes/tem/index.html [Accessed September 2011]

[105] Lodish, H.; Berk, A.; Zipursky, S.L.; Matsudaira, P.; Baltimore, B.; Darnell, J. *Molecular Cell Biology*, 4th Ed., W.H. Freeman, 2000.

[106] Mokari, T.; Sztrum, C.G.; Salant, A.; Rabani, E.; Banin, U. *Nat. Mater.* **2005**, *4*, 855-63.

[107] Franz, M.; Wipf, P. *Environ. Mol. Mutagen* **2010**, *51*, 462-75.

[108] Oyelere, A.K.; Chen, P.C.; Huang, X.; El-Sayed, I.H.; El-Sayed, M.A. *Bioconjug. Chem.* **2007**, *18*, 1490-97.

[109] Xie, W.; Wang, L.; Zhang, Y.; Su, L.; Shen, A.; Tan, J.; Hu, J. *Bioconjug. Chem.* **2009**, *20*, 768-73.

[110] Kalderon, D.; Roberts, B.L.; Richardson, W.D.; Smith, A.E. *Cell* **1984**, *39*, 499-509.

[111] Dingwall, C.; Robbins, J.; Dilworth, S.M.; Roberts, B.; Richardson, W.D. *J. Cell Biol.* **1988**, *107*, 841-9.

[112] Lee, B.J.; Cansizoglu, A.E.; Süel, K.E.; Louis, T.H.; Zhang, Z.; Chook, Y.M. *Cell* **2006**, *126*, 543-58.

[113] Newmeyer, D.D.; Forbes, D.J. *Cell* **1988**, *52*, 641-53.

[114] Kubitscheck, U.; Wedekind, P.; Zeidler, O.; Grote, M.; Peters, R. *Biophys. J.* **1996**, *70*, 2067-77.

[115] Alvarez-Puebla, R.A.; Ross, D.J.; Nazri, G.A.; Aroca, R.F. *Langmuir* **2005**, *21*, 10504-8.

[116] http://www.nanopartz.com/Nanorodz.htm [Accessed September 2011]

[117] Chan, W.C.; White, P.D. *Fmoc Solid Phase Peptide Synthesis: A Practical Approach*, Oxford University Press, 2000.

[118] Nghiem, T.H.L.; *et al*., *Adv. Nat. Sci.: Nanosci. Nanotechnol.* **2010**, *1*, 025009 (5pp).

[119] Suga, K.; Bradley, M.; Rusling, J.F. *Langmuir* **1993**, *9*, 3063-6.

[120] Stewart, S.; Fredericks, P.M. *Spectrochim. Acta, Part A* **1999**, *55*, 1641-60.

[121] Aliaga, A.E.; *et al. Spectrochim. Acta, Part A* **2010**, *76*, 458-63.

[122] http://probes.invitrogen.com/media/pis/mp21486.pdf [Accessed September 2011]

[123] Shiraishi, T.; Nielsen, P. E. *Nat. Protoc.* **2006**, *1*, 633-6.

[124] Esposti, M.D. *Methods* **2002**, *26*, 335-40.

[125] Girard-Lalancette, K.; Pichette, A.; Legault, J. *Food Chem.* **2009**, *115*, 720-6.

[126] http://search.cosmobio.co.jp/cosmo_search_p/search_gate2/docs/CBL_/STA342.20090820.pdf [Accessed September 2011]

[127] Martín, M.A.; Ramos, S.; Mateos, R.; Izquierdo-Pulido, M.; Bravo, L.; Goya, L. *Phytother. Res.* **2010**, *24*, 503-9.

[128] Song, W.; Zhang, J.; Guo, J.; Zhang, J.; Ding, F.; Li, L.; Sun, Z. *Toxicol. Lett.* **2010**, *199*, 389-97.

[129] Cai, J.; Jones, D.P. *J. Biol. Chem.* **1998**, *273*, 11401-4.

[130] http://www.biocolor.co.uk/manuals/apopercentage.pdf [Accessed September 2011]

[131] Belmokhtar, C.A.; Hillion, J.; Ségal-Bendirdjian, E. *Oncogene* **2001**, *20*, 3354-62.

[132] Mosmann, T. *J. Immunol. Methods* **1983**, *65*, 55-63.

[133] http://www.caymanchem.com/pdfs/10009365.pdf [Accessed September 2011]

[134] Uzunbajakava, N.; A. Lenferink, A.; Kraan, Y.; Volokhina, E.; Vrensen, G.; Greve, J.; Otto, C. *Biophys. J.* **2003**, *84*, 3968-81.

[135] Draux, F.; Gobinet, C.; Sulé-Suso, J.; Manfait, M.; Pierre Jeannesson, P.; Sockalingum, G. D. *Analyst* **2011**, *136*, 2718-25.

[136] Pezacki, J. P.; Blake, J. A.; Danielson, D. C.; Kennedy, D.C.; Lyn, R. K. Singaravelu, R. *Nat. Chem. Biol.* **2011**, *7*, 137-45.

[137] Xie, W.;Su, L.; Shen, A.; Materny, A.; Hu, J. *J. Raman Spectrosc.* **2010**, *42*, 1248-54.

[138] Jarvis, R.; Goodacre, R. *Chem.Soc.Rev.* **2008**, *37*, 931-6.

[139] Vo-Dinh, T.; Wang, H.N.; Scaffidi, J. . *Biophotonics* **2010**, *3*, 89-102.

[140] Shanmukh, S.; Jones, L.; Driskell, J.; Zhao, Y.; Dluhy, R.; Tripp, R.A. *Nano Lett.* **2006**, *6*, 2630-6.

[141] Cui, Y.; Kim, D.; Park, S.; Yoon, J.; Kim, S.; Qwon, S.; Park, K. *Chem. Phys. Lipids* **2004**, *129*, 43-52.

[142] Niki, E. *Methods Enzymol.* **1990**, *186*, 100-8.

[143] Cleland, W.W. *Biochemistry* **1964**, *3*, 480- 2.

[144] Cohen, G.M. *Biochem. J.* **1997**, *326*, 1-16.

[145] Alnemri, E.S.; Livingston, D.J.; Nicholson, D.W.; Salvesen, G.; Thornberry, N.A.; Wong, W.W.; Yuan, J. *Cell*, **1996**, *87*, 171.

[146] Counis, M.F.; Torriglia, A. *Biochem. Cell Biol.* **2000**, *4*, 405-14.

[147] Frahm, S.; Kurtz, A.; Kluwe, L.; Farassati, F.; Friedrich, R.E.; Mautner, V.F. *Cancer Cell Int.* **2004**, *4*, 1-11.

[148] Green, D.R.; Reed, J.C. *Science* **1998**, *281*, 1309-12.

[149] Zeitlin, B.D.; Zeitlin, I.J.; Nör, J.E. *J.C.O.* **2008**, *26*, 4180-8.

[150] Kim, H.; Du, F.; Fang, M.; Wang, X. *Proc. Natl. Acad. Sci. USA* **2005**, *102*, 17545-50.

[151] Pop, C.; Timmer, J.; Sperandio, S.; Salvessen, G.S. *Mol. Cell* **2006**, *2*, 269-75.

[152] http://www.sgul.ac.uk/depts/immunology/~dash/apoptosis/caspases.html [Accessed September 2011]

[153] Wajant, H. *Science*, **2002**, *296*, 1635-6.

[154] Chen, G.; Goeddel, D.V. *Science*, **2002**, *296*, 1634-5.

[155] Ye, H.; *et al. Nat. Struct. Biol.* **2002**, *9*, 680-4.

[156] Gani, O.A.B.S.M.; Engh, R.A. *Nat. Prod. Rep.* **2010**, *27*, 489-98.

[157] Wan, X.; Yokoyama, Y.; Shinohara, A.; Takahashi, Y.; Tamaya, T. *Cell Death Differ.* **2002**, *9*, 414-20.

[158] Nakajima, Y.; Aoshiba, K.; Yasui, S.; Magai, A. *Life Sciences* **1999**, *64*, 2489-96.

[159] http://www.promega.com/~/media/Files/Resources/Protocols/Technical%20Bulletins/0/ApoONE%20Homogeneous%20Caspase%203%207%20Assay%20Protocol.ashx [Accessed September 2011]

[160] Wahid F.; Shehzad, A.; Khan, T.; Kim, Y.Y. *Biochim. Biophys. Acta* **2010**, *1803*, 1231-43.

[161] Santhakumar, D.; *et al. Proc. Natl. Acad. Sci. USA* **2010**, *107*, 13830-5.

[162] Hayes, J.B.; Chanas, S.A.; Henderson, C.J.; McMahon, M.; Sun, C.; Moffat, G.J.; Wolf, C.R.; Yamamoto, M. *Biochem. Soc. Trans.* **2000**, *28*, 33-41.

[163] Venugopal, R.; Jaiswal, A.K. *Proc. Natl. Acad. Sci. USA* **1996**, *93*, 14960-5.

[164] Gordillo, G.; Fang, H.; Park, H.; Roy, S. *Antioxidant Redox Signal.* **2010**, *12*, 933-43.

[165] Kezhong Zhang, K.; Kaufman, R.J. *Nature* **2008**, *454*, 455–62.

[166] Yusop, R. M.; Unciti-Broceta, A.; Johansson, E. M. V.; Sanchez-Martin, R. M.; Bradley, M. *Nat. Chem*. **2011**, *3*, 239-43.

[167] Wilson, W.R.; Hay, M.P. *Nat. Rev. Cancer* **2011**, *11*, 393-410.

Appendices

Appendix 1 CV Analyses

E_{Red} (mV)	E_{Ox} (mV)	i_{Red} (µA)	i_{Ox} (µA)	C_{Red} (µC)	C_{Ox} (µC)	i_{Red}/i_{Ox}	C_{Red}/C_{Ox}
-344	-285	0.216	0.208	0.027	0.024	1.038	1

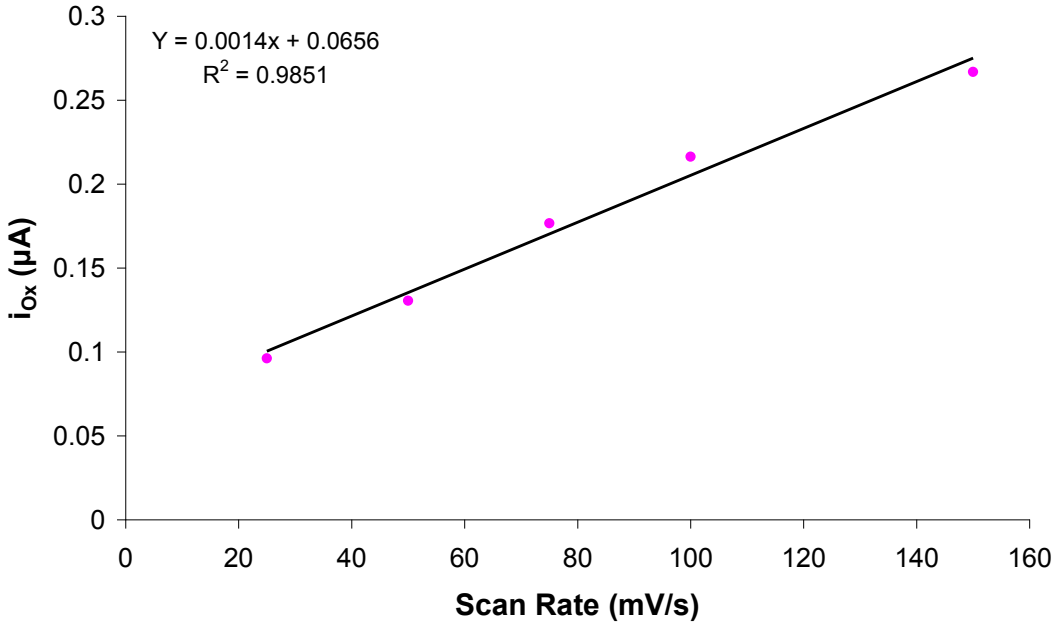

Appendix 1a: AQ CV analyses including i_{Red}/ i_{Ox} and C_{Red}/ C_{Ox} ratio and plot of i_{Ox} vs. scan rate.

E_{Red} (mV)	E_{Ox} (mV)	i_{Red} (µA)	i_{Ox} (µA)	C_{Red} (µC)	C_{Ox} (µC)	i_{Red}/ i_{Ox}	C_{Red}/ C_{Ox}
-313	-253	0.615	0.598	0.035	0.035	1.028	1

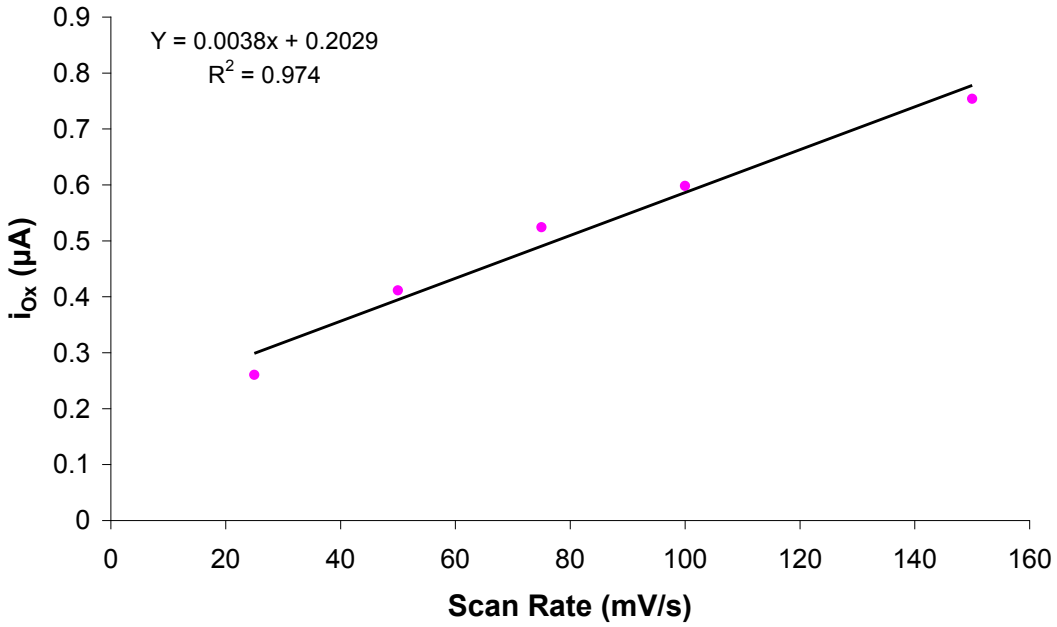

Appendix 1b: NQ CV analyses including i_{Red}/ i_{Ox} and C_{Red}/ C_{Ox} ratio and plot of i_{Ox} vs. scan rate.

E_{Red} (mV)	E_{Ox} (mV)	i_{Red} (µA)	i_{Ox} (µA)	C_{Red} (µC)	C_{Ox} (µC)	i_{Red}/ i_{Ox}	C_{Red}/ C_{Ox}
67	194	0.719	0.680	0.138	0.133	1.057	1.038

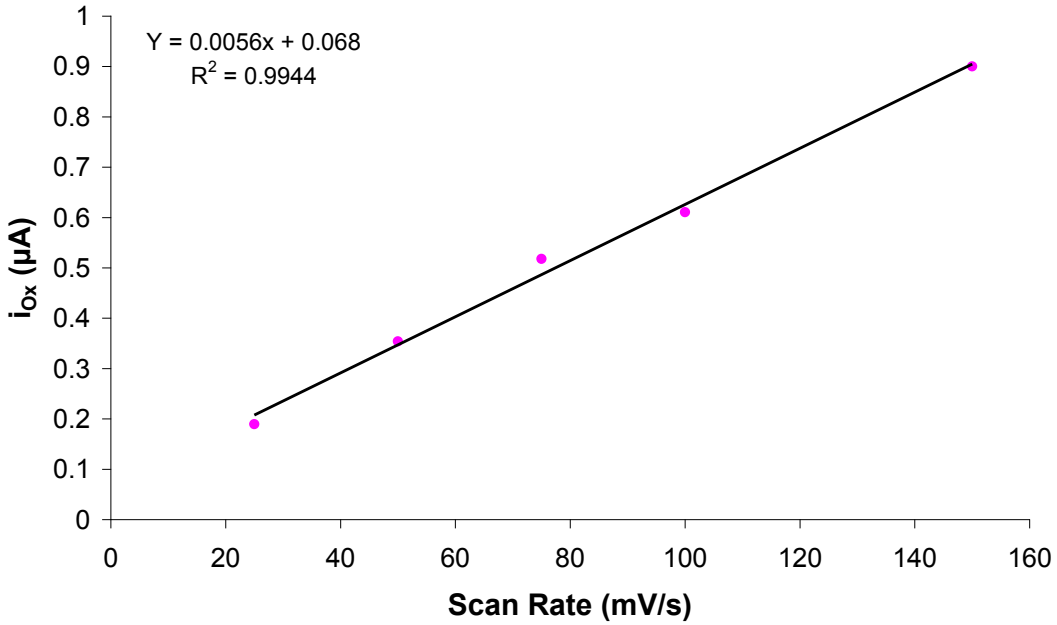

Appendix 1c: HQ CV analyses including i_{Red}/ i_{Ox} and C_{Red}/ C_{Ox} ratio and plot of i_{Ox} vs. scan rate.

E_{Red} (mV)	E_{Ox} (mV)	i_{Red} (µA)	i_{Ox} (µA)	C_{Red} (µC)	C_{Ox} (µC)	i_{Red}/ i_{Ox}	C_{Red}/ C_{Ox}
427	489	1.294	1.330	0.124	0.130	0.973	0.954

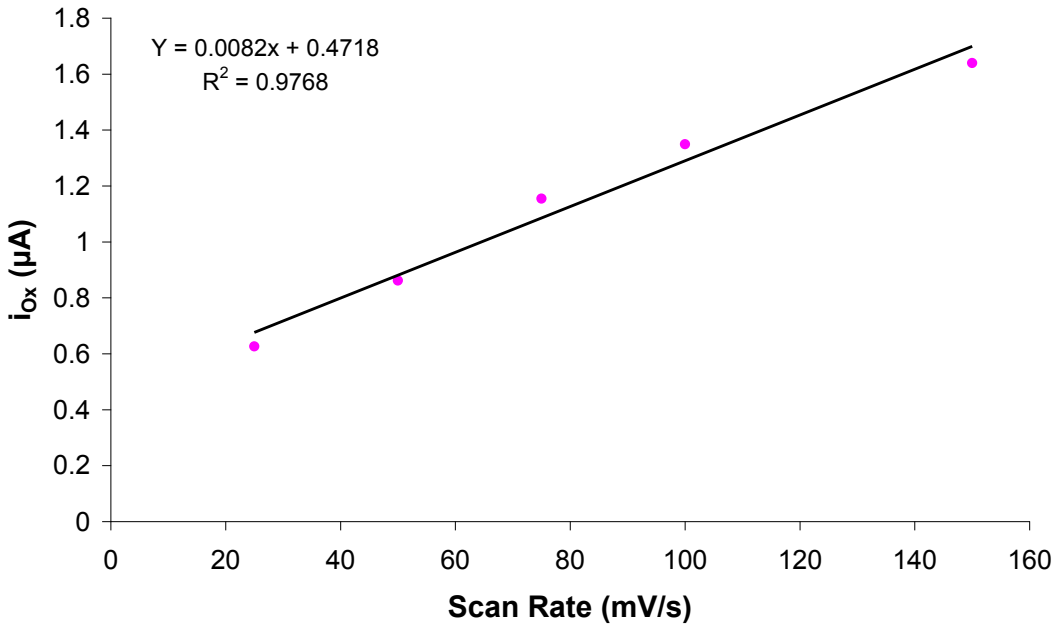

Appendix 1d: FCBX CV analyses including i_{Red}/ i_{Ox} and C_{Red}/ C_{Ox} ratio and plot of i_{Ox} vs. scan rate.

Appendix 2 UV-vis spectra of RAM functionalised NS

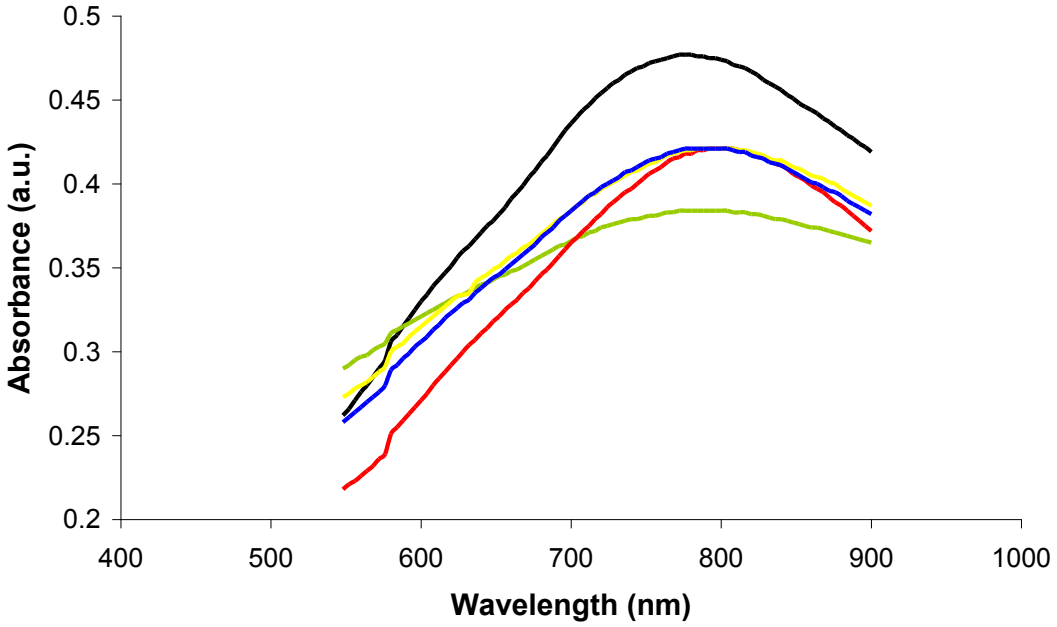

Appendix 2: UV-vis spectra of RAM functionalised NS. Bare NS (black line), NQ-NS (green line), HQ-NS (red line), AQ-NS (yellow line) and FCBX-NS (blue line).

Appendix 3 Nanosensor TEM Gallery

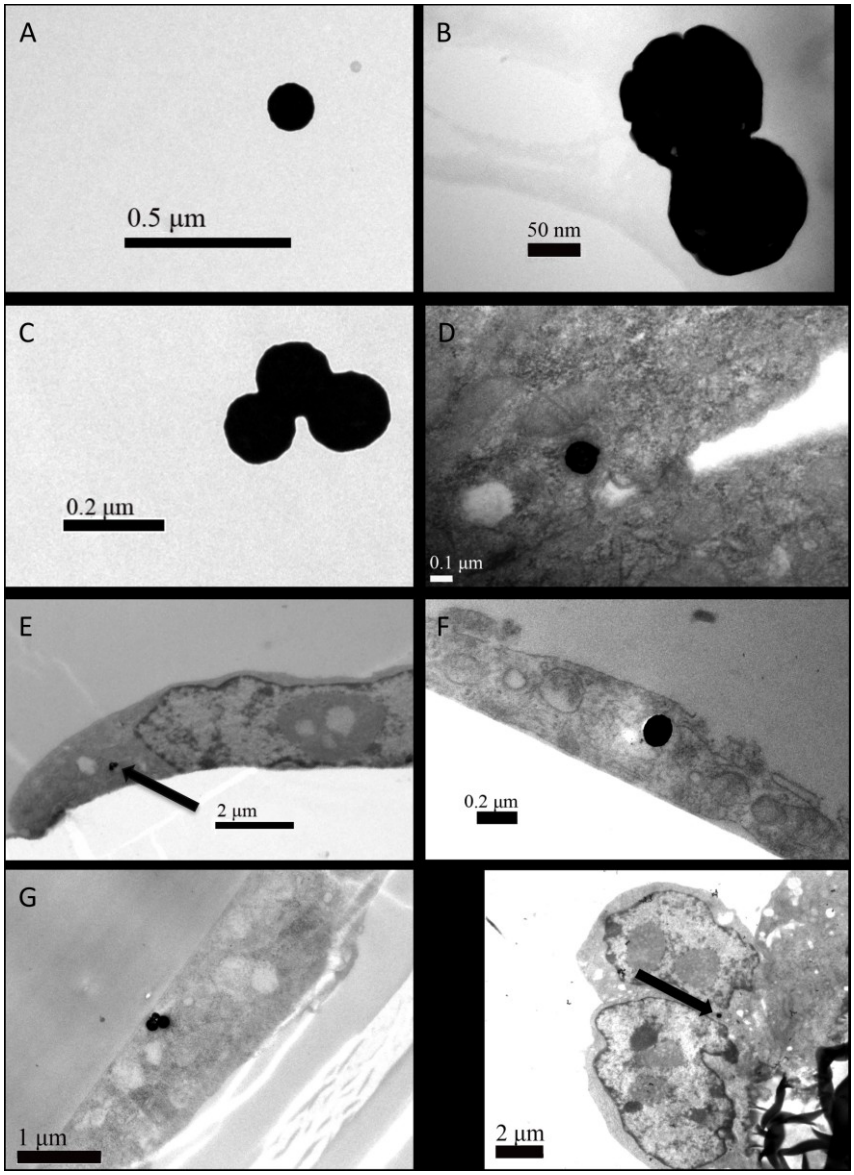

Appendix 3: TEM images of nanosensors. **(A)** Single nanosensor; **(B)** nanosensor dimmer; **(C)** nanosensor trimer; **(D)** single cytoplasmic nanosensor adjacent to a mitochondrion; **(E)** single nanosensor in cytoplasm; **(F)** single nanosensor in cytoplasm; **(G)** nanosensor aggregate in cytoplasm and; **(H)** single nanosensor between two nuclei. Arrows have been used to identify nanosensor locations where resolution is low.

Appendix 4 NLS Peptide Synthesis – Structures and Mechanisms

Fmoc-Gly-OH 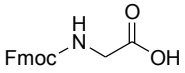

Fmoc-Arg(Pbf)-OH 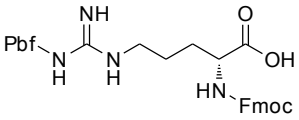

Fmoc-Lys(Boc)-OH 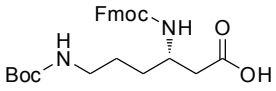

Fmoc-Cys(Trt)-OH 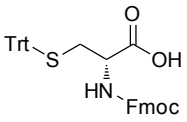

Fmoc-Val-OH 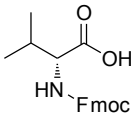

Fmoc-Pro-OH 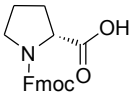

Appendix 4a: Molecular structure of AAs used in the syntheses of CA-NLS 1 and CA-NLS 2.

Fmoc 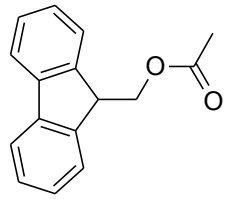

Trt 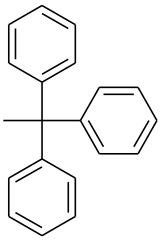

Boc 

Pbf 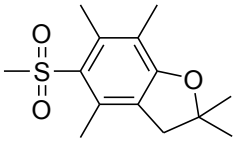

Appendix 4b: Molecular structure of AA protecting groups.

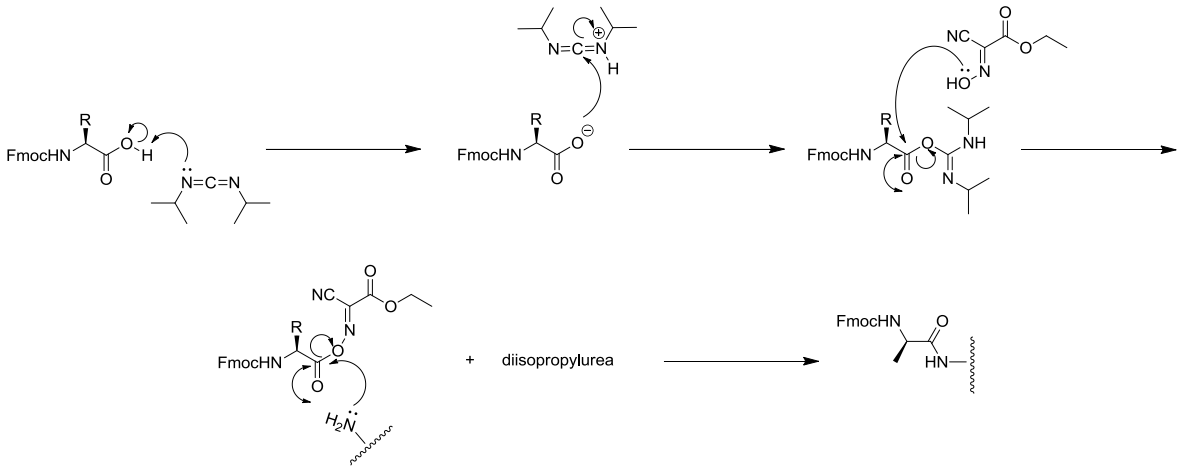

Appendix 4c: Mechanism of DIC peptide coupling.

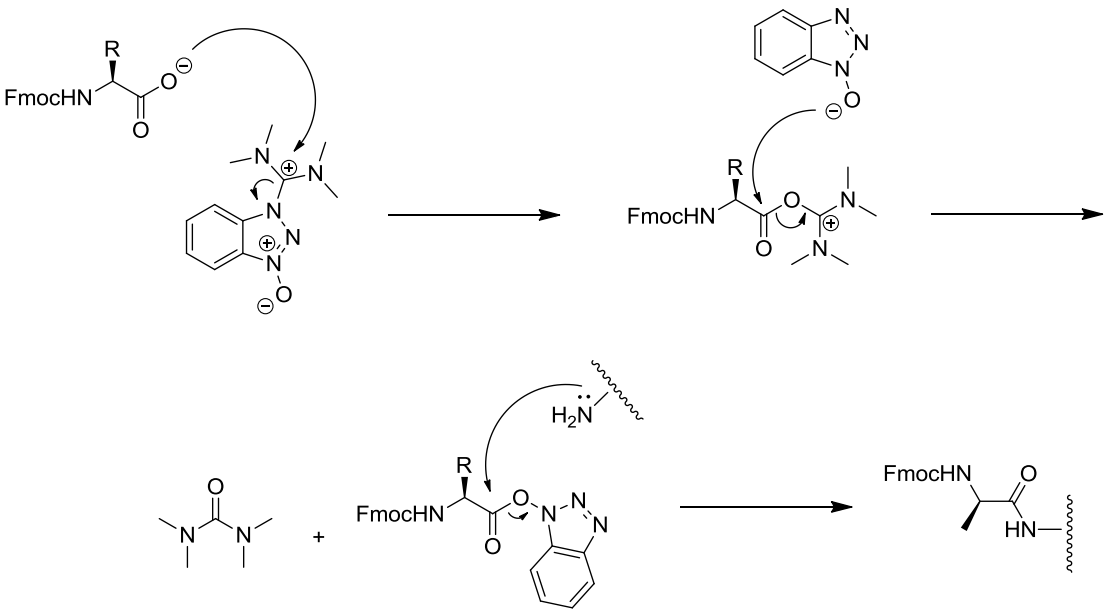

Appendix 4d: Mechanism of HBTU peptide coupling.

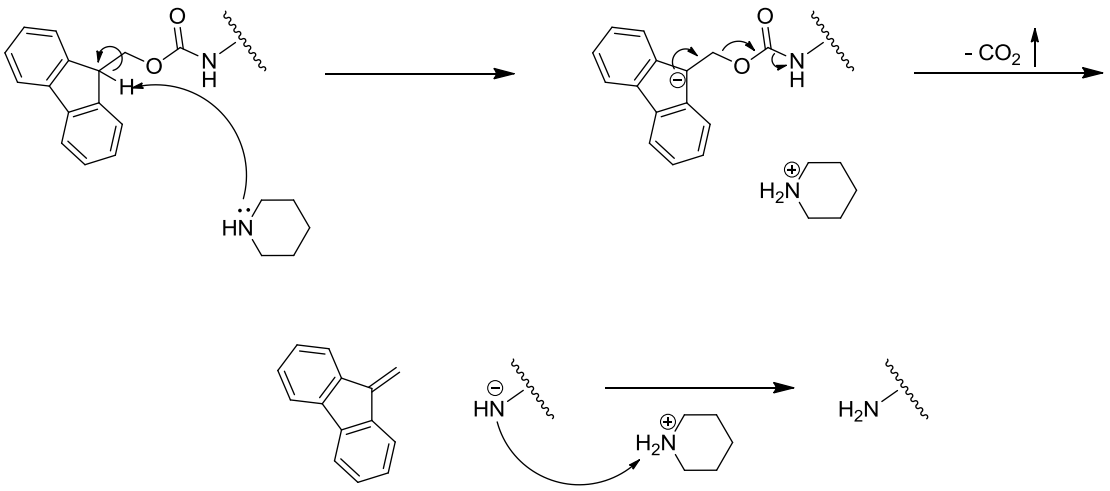

Appendix 4e: Fmoc deprotection mechanism.

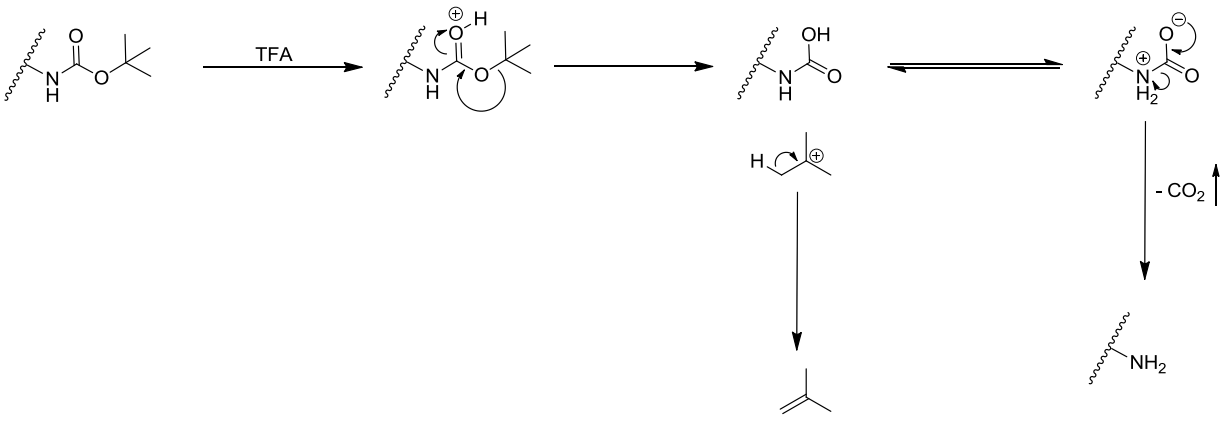

Appendix 4f: tBoc deprotection mechanism.

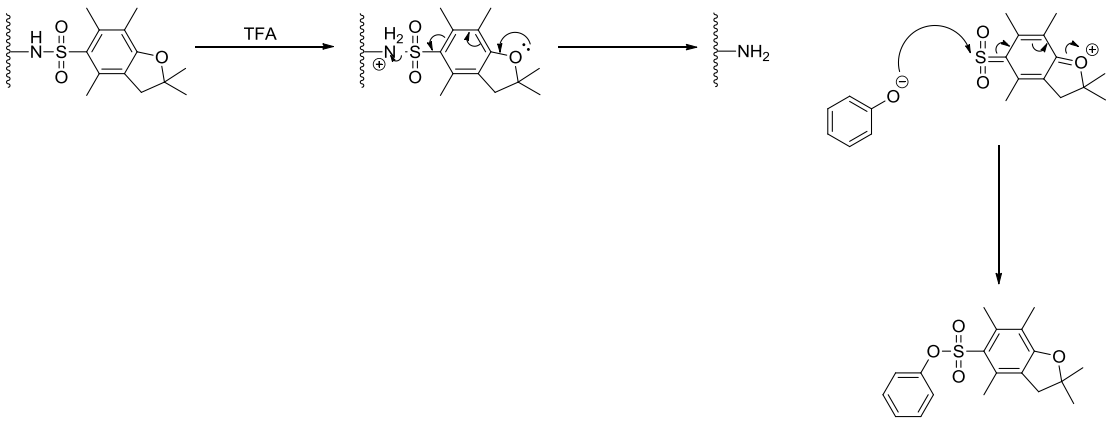

Appendix 4g: Pbf deprotection mechanism.

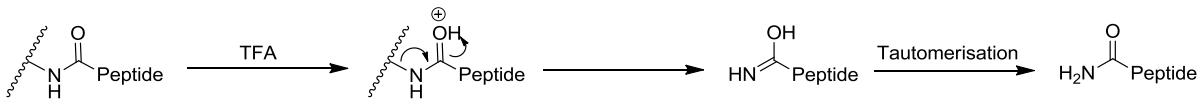

Appendix 4h: TFA cleavage mechanism.

Appendix 5 Fluorescence Images of CA-NLS 1-NR Nuclear Transfection

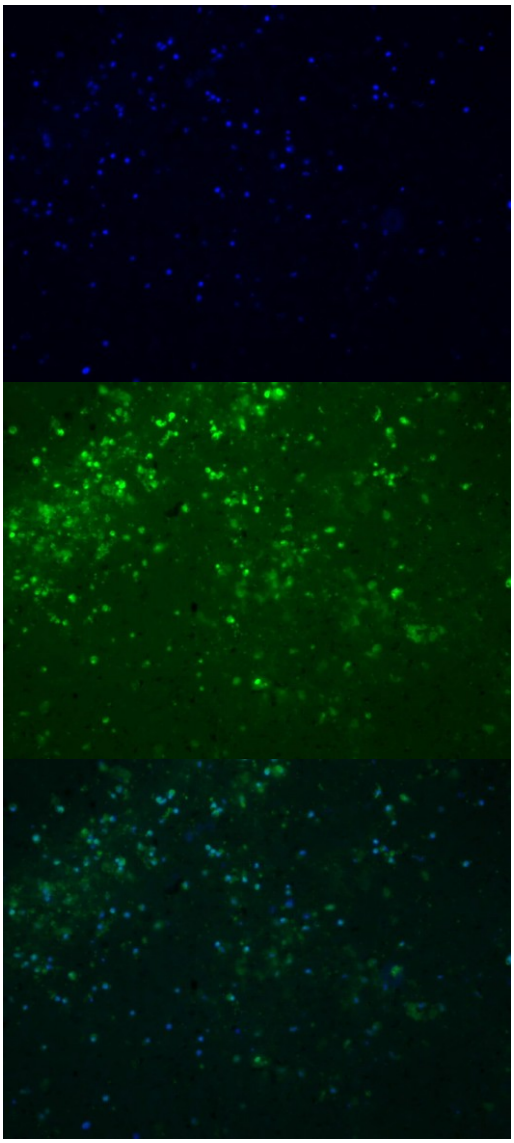

Appendix 5a: Image set 1. Where: Top image = Höescht stained nuclei; middle image = fluorescence from fluorescein moiety of CA-NLS 1 and; bottom image = overlay.

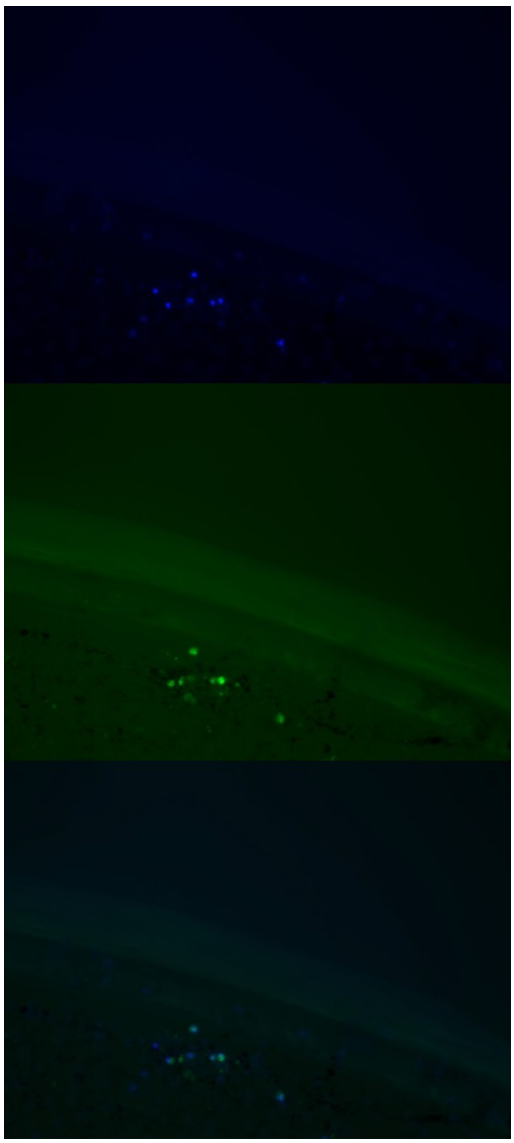

Appendix 5b: Image set 2. Where: Top image = Höescht stained nuclei; middle image = fluorescence from fluorescein moiety of CA-NLS 1 and; bottom image = overlay.

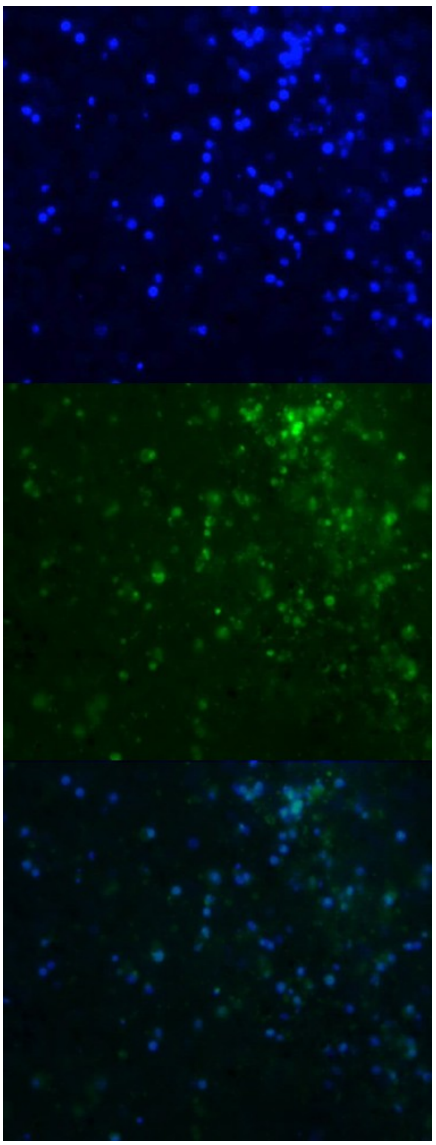

Appendix 5c: Image set 3. Where: Top image = Höescht stained nuclei; middle image = fluorescence from fluorescein moiety of CA-NLS 1 and; bottom image = overlay.

Appendix 6 CA-NLS 2-NR Nuclear Transfection TEM Gallery

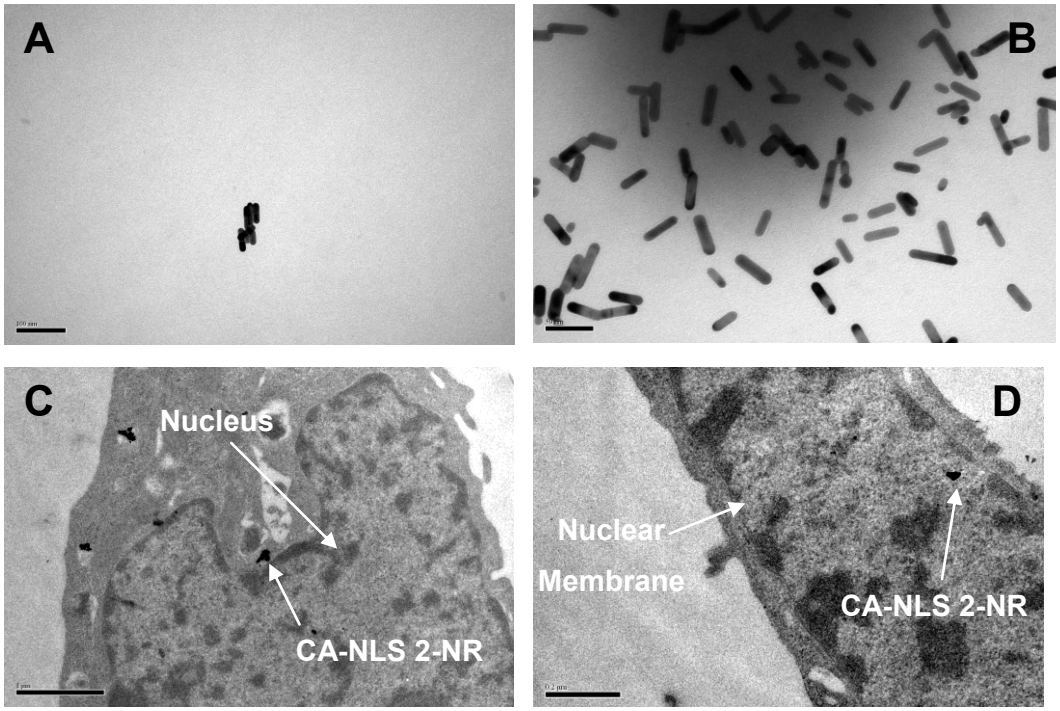

Appendix 6: TEM images of: **(A)** Small cluster of NR; **(B)** large cluster of NR; **(C)** CA-NLS 2-NR just outside the nuclear membrane and; **(D)** CA-NLS 2-NR inside nuclear membrane.

Appendix 7 GSH Recycling Assay Standard Curves

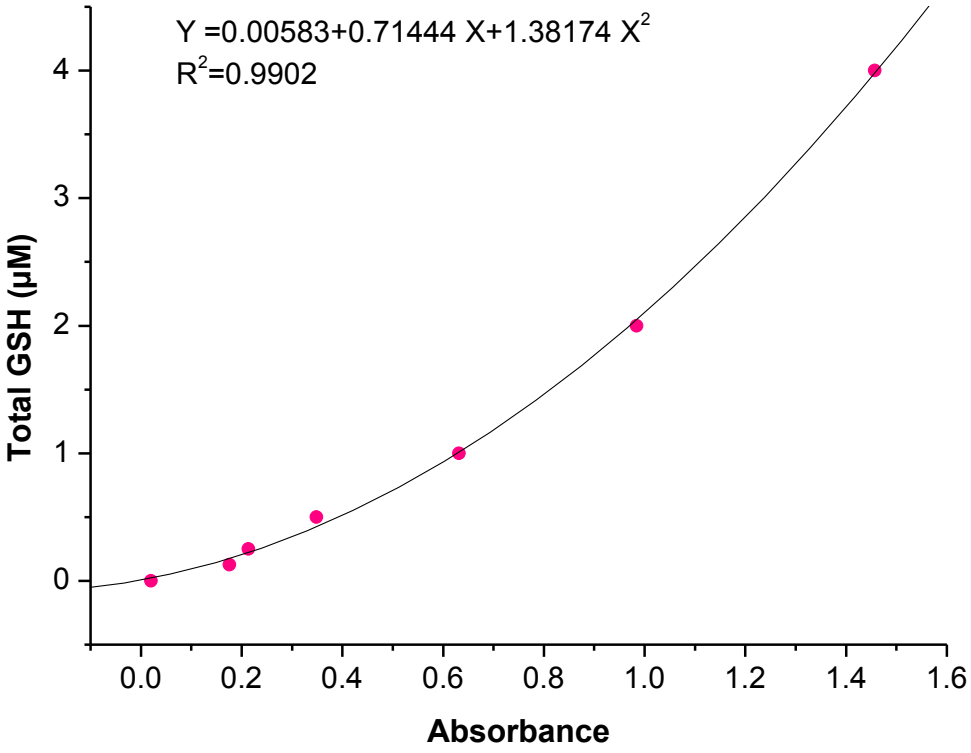

Appendix 7a: GSH standard curve. Concentration range – 0-4 µM GSH.

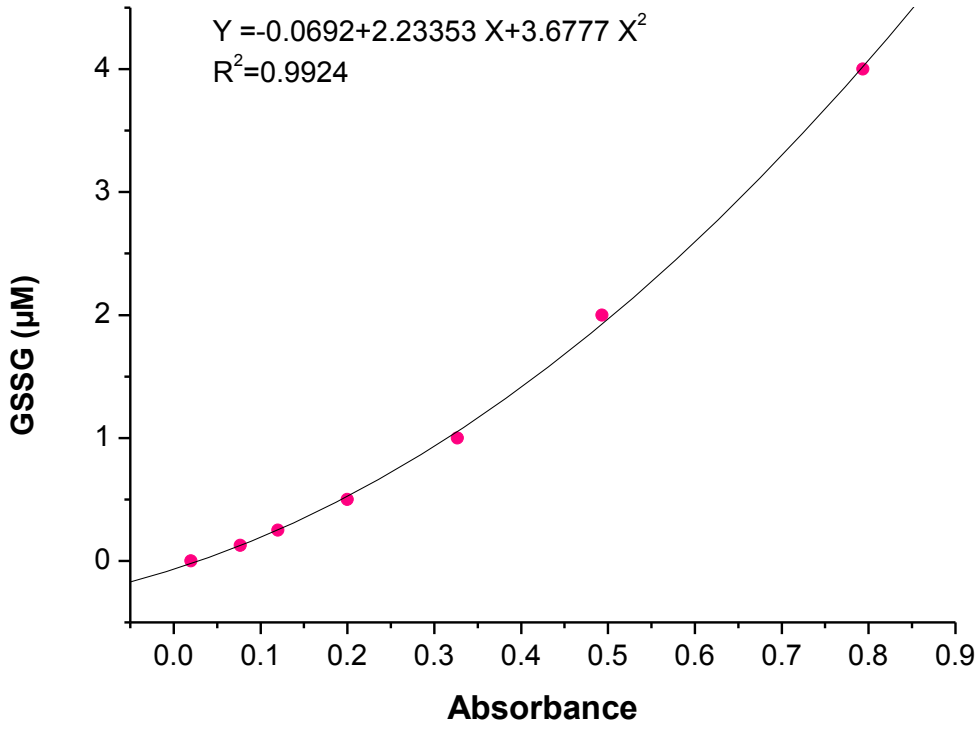

Appendix 7b: GSSG standard curve. Concentration range – 0-4 µM GSSG.

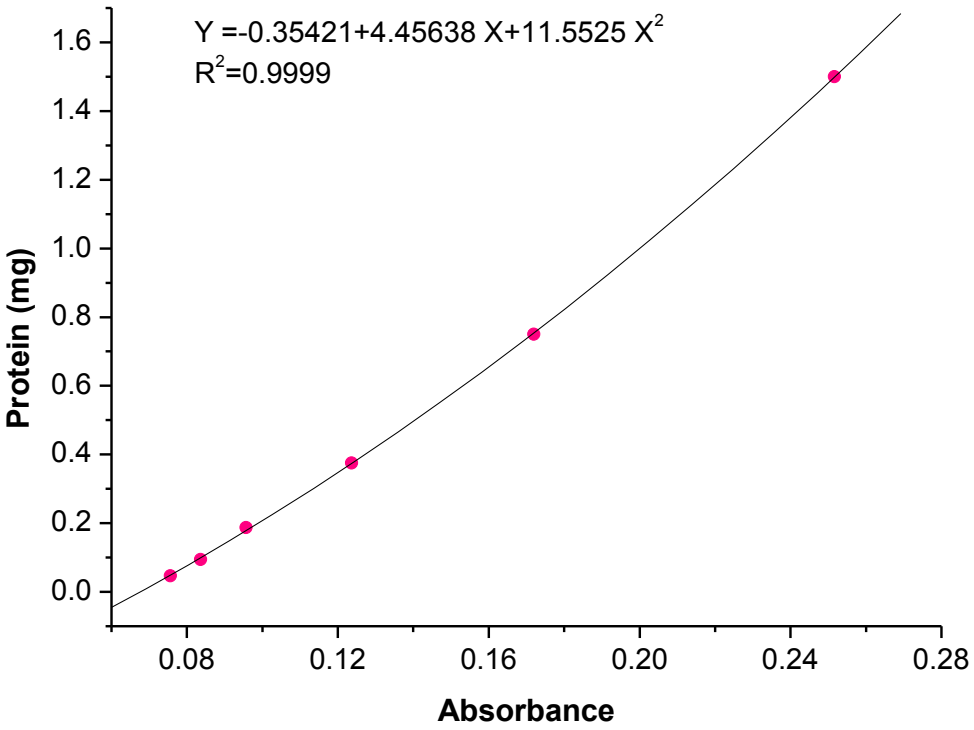

Appendix 7c: BCA protein assay standard curve.

Appendix 8 Representative SERS Spectra from Intracellular Experiments

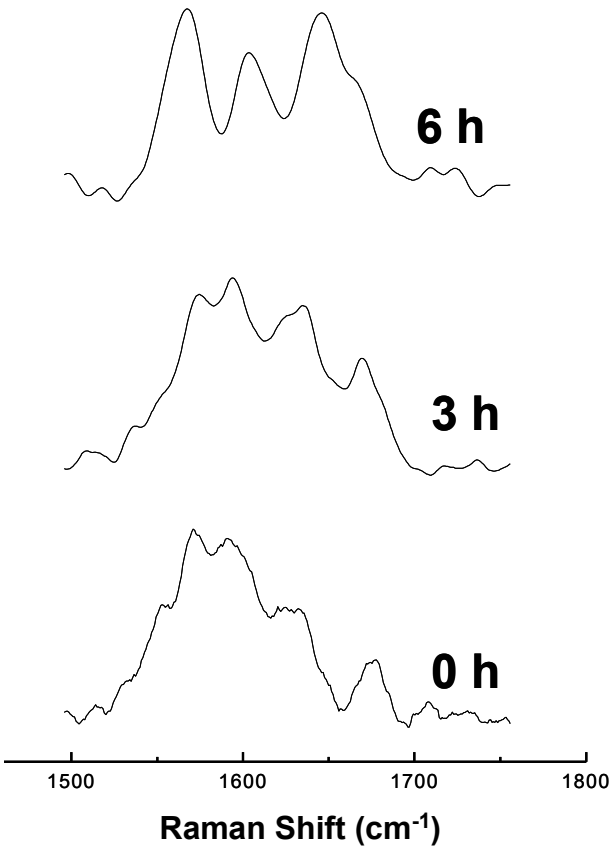

Appendix 8a: SERS spectra of NQ-NS from cells undergoing staurosporine-induced apoptosis at 0, 3 and 6 h time points.

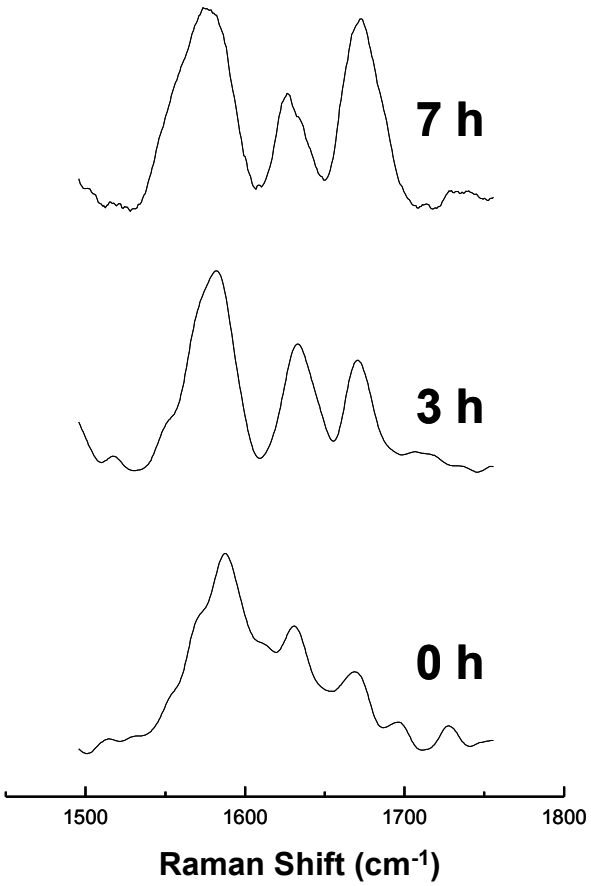

Appendix 8b: SERS spectra of NQ-NS from cells undergoing H_2O_2-induced apoptosis at 0, 3 and 7 h time points.

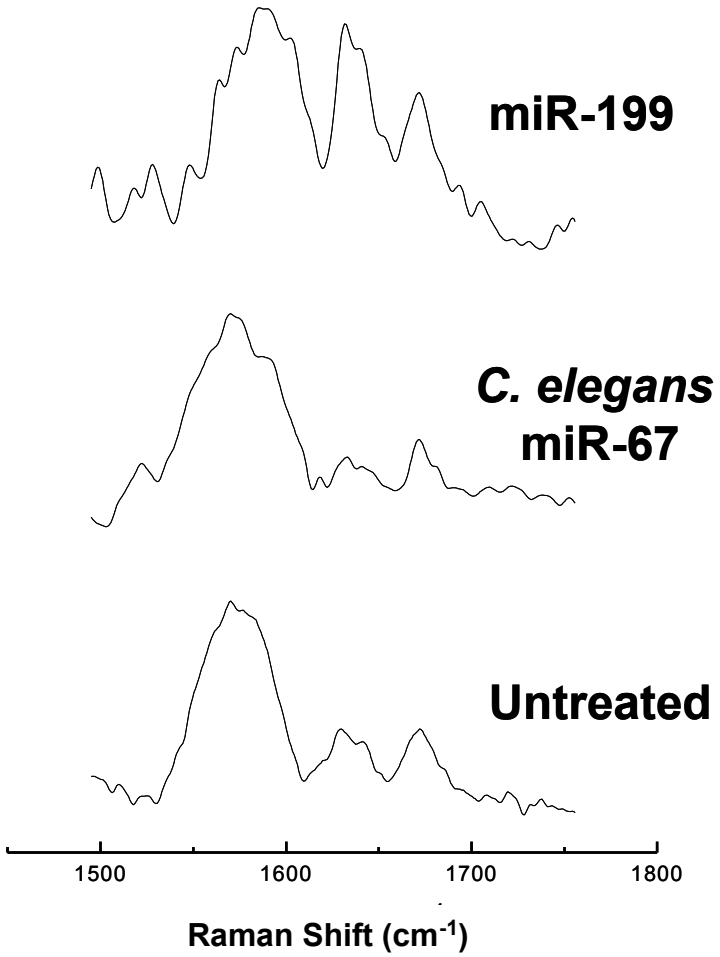

Appendix 8c: SERS spectra of NQ-NS from cells treated with miR-199 and *C. Elegans* miR-67, as well as untreated cells.